THE UNIVERSITY OF CALGARY

AIRBORNE GPS/INS WITH AN APPLICATION TO AEROTRIANGULATION

by

M. ELIZABETH CANNON

A THESIS

SUBMITTED TO THE FACULTY OF GRADUATE STUDIES

IN PARTIAL FULFILLMENT OF THE REQUIREMENTS FOR THE DEGREE

OF DOCTOR OF PHILOSOPHY

DEPARTMENT OF SURVEYING ENGINEERING

CALGARY , ALBERTA

APRIL , 1991

ISBN 0-315-66853-9

THE UNIVERSITY OF CALGARY

FACULTY OF GRADUATE STUDIES

The undersigned certify that they have read, and recommend to the Faculty of Graduate Studies for acceptance, a thesis entitled 'Airborne GPS/INS with an Application to Aerotriangulation' submitted by M. Elizabeth Cannon in partial fulfillment of the requirements for the degree of Doctor of Philosophy.

K.P. Schwarz.

Supervisor, Dr. K.P. Schwarz
Department of Surveying Engineering

M. A. Chapman

Dr. M.A. Chapman
Department of Surveying Engineering

Dr. E.J. Krakiwsky
Department of Surveying Engineering

S E Franklin

Dr. S. E. Franklin
Department of Geography

Delikaraoglou

Dr. D. Delikaraoglou
Energy, Mines & Resources

Date April 15, 1991

ABSTRACT

The integration of a differential Global Positioning System (GPS) receiver system with an Inertial Navigation System (INS) is investigated for kinematic positioning in land and airborne environments with the emphasis on accuracies at the cm-level. Fundamental aspects of both GPS and INS are presented and the error sources of each are analyzed. A centralized Kalman filter approach is developed which incorporates double differenced GPS measurements as updates to the INS. Land kinematic tests are used to demonstrate that the integrated system is capable of providing kinematic positions with an external accuracy of 5 cm (1σ). In airborne mode, accuracies at the 15 cm level are achieved when the GPS/INS positions are compared to photogrammetrically-derived camera coordinates. The application of airborne GPS/INS to large-scale aerotriangulation is assessed for the cases when no ground control or minimal ground control are available. Tie point ground coordinates are estimated to be accurate to 15 cm (1σ) when no ground control is utilized. Alberta large-scale mapping requirements of 12.5 cm horizontally and 10.0 cm vertically are reached when at least one ground point is included in the block adjustment.

ACKNOWLEDGEMENTS

I would like to express my appreciation to my distinguished supervisor, Professor Klaus-Peter Schwarz, for his continued support and encouragement throughout my Ph.D. program.

Thanks also go to the many students in the Department for their assistance in data collection as well as for the many fruitful discussions throughout my graduate studies. Specifically, I would like to acknowledge Dr. R.V.C. Wong, Mr. D. Lapucha and Mr. H. Martell. Dr. E.T. Knickmeyer is thanked for organizing the U of C contribution to the GPS/INS airborne campaign in Germany and for participating in it. Data needed for this thesis were collected in that campaign. Appreciation is also extended to Dr. M.A. Chapman for the many discussions on aerotriangulation and for use of his bundle adjustment program. Dr. J. Krynski is acknowledged for the INS error simulation, and Dr. J. Czompo is thanked for performing the FFT on the INS gyro data.

I would like to acknowledge the co-operation between the Department and the University of the Federal Armed Forces in Munich for the first series of GPS/INS airborne photogrammetric tests which formed the basis of this research. Professor G. Hein, Mr. G. Baustert and Mr. C. Schwiertz, University of the FAF, are thanked for their assistance in the data reduction and assessment of the results.

Financial support for part of my Ph.D. studies from the Killam Memorial Foundation is greatly appreciated.

TABLE OF CONTENTS

LIST OF TABLES

LIST OF FIGURES

NOTATION

i) Conventions

a) Matrices are uppercase and bold

b) Vectors are lowercase and bold

c) Rotation matrices between coordinate systems are defined by a subscript and a superscript denoting the two coordinate systems, e.g. $\mathbf{R}_w^b$ indicates a transformation from the wander frame (w) to the body frame (b). The angular rate vector, ω_{ib}^b, represents the rotation of the body frame with respect to the inertial frame coordinated in the body frame.

d) The following operators are defined as:

(+)	Kalman update
(-)	Kalman prediction
$\dot{a}$	derivative with respect to time
A^T	matrix transpose
C^{-1}	matrix inverse
Δ	single difference between receivers
δ	correction to
f{ }	is a function of
$\hat{x}$	estimated value
$\tilde{x}$	measured value
x_o	initial value
∇	single difference between satellites

ii) Coordinate Systems

Body (b): A right-handed system which defines the frame in which the raw INS measurements are made.

origin: at the centre of the INS

x-axis: towards the right side of the INS

y-axis: towards the output pins of the INS

z-axis: upwards, perpendicular to the x-y plane

Earth (e): A right-handed system which is used as an intermediate computational frame.

origin: at the centre of mass of the earth

x-axis: towards the mean Greenwich meridian in the equatorial plane

y-axis: 90 degrees east of the Greenwich meridian in the equatorial plane

z-axis: mean axis of rotation of the earth

Inertial (i): A right-handed system to which the x-axis INS measurements are referred to. This system is called an 'operational' rather than a true inertial frame due to the approximations made.

origin: at the centre of mass of the earth

x-axis: towards the mean vernal equinox at t_o

	y-axis:	completes a right-handed system
	z-axis:	towards the mean north celestial pole at t_o

Local level (n): A right-handed system which is used as a computational frame for the trajectory computation. It is defined with respect to a best fitting ellipsoid with origin at the earth's centre of mass.

origin:	at the centre of the INS
x-axis:	towards ellipsoidal east
y-axis:	towards ellipsoidal north
z-axis:	upwards, along ellipsoidal normal

Wander (w): A right-handed system in which the INS computations are made. It is similar to the local-level frame except for a rotation in the x-y plane.

origin:	at the centre of the INS
x-axis:	rotated towards the east by an angle, α, the wander angle. This angle is selected to be the meridian convergence at the initial point.
y-axis:	orthogonal to the x-axis in the level plane
z-axis:	upwards, along ellipsoidal normal

iii) Symbols

A	design matrix
α	wander azimuth
b	accelerometer bias vector
c	speed of light (299792458 m s^{-1})
$\mathbf{C}^e$	Kalman measurement noise covariance matrix
$\mathbf{C}^w$	Kalman filter process noise covariance matrix
$\mathbf{C}^x$	Kalman state vector covariance matrix
d	gyro drift vector
dT	receiver clock error
dt	satellite clock error
ε	measurement noise
Φ	carrier phase (m)
F	dynamics matrix
$\mathbf{\Phi}$	Kalman filter transition matrix
f	carrier phase frequency, camera focal length
ϕ	geodetic latitude; carrier phase (cycles); exterior orientation angle; roll
f	specific force vector
F[$\cdot$]	Fourier transform
g	gravitational acceleration vector
γ	normal gravity

h	geodetic height
$\mathbf{I}$	identity matrix
$\mathbf{K}$	Kalman gain matrix
κ	exterior orientation angle
λ	geodetic longitude; carrier phase wavelength
$\mathbf{l}$	vector of measurements
N	carrier phase ambiguity
P	pseudorange
$\mathbf{Q}$	spectral density matrix
θ	incremental velocity vector; pitch
ρ	computed distance between satellite and receiver
R_E	earth radius
R_M	meridian radius of curvature
R_N	prime vertical radius of curvature
$\mathbf{r}_r$	coordinates of receiver
$\mathbf{r}^s$	coordinates of satellite
$\mathbf{v}$	velocity vector
Ω	three parameter skew symmetric matrix
ω	2π (rad); exterior orientation angle; INS angular rate vector
$\mathbf{w}$	process noise vector
$\mathbf{x}$	Kalman state vector; Cartesian x coordinate
ψ	azimuth

iv) Acronyms

A-S	Anti-Spoofing
C/A code	Clear/Aquisition code
DoD	U.S. Department of Defense
FFT	Fast Fourier Transform
GPS	Global Positioning System
INS	Inertial Navigation System
MDB	Minimum Detectable Bias
P code	Precise code
PC	Perspective Centre
PPS	Precise Positioning Service
PRN	Pseudo Random Noise
PSD	Power Spectral Density
RF	Radio-Frequency
RLG	Ring Laser Gyro
RMS	Root Mean Square
SA	Selective Availability
SNR	Signal-to-Noise Ratio
SPS	Standard Positioning Service
TEC	Total Electron Content
WGS-84	World Geodetic System 1984
ZUPT	Zero Velocity Update

CHAPTER 1

INTRODUCTION

1.1 Background and Objective

The integration of a Global Positioning System (GPS) receiver with an Inertial Navigation System (INS) was initially conceived by military groups concerned with accuracies at the level of several metres to address navigation requirements. However, the application of this integrated technology to precise kinematic surveying where centimetre or decimetre accuracies are required is relatively new, and virtually non-existent in the airborne environment.

The motivation for the integration of GPS and INS for high accuracy kinematic positioning is to exploit the benefits of each positioning system. GPS, when operated in a differential mode, provides accurate position and velocity information when the carrier phase observable is utilized. In general, the data have consistent accuracy throughout a survey mission, but are affected by cycle slips caused by loss of phase lock between the receiver and a satellite. These cycle slips can significantly degrade the positioning accuracy in kinematic mode. A GPS receiver is also susceptible to outages where no satellites are tracked due to shading. This is especially prevalent in urban areas or when encountering highway tunnels, for example. In contrast, an INS is a self-contained system which gives accurate relative position information, but is subject to time dependent error growth when operated in an unaided mode. Therefore, when the two systems are combined, the short term position accuracy of INS can be used to detect and correct cycle slips in the GPS carrier phase data, while the accurate GPS measurements can provide updates to the INS on a consistent and frequent basis. An INS can also bridge the gaps in satellite tracking due to masking. The resulting integrated system is not only accurate but more reliable and operationally more flexible than the individual systems.

Integration of GPS and INS can be accomplished at two different levels, namely, by direct hardware integration, or merely by combining the output data of each in a software processing scheme. The advantage of hardware integration is that the two systems can directly aid each other so information from one system can be used as feedback to the other. For example, INS acceleration measurements can be used to control the GPS receiver tracking bandwidth so cycle slip occurrence is minimized (Hemesath,1980). Also, satellite re-acquisition after loss of satellite tracking will be faster if the estimated INS position is used to re-initialize the GPS receiver. The disadvantage of this approach is that no off-the-shelf systems currently exist that address the high accuracy market. Therefore, the current research uses the technique of data integration, where the two hardware components do not communicate, but instead the data streams are combined in software.

A variety of tests of precise differential kinematic positioning using the GPS-only approach have taken place over the last several years. Mader (1986) showed that cm accuracies (height component only) are achievable in an aircraft when cycle slips are not present in the carrier phase data while Cannon (1987) showed degradation to the dm-level when numerous cycle slips are detected in land mode. More recently, the emphasis has been on reducing the effect of cycle slips by instantaneous cycle slip fixing or 'on the way' ambiguity resolution to maintain cm accuracies, e.g. Seeber and Wübbena (1989), Cannon (1990). Keel et al. (1989) report airborne accuracies at the sub-metre level using the carrier smoothed pseudorange processing technique, while Baustert et al. (1989) improve this accuracy to the cm-level using double differenced carrier phase in a Kalman filter model. Overall, however, cycle slips still pose a significant problem for reliable high accuracy kinematic positioning as do the presence of position drifts detected in some airborne results, e.g. Friess (1988).

Inertial positioning techniques are well-developed and dm-accuracies are routinely achieved, e.g. Wong (1985). The application of strapdown INS technology to the surveying market is relatively new, but it has been demonstrated that this lower cost hardware can meet survey requirements if proper modelling is applied (Wong,1988). Most of these tests use the method of coordinate or zero-velocity updates where the vehicle must stop briefly during the mission in order to bound time dependent INS errors. Therefore, the main limitation of inertial positioning for continuous precise kinematic positioning, especially in an aircraft, is the need for frequent updates from an independent positioning system. Currently, GPS is the only positioning system that can satisfy the accuracy requirements in a cost-effective and flexible manner.

GPS/INS tests for high accuracy positioning have been limited to date. Wong et al. (1988) report dm-level accuracies when a local-level INS is combined with TI4100 receivers in differential land mode. Lapucha (1990) increased these accuracies to the cm-level with improved hardware, further model development, and more effective cycle slip detection and correction procedures. In this case, five channel Trimble 4000SX receivers were integrated to the U of C's LTN 90-100 strapdown INS in a land vehicle. No results for high accuracy GPS/INS in an airborne environment have been previously reported. However, a joint GPS/INS-photogrammetric campaign conducted by the University of the Federal Armed Forces, Munich, The University of Calgary and the Rheinbraun Company, Cologne, provided the test data necessary for a comprehensive study of precise aircraft positioning which forms the basis of this thesis.

The application of GPS technology to aerotriangulation has been recognized for some time, e.g. Schwarz et al. (1984), Goldfarb (1987), Lucas and Mader (1989) and is motivated by the potential for increased cost-effectiveness when this technology is incorporated into photogrammetric campaigns. If ground control can be replaced by accurate positions at flight level, the need for pre-targetting ground points may be eliminated. The establishment of ground control can consume up to 50% of the budget in a photogrammetric project (Moffitt and Mikhail,1980). Many preliminary tests have been conducted to assess the feasibility of applying GPS to aerotriangulation without ground control, e.g. Andersen (1989), Colomina (1988,1989), Dorrer and Schwiertz (1990), van der Vegt (1989), van der Vegt et al. (1988). Although results from these tests are encouraging, irregularities such as GPS position drifts were detected in many instances. The problem of transformation between a local datum and the GPS reference datum (WGS-84) was also encountered. Stand-alone INS has also been used for aerotriangulation without ground control, e.g. Thyer (1988), Thyer et al. (1989), however, it is not applicable to large-scale photogrammetry where the accuracy requirements are relatively stringent. Besides the accuracy and reliability of the estimated positions, the advantage of GPS/INS in aerotriangulation is the attitude information provided by INS which may be included in the block adjustment if the photogrammetric orientation requirements can be met. Currently, the only application of GPS/INS to aerotriangulation has been through simulation studies, e.g. Goldfarb (1987).

The main objective of this research is to investigate the potential of GPS-INS integration for high accuracy kinematic positioning in post-mission. Two kinematic test cases are used in the analysis, namely data collected in land and airborne modes. Land data are used to demonstrate the feasibility of this technology for precise kinematic positioning before the new application of GPS/INS to the airborne environment is approached. The subsequent use of GPS/INS-derived positions in aerotriangulation is also studied to determine the requirements for large-scale mapping without ground control. High accuracy GPS/INS for airborne positioning and aerotriangulation using real test data has not been previously investigated.

1.2 Outline

In Chapter 2, the main measurement systems are discussed. Fundamental aspects of GPS are summarized and receiver designs currently available are reviewed with the desired hardware specifications for precise kinematic applications being listed. The prime GPS observables and their error sources are given and the differencing technique to reduce these errors is also reviewed. Fundamental aspects of INS as well as the various platforms are also discussed in Chapter 2. Strapdown INS mechanization equations, alignment procedure and error sources are outlined. General aerotriangulation concepts are also reviewed in this chapter and the concept of block adjustment is introduced. Finally, the combination of these three measurement systems is discussed and the integration strategy is developed.

In Chapter 3, the mathematical methodology for the post-mission reduction of the GPS and INS data is derived. A centralized Kalman filter approach which uses double differenced GPS observables as measurement updates to the INS forms the basis of the methodology. The cycle slip detection and correction algorithm based on predicted GPS antenna positions using INS data is detailed. Main features of the software package, **GPSINS**, which incorporates the mathematical methodology discussed in Chapter 3, are outlined. Photogrammetric block adjustment using the bundle method is outlined with the emphasis being on aerotriangulation without ground ground control.

Chapter 4 concentrates on kinematic results using the land test data collected on a well-controlled traverse. The adequacy of the mathematical model for cm-level positioning is verified. This includes analysis of the cycle slip detection and correction procedure using simulated carrier phase cycle slips. The effect of various GPS update rates and outages on precise kinematic positioning is also investigated in this chapter, and finally, the effect of incorrect initial ambiguity resolution on precise kinematic positioning is demonstrated using land test data.

In Chapter 5, aircraft data are analyzed to determine the potential of GPS/INS for precise kinematic positioning in this dynamic environment. Estimated GPS/INS positions are compared to photogrammetrically-derived positions to compute the overall achievable accuracy. Attitude parameters estimated from the INS data are also compared to block adjustment values to assess the feasibility of the LTN 90-100 to provide accurate orientation data.

The application of GPS/INS to large-scale aerotriangulation is the focus of Chapter 6. Positions computed from the integrated system are used as perspective centre control in the block adjustment to assess the feasibility of replacing ground control by accurate positions at flight level, hence reducing or eliminating the need for ground control.

The main conclusions formed throughout this thesis as well as recommendations for further GPS/INS - Aerotriangulation development are given in Chapter 7.

CHAPTER 2

MEASUREMENT SYSTEMS

Outlined in this chapter are the measurement system concepts and the fundamental observables. Sources and magnitudes of errors affecting GPS performance are described in detail. The method of observation differencing to reduce single point errors is given and the resulting residual error budget is quantified. Fundamental concepts of inertial positioning are presented and various hardware configurations currently available are described. The raw data mechanization equations for the strapdown INS case are given and finally, the alignment procedure is discussed. Photogrammetric coordinate frames used in aerotriangulation are defined and the collinearity equations are presented. Finally, a summary of the three measurement systems and a discussion of integration strategies concludes the chapter.

2.1 Global Positioning System

The Global Positioning System is a satellite-based radionavigation system being developed by the U.S. Department of Defense (DoD). Once complete, there will be 21 satellites available plus three active spares occupying six orbital planes (four satellites per plane) inclined at a 55 degree angle with respect to the equator. It will be an all-weather system providing 24 hour, world-wide satellite coverage with a minimum of four satellites in view at any one time. Currently, there are 16 satellites operational, of which six are prototype Block I. The system is expected to be fully operational by the beginning of 1993.

GPS satellites orbit 20,200 km above the Earth's surface with a period of 12 hours. They transmit signals on two frequencies; L1 at 1575.42 MHz and L2 at 1227.6 MHz. These signals are bi-phase modulated by one or two pseudo random noise (PRN) codes; the Clear Acquisition, C/A code, and the Precise, P code. The L1 carrier is modulated by both the C/A and P codes while the L2 carrier is only modulated by the P code. The C/A code is transmitted at 1/10 the fundamental GPS frequency (10.23 MHz) and is repeated every one ms. In contrast, the P code is transmitted at the fundamental frequency and is only repeated every 267 days. The navigation message, containing broadcast ephemeris and health information, is modulated on both frequencies at a 50 bits per second rate.

The C/A code is unrestricted and used for the Standard Positioning Service (SPS) where single point accuracies of 20-30 m horizontally and 30-45 m vertically can be achieved at the 95% confidence interval. When Selective

Availability (SA) is turned on, these accuracies are reduced to 100 and 156 m in the horizontal and vertical components, respectively. SA is implemented by a combination of degraded satellite orbital information (ε-type) and satellite clock dithering (δ-type). It was turned on in April, 1990, but has been turned off since August, 1990. However, the DoD retains the right to implement SA on a satellite once it is declared operational.

The more accurate P code, which provides the Precise Positioning Service (PPS) to military users, gives accuracies of 15-25 m horizontally and 20-30 m vertically (95%) when SA is off. Although the two frequency data are available when SA is on, these real-time accuracies are degraded to SPS accuracies for civilian P code receivers. Once the system is fully operational, civilian users will be restricted from the P code by the DoD. This restriction is accomplished by means of Anti-Spoofing (A-S), where the P code is translated (to give the Y-code) except for the U.S. military.

2.1.1 Receiver Technology

GPS hardware has undergone many changes in the past several years in terms of size, weight, cost and capabilities. Listed in Table 2.1 are the classes of GPS receivers that are currently available to civilians (Lachapelle et al.,1991). Several options exist from a C/A code receiver which gives pseudorange and carrier phase on the L1 frequency, to a full P code receiver which gives pseudorange and carrier phase on both L1 and L2 frequencies. The advantage of the P code receivers is that the raw data have smaller noise characteristics than C/A code data and ionospheric corrections can also be computed. Techniques such as widelaning and extrawidelaning (Wübbena,1989) can also be used to recover carrier phase ambiguities when P code data are collected. This is advantageous for kinematic applications where efficient initial ambiguity recovery techniques must be used. However, with the implementation of A-S, a P code receiver will convert to C/A code mode, and the advantages of using a P code receiver will not be realized.

One receiver technology that falls between these two limits is the C/A code - P codeless receiver which does not require the P code, but can provide the absolute ionospheric group delay by comparing the received L1 and L2 P codes. This concept is implemented in the Rogue receiver (Meehan et al.,1987). With this type of receiver, the L2 carrier is cross-correlated with the L1 signal to give the full wavelength L2 carrier measurement, as opposed to the half wavelength L2 measurement when the squaring technique is used.

Table 2.1
GPS Receiver Classes and Characteristics

Class	Characteristics
C/A code	pseudorange and carrier phase on L1
C/A code L1 + L2 squaring	pseudorange and carrier phase on L1, carrier phase on L2 (λ = 12 cm)
C/A code L1, P code L2*	pseudorange and carrier phase on L1, carrier phase on L2 (λ = 24 cm)
P code**	pseudorange and carrier phase on L1 and L2
C/A code - P codeless	pseudorange and carrier phase on L1, carrier phase on L2 (λ = 24 cm), absolute ionospheric group delay

* requires P code on L2 only
** requires full P code

The availability of multi-channel receivers is a benefit for high accuracy kinematic applications. Typical geodetic-quality receivers consist of 8-12 channels (e.g. Trimble 4000SST and Ashtech LD-XII), meaning that data from up to 8-12 satellites can be collected simultaneously, giving 'all-in-view' tracking capability. This is important not only from an accuracy point of view, but also in terms of maximizing reliability. Clearly, with high measurement redundancy in the estimation process, carrier phase cycle slip detection and correction becomes more effective.

Raw data rate is another important aspect in the selection of a receiver for precise kinematic positioning. Nominal data rates are generally 1 Hz, with some receiver types reaching 2-4 Hz. Although this is not such an critical issue in the GPS/INS case where the INS can provide high interpolation accuracy, for GPS-only positioning, a high data rate will reduce interpolation errors when relating GPS-derived positions to an external event, e.g. camera exposure time. It also assists in cycle slip detection and correction. The degree of interpolation-induced accuracy is not only a function of data rate, but also of the vehicle dynamics. Some receivers circumvent this problem by having the capability of direct time synchronization so measurements are collected from the GPS receiver and external sensor at the same instant.

Size, weight and power consumption are also important factors in receiver selection. Receivers on the market today are generally lightweight (4 - 5 kg), small (6,000 to 7,000 cm^3), and require little power (< 10 W). In the future, technologies such as Monolithic Microwave Integrated Circuits (MMIC) and Very High Speed Integrated Circuits (VHSIC) will further miniaturize receivers (Krakiwsky et al.,1990). For example, the DARPA GPS chipset, a result of these technologies, weighs 100 g, consumes less than 1 Watt of power and is only 100 cm^3 in volume (Hemesath and Bruckner,1988).

Outlined in Table 2.2 are the major characteristics that are desirable for high-accuracy kinematic positioning. Note the receiver dynamic characteristics that are needed to suit the many kinematic positioning environments, e.g. sea, air and land.

Table 2.2
Desired GPS Receiver Specifications for High-Accuracy Kinematic Applications

Characteristic	Specification
Class	P code
Raw data rate	5 Hz
No. of channels	≥8
Weight	< 10 kg
Power	15 W
Dynamics	200 m s^{-1} (velocity) 2 g (acceleration)

2.1.2 Fundamental Observables and Error Sources

The three fundamental GPS observations, namely pseudoranges (code), carrier phase and Doppler frequencies are generally available on most geodetic quality GPS receivers.

Pseudorange measurements are made by comparing a receiver-replicated PRN code with the incoming signal from a particular satellite to determine the time shift needed to correlate the two signals. This time shift is the pseudorange and it represents the difference in time between signal transmission and reception. Although it is measured in seconds of time, it can easily be converted to units of length using the known speed of light. It is called pseudorange rather than range since the receiver and satellite clocks are not synchronized, hence the pseudorange contains a clock bias.

The *carrier phase* observation is made by differencing the incoming carrier signal with a receiver-generated carrier signal. The resulting *beat* phase is therefore the difference in phase between the satellite and receiver at the time of measurement. Differencing of the carrier signals is much more accurate than the measurement of time in the case of the pseudorange, therefore the carrier phase has lower noise characteristics.

Both pseudoranges and carrier phase contain geometric range information so the position of the receiver can be determined. If the receiver clock was accurately synchronized to the GPS frame, only three observations would be needed to instantaneously compute the three components of the user's position. However, due to the receiver clock error, an additional measurement is required to solve the system of equations. The pseudorange and carrier phase observation equations can be expressed as (Wells et al.,1986)

$$P = \rho + c(dt-dT) + d_{ion} + d_{trop} + d_{\rho} + \varepsilon_{P} , \qquad 2.1a$$

$$\Phi = \rho + c(dt-dT) + \lambda N - d_{ion} + d_{trop} + d_{\rho} + \varepsilon_{\phi} , \qquad 2.1b$$

where	P	... is the pseudorange observation (m)
	Φ	... is the carrier phase observation (m) (i.e. $\lambda\phi_{measured}$ (cycles))
	ρ	... is the satellite - receiver range (m)
	c	... is the speed of light (m s^{-1})
	dt	... is the satellite clock error (s)
	dT	... is the receiver clock error (s)
	λ	... is the carrier phase wavelength (m $cycle^{-1}$)
	N	... is the carrier phase integer ambiguity (cycles)
	d_{ion}	... is the ionospheric correction (m)
	d_{trop}	... is the tropospheric correction (m)
	d_{ρ}	... is the orbital error (m)
and	ε	... is the measurement noise (m).

The ρ term contains the receiver's coordinates, i.e. $||\mathbf{r}^s - \mathbf{r}_r||$, where $\mathbf{r}_r$ is the receiver position vector. The satellite coordinate vector, $\mathbf{r}^s$, can be calculated using the broadcast satellite ephemerides. Each of the other terms in Eqn. (2.1) are either receiver dependent, satellite dependent or are a result of the signal path from the satellite to the receiver; listed in Table 2.3 is the source of each of these errors. The causes and magnitude of each of these errors is discussed in the sequel.

Table 2.3
Source of GPS Errors

Source	Error
Receiver	ε , dT
Propagation	d_{ion} , d_{trop}
Satellite	d_{ρ} , dt

One term that is not listed in Table 2.3 is the carrier phase ambiguity, N. This ambiguity is an integer value which represents the difference between the true range and measured carrier phase. Its magnitude is arbitrary, hence it can vary from several to millions of cycles. Also note that there is an ambiguity for each satellite-receiver pair, i.e. there is no correlation between the ambiguity on one satellite with respect to another. The ambiguity is constant over the observation span, provided that no cycle slips occur in the carrier phase data. Cycle slips are caused by phenomenon such as satellite shading, vehicle acceleration, intense ionospheric activity, etc. and result in loss of phase lock between the receiver and satellite. When cycle slips occur, the carrier phase ambiguity changes by an integer number of cycles, hence a discontinuity in the phase time series appears. In this case, a new ambiguity must be estimated or alternatively the number of cycles slipped must be detected and all subsequent phase data corrected. Although the ambiguity is not considered a GPS error, incorrect estimation of this term will affect the accuracy of the kinematic positioning results. A further discussion of the impact of incorrect ambiguity estimation on precise kinematic positioning is found in Chapter 5.

A third fundamental GPS observation is the *Doppler frequency*, a measure of the induced Doppler effect due to the relative satellite and vehicle motion. It can be considered as an instantaneous measure of the carrier phase rate. The Doppler frequency has units of cycles s^{-1}, which can be converted to m s^{-1} using the carrier phase wavelength, λ. By differentiating the carrier phase observation equation given in Eqn. (2.1b), the Doppler frequency observation equation is given as

$$\dot{\Phi} = \dot{\rho} + c(\dot{d}t - \dot{d}T) - \dot{d}_{ion} + \dot{d}_{trop} + \dot{d}_{\rho} + \varepsilon_{\dot{\Phi}} \qquad 2.2$$

where $\dot{\Phi}$ ... is the Doppler frequency observation (m s^{-1})

and $(\dot{\cdot})$ ... denotes a time derivative.

The term, $\dot{\rho}$, contains velocity components of the receiver and the satellite, i.e. $||\dot{r}^s - \dot{r}_r||$. Since the velocity of the satellite can be computed from the broadcast satellite ephemerides, the instantaneous velocity of the receiver can be estimated when Doppler frequency measurements are observed to at least four satellites simultaneously, i.e. three for 3-D velocity and an additional observation to determine the receiver clock drift, $\dot{d}T$. Note that the time derivative of the carrier phase ambiguity is zero, hence it is neglected in Eqn. (2.2). The advantage of the Doppler frequency not being a function of the carrier phase ambiguity is that it is not affected by cycle slips, so the estimation of the receiver velocity will not be significantly degraded when they occur.

Each of the errors listed in Table 2.3 must be accounted for in order to have optimal, unbiased results. The following discussion details how each of the errors are generally treated as well as the expected magnitude of each.

Receiver Noise, ε:

The measurement noise given in Eqns. (2.1a) and (2.1b) can be expanded to give (Lachapelle et al.,1991)

$$\varepsilon_P = f\{\varepsilon_{P_{RX}}, \varepsilon_{P_{multi}}\}, \qquad 2.3a$$

$$\varepsilon_\Phi = f\{\varepsilon_{\Phi_{RX}}, \varepsilon_{\Phi_{multi}}\}, \qquad 2.3b$$

where $\varepsilon_{P_{RX}}$ ... is the receiver-generated pseudorange noise due to receiver components, tracking bandwidth, etc.

$\varepsilon_{P_{multi}}$ ... is the pseudorange noise due to multipath

$\varepsilon_{\Phi_{RX}}$ ... is the receiver-generated carrier phase noise

and $\varepsilon_{\Phi_{multi}}$ ... is the carrier phase noise due to multipath.

As shown in Eqns. (2.1a) - (2.2b), pseudorange and carrier phase observations provide geometric range information between the receiver and the satellite, but with different noise characteristics. Receiver measurement noise is a result of thermal noise intercepted by the antenna or produced by the internal receiver components. Its magnitude is a function of the tracking bandwidth, carrier to noise density ratios and code tracking mechanization parameters (Martin,1980). For C/A code pseudoranges, the noise is approximately 1-3 m, depending on the dynamics of the receiver and the signal-to-noise ratio

(SNR), and for P code receivers the noise is reduced to approximately 10-30 cm, due to the higher chipping rate. In contrast, the receiver-generated carrier phase noise is about 3-5 mm for both C/A and P codes.

Multipath is a result of the satellite signal reflection from various surfaces surrounding the antenna so the received signal is actually a superimposition of these reflected signals. Shown in Figure 2.1 is the concept of signal multipath. While multipath affects both the pseudorange and carrier phase observables, the magnitude of the error is larger in the case of the pseudorange. Carrier phase multipath does not exceed 25% of the carrier wavelength, e.g. about 5 cm on L1 (Georgiadou and Kleusberg,1989), but can result in a significant accuracy degradation during periods of poor Geometric Dilution of Precision (GDOP).

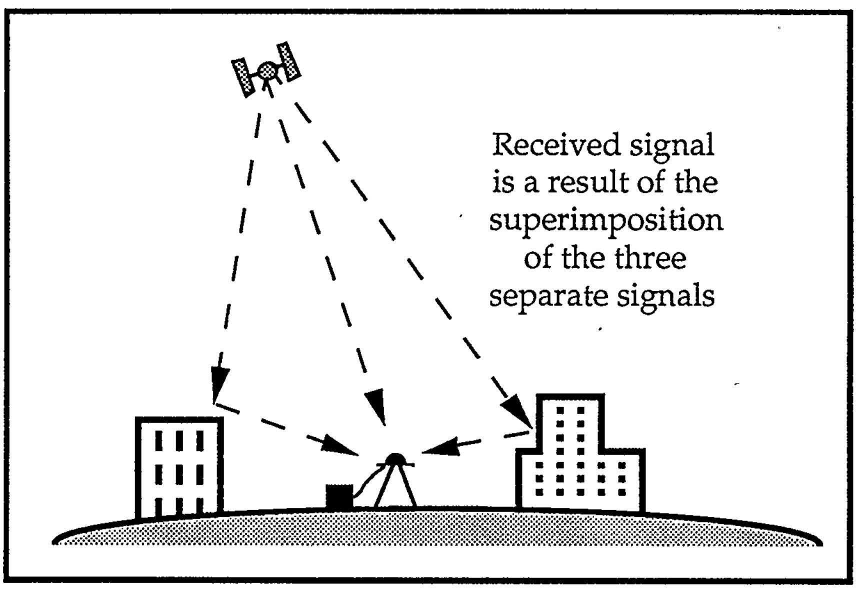

Figure 2.1
GPS Signal Multipath

The magnitude of pseudorange multipath is limited to one chip length of the PRN code, that is 293 m for C/A code and 29.3 m for P code. It is generally systematic in nature for static applications but can be difficult to detect or reduce using standard modelling procedures. In one investigation, static multipath errors with an amplitude of 20 m and a period of several minutes were observed with a C/A code receiver, see Lachapelle et al. (1989). For kinematic applications, multipath is generally random due to vehicle movement, hence the changing satellite geometry with respect to the antenna. Multipath errors can be reduced using radio-frequency (RF) absorbent ground planes or proper location of the antenna.

Receiver Clock Error and Drift, dT and $\dot{d}T$:

The receiver clock error, dT, is the difference between the receiver and GPS time frames due to lack of synchronization between the two clocks. Depending on the receiver hardware, it's magnitude will vary from several ms to less than one ms.

The receiver clock drift, $\dot{d}T$, represents the drift between the receiver and GPS time frames. Its magnitude is a function of the type of clock used in the receiver. Since most geodetic-quality receivers are equipped with high quality ovenized quartz clocks, the drift in the receiver clock is relatively stable.

Since the clock errors are receiver dependent, they are common to all observed satellites and can thus be estimated along with the receiver position (or velocity). However, through linear combinations of the observations to various satellites, these errors can be eliminated. This is discussed in detail in Section 2.1.3.

Ionospheric Error, d_{ion}:

The ionosphere is that region of the atmosphere located 50 - 1000 km above the earth's surface. Non-linear dispersion effects due to the ionization of gases in this region affect the satellite signals which must pass through it (Wells et al.,1986). The effect of the ionosphere is to delay the pseudorange and advance the carrier phase observation, hence the opposite sign for the d_{ion} term in Eqns. (2.1a) and (2.1b).

The magnitude of the ionospheric error is a function of the sunspot number, time of day, receiver location and satellite elevation angle. It can reach 150 m during periods of intense sunspot activity when observations are taken at night to satellites at low elevations. In contrast, an error of 5 m is realized during minimum sunspot numbers for measurements taken in the day to satellites at the zenith (Wells et al.,1986).

There are three methods for eliminating or reducing the ionospheric error. A method which virtually eliminates the error is the use of dual frequency data available from P-code GPS receivers. Since the ionospheric error is frequency dependent, the measurements on the L1 and L2 frequencies can be compared to remove the error, i.e. for the carrier phase,

$$d_{ion} = \lambda \left\{ \frac{f_2^2}{f_2^2 - f_1^2} \left[\phi_{L1} - \frac{f_1}{f_2}\phi_{L2} - (N_{L1} - \frac{f_1}{f_2} N_{L2}) \right] \right\} , \qquad 2.4$$

where ϕ_{L1} ... is the carrier phase measurement on L1 (cycles)

ϕ_{L2} ... is the carrier phase measurement on L2 (cycles)

f_1, f_2 ... are the L1 and L2 frequencies (cycles s^{-1})

and N_{L1}, N_{L2} ... are the ambiguities on L1 and L2 (cycles).

From Eqn. (2.4) it is seen that the carrier phase ionospheric correction is a function of the ambiguities. Since the differential carrier phase advance between L1 and L2 is generally larger than one wavelength, only the relative (i.e. over time) ionospheric correction can be recovered from carrier phase data. L2 codeless receiver technology can also be used to remove the relative ionospheric effect, however, since the absolute ionosphere cannot be determined, it has a limited application for many kinematic positioning applications.

A second method for reducing the ionospheric error is the use of a model utilizing coefficients broadcast as part of the satellite navigation message (Klobuchar,1983). This model consists of a cosine representation of the diurnal ionospheric error curve which will vary in amplitude and period depending on the user's latitude. It has been shown to be effective in removing about 50% (root mean square) of the total error.

A third method for controlling the effect of ionospheric errors is through a combination of the pseudorange and carrier phase measurements. Goad (1990) applies an adaptive filtering technique to estimate the ionospheric effect based on the code and carrier divergence. In general, however, this method will not be sensitive enough for cm-level kinematic positioning.

The effect of the ionosphere can be very significant during periods of ionospheric scintillation, where rapid fluctuations in the Total Electron Content (TEC) cause variations in the Doppler shift, hence losses of phase lock may occur (ibid). However, geomagnetic activity forecasts can be used to avoid observations during these periods.

Tropospheric Error, d_{trop}:

The effect of the troposphere is to retard the satellite signal during transmission with the degree of retardation being a function of the atmospheric conditions and the satellite elevation with respect to the receiver. The total tropospheric error is comprised of components due to the wet (up to about 11 km) and dry (up to about 40 km) troposphere.

Many models exist to estimate the tropospheric effect based on surface measurements of temperature, pressure and relative humidity, e.g. Hopfield (1963), Black and Eisner (1984). These models can estimate the dry portion of the troposphere, which accounts for about 80% of the total error, to within 2-5%. However, accurate estimation of the wet portion using surface measurements is more difficult due to vertical gradients in the meteorological data. Water vapour radiometers, which measure the vertical gradient of the water vapour, and stochastic techniques are useful in static mode, e.g. Tralli and Lichten (1990), but are generally of limited use for kinematic applications.

The effectiveness of a tropospheric model to remove the actual tropospheric delay is a function of the satellite elevation angle. For elevations above 10 degrees, accuracies are generally within a few dm, but can reach several metres at the horizon. Therefore, the use of relatively high elevation cutoff angles, say 10 degrees, or the selection of a model that performs well at low elevations, will reduce errors due to residual tropospheric effects. The modified Hopfield model was chosen for data processing since it performs relatively well at low elevations compared to other models (Goad and Goodman,1974).

Orbital Error, dρ:

The orbital error given in Eqns (2.1a) and (2.1b) contain components due to the broadcast orbital error and SA (Lachapelle et al.,1991), i.e.

$$d_\rho = f\{ d_{\rho_n}, d_{\rho_{SA}} \} , \qquad 2.5$$

where d_{ρ_n} ... is the nominal broadcast orbital error component

and $d_{\rho_{SA}}$ ... is the orbital error due to SA.

The broadcast orbital component is due to the error in the predicted satellite orbits generated at the GPS Control Segment and generally range between 5 - 25 m with peaks of 80 m being observed in some instances. However, once GPS is declared operational in 1993, this error is expected to range between 5 and 10 m. If post-mission precise ephemerides are used instead of the broadcast parameters, orbital accuracy is generally better than 5 m.

The contribution of SA to the orbital error has been estimated to be about 100 m (Kremer et al.,1989). Note that post-mission ephemerides are not affected by SA.

Satellite Clock Error, dt:

The satellite clock error is the difference between a satellite's time scale and true GPS time, with the size of the correction being different for each observed satellite. This error is predicted by the GPS Control Segment and the estimated polynomial coefficients are transmitted as part of the navigation message. The user can then correct the transmit time and measurements using the following relationship (Van Dierendonck et al.,1980),

$$dt = a_o + a_1(t - t_{oc}) + a_2(t - t_{oc})^2 \qquad 2.6a$$

$$\dot{d}t = a_1 + a_2(t - t_{oc}) \qquad 2.6b$$

where t ... is the measurement transmit time (s)

a_o, a_1, a_2 ... are the broadcast polynomial coefficients (s, s s^{-1} and s s^{-2}, respectively)

and t_{oc} ... is the time to which the coefficients refer (s).

Although the magnitude of dt can reach 1 ms (about 300,000 m), once the model is applied the residual clock prediction error is approximately 8 ns (2.4 m) assuming SA is not turned on (Russell and Schaibly,1980). When SA is turned on, however, it not only affects the orbital error, $d\rho$, it also effects the satellite clock term due to induced clock dithering. Dithering is accomplished through the injection of errors into the a_1 term which will result in a relatively short correlation time for the SA-induced error. Note that the observed satellite clock error is identical for any receiver tracking the same satellite. The implication of this is further discussed in the next section.

2.1.3 Differenced Observations and Residual Errors

The fundamental observation equations given in Eqns. (2.1) and (2.2) express the observables as a function of the geometric range as well as numerous errors. In general, many of these errors are spatially correlated between receivers tracking simultaneous satellites. This is due to the fact that some errors are satellite dependent and also that a transmitted signal will follow a similar path through the atmosphere to various receivers. The degree of correlation between errors at two receivers is a function of the separation between them.

This correlation of errors between receivers can be used to effectively remove them when two receivers track the same satellites simultaneously. For example, by differencing the fundamental phase observation for a particular satellite between two receivers, a *single difference* observable is obtained (Remondi,1984), i.e.

$$\Delta\Phi = \Delta\rho - c\Delta dT + \lambda\Delta N - \Delta d_{ion} + \Delta d_{trop} + \Delta d_{\rho} + \varepsilon_{\Delta\phi} \qquad 2.7$$

where Δ ... represents a difference between receivers.

Similar expressions can be derived for the pseudorange and Doppler frequency observables. Comparing Eqn. (2.7) to Eqn. (2.1b), it is evident that the satellite clock error, dt, has been eliminated in Eqn. (2.7). This is because the magnitude of the satellite clock error is the same for two receivers at the same measurement epoch. All the remaining terms in Eqn. (2.7) are relative between the two receivers. For example, the $\Delta\rho$ term can be expanded to give,

$$\Delta\rho = \| \mathbf{r}^s - \mathbf{r}_1 \| - \| \mathbf{r}^s - \mathbf{r}_2 \| \qquad 2.8$$

where $\mathbf{r}_1, \mathbf{r}_2$ ... are the position vectors for receivers 1 and 2, respectively.

If the coordinates of receiver 1 are known, only the position vector of receiver 2 needs to be estimated. This is the concept of *differential* positioning, where receiver 1 is at the so-called fixed monitor station while receiver 2 is located at the remote site. Using single difference observations, the parameters that must be estimated are the coordinates of the remote station, the relative receiver clock error and the relative carrier phase ambiguity. The remaining terms in Eqn. (2.7), namely the relative tropospheric, ionospheric and orbital errors, will be much smaller than the undifferenced value, due to the correlation of these errors between receivers, but will not completely cancel, so the presence of residual effects may be significant, especially for baselines greater than 30-50 km. The magnitude of these residual errors is discussed in the sequel.

By a subsequent differencing of the 'between-receiver' single difference across two different satellites, a 'between-receiver, between-satellite' *double difference* can be obtained, i.e.

$$\Delta\nabla\Phi = \Delta\nabla\rho + \lambda\Delta\nabla N - \Delta\nabla d_{ion} + \Delta\nabla d_{trop} + \Delta\nabla d_{\rho} + \varepsilon_{\Delta\nabla\phi} , \qquad 2.9$$

where ∇ ... represents a difference across satellites.

The double difference eliminates the receiver clock term, dT, from the observation equation since it is identical for phase measurements from two satellites observed at the same receiver.

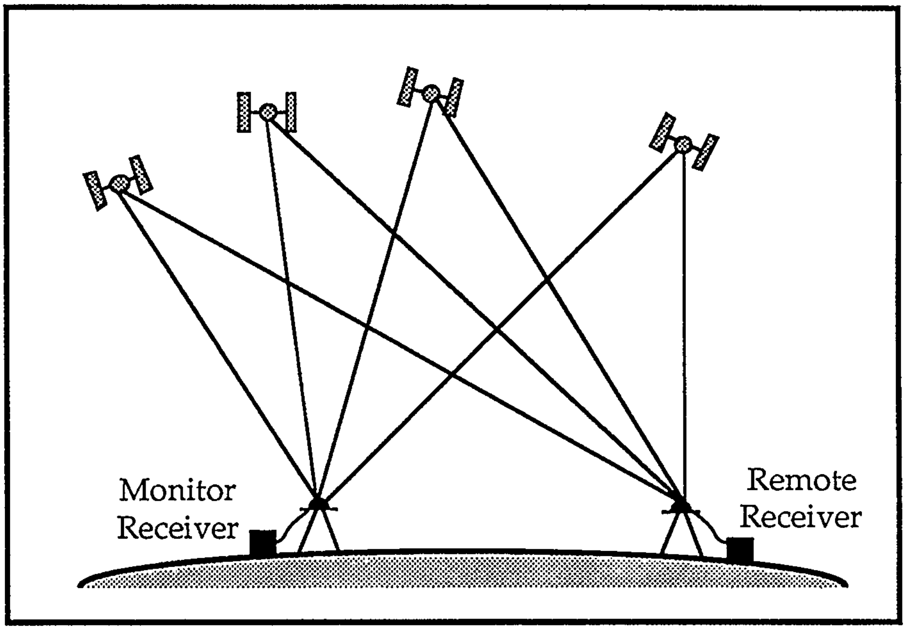

Figure 2.2
GPS Double Differencing

Illustrated in Figure 2.2 is the double difference concept. In this case, the only parameters that need to be estimated are the remote receiver's position and the double differenced ambiguities. The number of double differenced ambiguities is equal to the number of satellites tracked less one. For example, if satellites 6, 8, 9 and 11 are tracked, double differences between satellites 6-8, 6-9 and 6-11 can be formed and an ambiguity would have to estimated for each pair. In this case, satellite 6 is the so-called *base* satellite. More information on the double differencing technique can be found in Remondi (1984) and Wells et al. (1986).

The advantage of using the double differenced observable compared to the single differenced one is that the receiver clock error is eliminated. This not only means that less parameters need to be estimated, but also that the true integer nature of the ambiguity can be exploited. In the single difference case, it is very difficult to separate the initial receiver clock error from the ambiguity term. However, it should be noted that the double differenced ambiguity will diverge from an integer value for longer (say > 25 km) separations between the monitor and remote receivers due to residual errors in the troposphere, orbit, etc.

In contrast to the single difference, double differenced observations are correlated since two observations at the same receiver are differenced. The explicit form of the double difference observation covariance matrix can be found in Remondi (1984). A further differencing step can be done to form triple differences, however, since it does not apply to the kinematic case, it will not be discussed in the sequel.

The remaining errors, namely the residual troposphere, ionosphere, orbital error and multipath may significantly contribute to the error budget, depending on the separation between the monitor and remote receivers. This separation dictates the degree of spatial correlation of the errors.

The residual tropospheric error after modelling is generally between 0.2 - 0.4 ppm (Beutler et al.,1988) for elevations above 10 degrees. This translates into an error of 2 - 4 mm for a 10 km separation, which is not significant for kinematic applications. The effect of this residual error is to lengthen the distance between the monitor and remote receivers. In contrast, if L1 data are used and no modelling is performed, the residual ionospheric effect will shorten the separation between the two receivers. The magnitude of the residual ionospheric error will vary, depending on the ionospheric activity at the time of observation, the user latitude and satellite elevation angles. Georgiadou and Kleusberg (1988) have detected scale biases of 0.25 ppm to 7.5 ppm during extreme ionospheric activity, however, in mid-latitudes, the scale error should be less than a few ppm.

The nominal residual orbital error is a function of the quality of the broadcast ephemerides. If the orbit is considered to be accurate to 20 m, this translates to about 1 ppm using the following relationship:

$$\text{Orbital Scale Error} = \frac{|\Delta r|}{h_{SV}} \qquad 2.10$$

where $|\Delta r|$ ... is the orbital accuracy (e.g. 20 m)

and h_{SV} ... is the height of the satellite (about 20,200 km).

To account for discrepancies in the quality of the broadcast ephemerides, a scale error ranging between 0.5 - 2 ppm can be assumed. If post-mission ephemerides are used instead, the scale error is reduced to about 0.25 ppm. If SA is on, orbital errors of 100 m have been detected and this would translate into a scale error of 5 ppm using Eqn. (2.10). It should be re-emphasized that post-mission orbits have the effect of SA removed during the orbit improvement process.

Since multipath errors are not spatially correlated, they will not cancel through differential processing. However, for kinematic applications where multipath is generally random, it will instead increase the noise of the measurements and thus the quality of the estimated results.

Summarized in Table 2.4 is the magnitude of each of the residual GPS errors. The total residual error can be computed as follows:

$$\text{Total Error (ppm)} = \sqrt{(\Delta\nabla d_{trop})^2 + (\Delta\nabla d_{ion})^2 + (\Delta\nabla d_n)^2 + (\Delta\nabla d_{SA})^2} \quad 2.11$$

using the notation from Eqns. (2.5) and (2.9). From Table 2.4, best and worst case scenarios can be computed to be 3.1 and 5.8 ppm, respectively. This translates into an error range of 3.1 - 5.8 cm for a 10 km separation between the monitor and remote receivers.

Table 2.4
Treatment and Magnitude of Residual GPS Errors

Error Source	Treatment	Residual Error
Troposphere	modified Hopfield Model	0.2 - 0.4 ppm
Ionosphere	none (L1 only)	0.25 - 2 ppm
Orbit (broadcast)	none	0.5 - 2 ppm
Orbit (SA)	none	3 - 5 ppm

2.2 Inertial Navigation Systems

The INS measurement principle can be derived from classical mechanics where the inertial coordinate system is one in which the Newtonian equations of motion hold. Using Newton's second law of motion, the specific force on or near the earth's surface, can be described as

$$\mathbf{f}_i = \mathbf{a}_i - \mathbf{g}_i \qquad 2.12$$

where **f** is the measured specific force, **a** is the vehicle acceleration and **g** is the gravitational acceleration all in an inertial system of reference. Since the vehicle and gravitational accelerations cannot be separated during the measurement process, one component must be known to determine the other. In the case of gravity vector determination, vehicle acceleration must be removed from the measured specific force, using GPS for example (Knickmeyer,1990). In contrast, in kinematic positioning, the gravitational acceleration must be computed and subtracted from the measured specific force.

An INS measures specific force along three orthogonal axes, called accelerometers, while a triad of gyroscopes senses the angular velocity of these accelerometers to determine their orientation with respect to an inertial reference. The coordinate system in which the accelerometer measurements are made, is dependent on the INS platform that is chosen. Various types of inertial system platforms that are currently available are described in the following section.

Vehicle velocity and position can be obtained by integrating with respect to time, i.e.

$$\mathbf{v}_i(t_k) = \mathbf{v}_i(t_o) + \int_{t_o}^{t_k} \mathbf{a}_i(\tau)\, d\tau \ , \qquad 2.13a$$

$$\mathbf{r}_i(t_k) = \mathbf{r}_i(t_o) + \int_{t_o}^{t_k} \mathbf{v}_i(\tau)\, d\tau \ , \qquad 2.13b$$

where $\mathbf{v}(t_o)$ and $\mathbf{r}(t_o)$ are the vehicle velocity and position vectors at the initial time epoch. The initial position cannot be determined by an INS, hence the system performs *relative* positioning.

2.2.1 INS Hardware Configurations

Two major INS hardware configurations are currently in use, namely gimballed and strapdown systems. In gimballed systems, the gyros and accelerometers are orthogonally mounted on a platform and are used to maintain alignment with a well-defined reference frame through torquing commands. There are two types of gimballed inertial systems, namely space-stabilized and local-level systems. The difference between the two types of systems is the reference frame to which they are aligned; the space-stabilized is aligned to an inertial frame while the local-level is aligned to a local-level frame (e.g. local geodetic). A local-level INS removes the earth and vehicle rates from the measured sensor output to obtain vehicle velocity increments. in a local-level system. Thus, coordinate differences in (ϕ,λ,h) are directly obtained. In the space-stabilized system, where computations are performed in an inertial reference frame, a transformation to an earth-fixed frame has to be made. The main disadvantage of the local-level INS is that it does not perform very well at high latitudes due to the large torquing commands. More information on commercially available gimballed inertial systems can be found in Schwarz (1980).

The second type of INS is the strapdown system, where the sensors are 'hard-mounted' to the INS body, the so-called *body* frame. It senses all vehicle accelerations and rotations with respect to inertial space as it moves along a given trajectory. In this case, the transformation matrix between the body frame and the computational frame has to be obtained from the measured angular velocities and the known earth and curvature rates. This matrix is used to transform the measured specific forces to the required coordinate system. The transformed specific forces are then integrated to form vehicle velocity and position.

If real-time results are not needed, raw angular rates and specific force measurements are recorded for post-mission processing. The computational load required to process raw strapdown data into velocities and positions is more significant than for gimballed systems, but this no longer poses a problem with current computer technology.

This research focuses on the Litton LTN 90-100 strapdown system, which utilizes the ring-laser gyro (RLG) technology. The advantage of this technology compared to conventional gyros is that there are no moving parts so system reliability is increased. The cost of an inertial system using RLGs is lower and since they do not break down as often as conventional gyros, cost-effectiveness will be gained in the short and long terms. In general, however, RLGs are noisier than conventional gyros but with improved modelling and processing techniques, the LTN 90-100 has shown to rival conventional gimballed systems. In Wong (1988), the adaptation of this civilian aircraft system into a survey-quality INS is discussed in detail and is used in this research.

2.2.2 Mechanization Equations

As previously discussed, the INS measures six rates; three angular rates from the triad of gyros and the three components of specific force from the accelerometers, at a frequency of 64 Hz in the case of the LTN 90-100. Measurements are made in the *body frame*, a 3-D coordinate system that coincides with the output axes of the sensor block. Shown in Figure 2.6 is the body frame system where the Euler angles are defined as follows; roll is about the y-axis, pitch is about the x-axis and azimuth is about the z-axis.

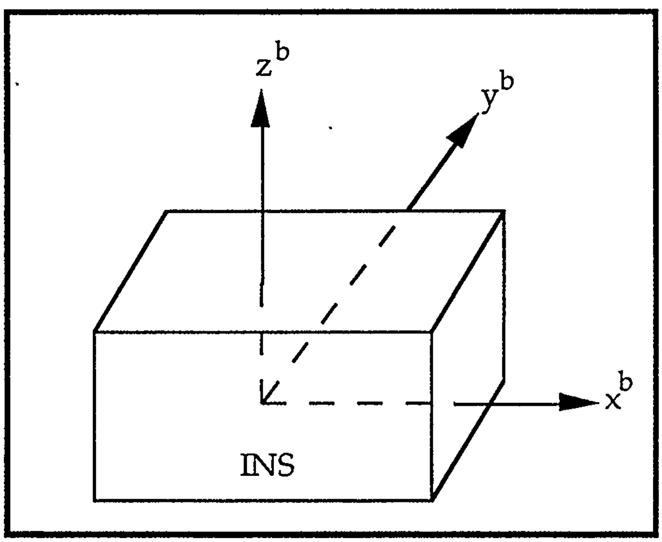

Figure 2.6
INS Body Frame

The computation frame is the system in which the data integration is performed. The wander frame, selected in this case, is similar to a local-level frame except the y-axis is not slaved to north (see Notation for definition) so there are no large torques at high latitudes.

INS mechanization equations express the transformation of the raw sensed rates and accelerations from the body to the computation frame. Two processes comprise the mechanization equations; first, the incremental changes in the Euler angles are computed by the sensed body rates, and second, the Euler angles are used to transform the sensed specific force from the body to wander frame where they can be integrated to form position and velocity. The following discussion is intended as an introduction into the mechanization scheme. Details of the explicit form of the process can be found in Wong (1988).

Transformation of Sensed Body Rates, $\tilde{\omega}_{ib}^{b}$:

The measured body angular rates with respect to the inertial frame ('i' coordinate system), $\tilde{\omega}_{ib}^{b}$, are first corrected by the gyro drifts, $\mathbf{d}_{ib}^{b}$, to give corrected angular rates in the body frame ('b' coordinate system), i.e.,

$$\omega_{ib}^{b} = \tilde{\omega}_{ib}^{b} - \mathbf{d}_{ib}^{b} \; . \qquad 2.14$$

The subscript, ib, denotes the angular rate from the body to the inertial frame, while the superscript denotes the frame in which these measurements are expressed, i.e. the body frame. Gyro drifts are laboratory-calibrated before the survey, but small deviations in these values (to account for unmodelled temperature change effects, etc.) are estimated in the error state vector.

The angular rate measurements are used to compute the rotation matrix between the body and wander frames which is required to transform the specific force measurements. This transformation matrix, R_b^w, must be continuously updated to account for vehicle rotations, i.e.,

$$R_b^w(t_k) = R_b^w(t_{k-1}) + \dot{R}_b^w(t_{k-1})\,\Delta t + \text{higher-order terms,} \qquad 2.18a$$

where

$$\dot{R}_b^w = R_b^w\,\Omega_{bw}^b\,. \qquad 2.18b$$

The term, Ω_{bw}^b, is a three parameter skew symmetric matrix containing the three components of the angular velocity vector, ω_{bw}^b. The matrix, R_b^w, is orthogonal and can be updated using the incremental rotation angles, as long as the orthogonality requirement is maintained. The incremental rotation angles, θ, are formed from the integration of the corrected angular rates, i.e.

$$\theta_{ib}^b = \omega_{ib}^b\,\Delta t\,. \qquad 2.15$$

Since the body angular rates are sensed with respect to an inertial reference frame, changes in the wander frame with respect to the i-frame must be computed to obtain the incremental angle between the body frame and the wander frame, i.e.

$$\theta^{b}_{wb} = \theta^{b}_{wi} + \theta^{b}_{ib} , \tag{2.16}$$

where the term, θ^{b}_{wi}, is the rotation angle between the inertial and wander frames while, θ^{b}_{wb}, is the corrected rotation angle between the body and wander frames. The term, θ^{b}_{wi}, is composed of the vehicle rate, ω^{w}_{ew}, i.e. the rate of rotation of the wander frame with respect to the earth frame, and the earth rate, ω^{w}_{ie}, which is the rate of rotation of the earth frame with respect to the inertial frame, and can be computed using the following:

$$\theta^{b}_{wi} = \omega^{b}_{wi}\,\Delta t = -\left[\, \mathbf{R}^{b}_{w} \left(\omega^{w}_{ie} + \omega^{w}_{ew} \right) \right] \Delta t . \tag{2.17}$$

The explicit form of this correction term can be found in Lapucha (1990).

Roll, pitch and azimuth can be easily computed from the body-wander transformation matrix, $\mathbf{R}^{w}_{b}$, i.e.

$$\begin{aligned} \mathbf{R}^{w}_{b} &= \mathbf{R}_2(\phi)\mathbf{R}_1(\theta)\mathbf{R}_3(\psi) \\ &= \begin{pmatrix} \cos\psi\cos\phi - \sin\psi\sin\theta\sin\phi & -\sin\psi\cos\theta & \cos\psi\sin\phi + \sin\psi\sin\theta\cos\phi \\ \sin\psi\cos\phi + \cos\psi\sin\theta\sin\phi & \cos\psi\cos\theta & \sin\psi\sin\phi - \cos\psi\sin\theta\cos\phi \\ -\cos\theta\sin\phi & \sin\theta & \cos\theta\cos\phi \end{pmatrix} \end{aligned} \tag{2.19a}$$

using the following formulas

$$\text{roll} = \phi = \tan^{-1}\left(\frac{-\mathbf{R}^{w}_{b}(3,1)}{\mathbf{R}^{w}_{b}(3,3)} \right) , \tag{2.19b}$$

$$\text{pitch} = \theta = \sin^{-1}\left(\mathbf{R}^{w}_{b}(3,2)\right) , \tag{2.19c}$$

$$\text{azimuth} = \psi = \tan^{-1}\left(\frac{-\mathbf{R}_b^w(1,2)}{\mathbf{R}_b^w(2,2)}\right) - \alpha\ , \qquad 2.19d$$

where α is the wander azimuth.

Transformation of Sensed Specific Force, $\tilde{\mathbf{f}}^b$:

The sensed specific force measurements, $\tilde{\mathbf{f}}^b$, must be corrected by the acceleration biases and then transformed from the body to wander frame using the appropriate transformation matrix, i.e.,

$$\mathbf{f}^b = \tilde{\mathbf{f}}^b - \mathbf{b}^b\ , \qquad 2.20a$$

and

$$\mathbf{f}^w = \mathbf{R}_b^w\ \mathbf{f}^b\ , \qquad 2.20b$$

where $\mathbf{b}^b$ is the vector of input acceleration biases. Deviations of the acceleration biases from the pre-calibrated values are estimated as part of the error state vector. As previously discussed, the specific force contains all the sensed accelerations. Therefore, in order to extract vehicle position and velocity from the raw data, the Coriolis, gravitational and centrifugal accelerations must first be removed. The Coriolis acceleration, $\mathbf{a}^w_{coriolis}$, is a function of vehicle velocity while the sum of gravitational and centrifugal accelerations is gravity which is approximated by the free-air normal gravity, γ^w. Explicit forms of these corrections can be found in Wong (1988). The specific force is then corrected to represent vehicle acceleration and integrated to form the incremental velocity at a time t_k,

$$\Delta v_k^w = (f^w - a^w_{coriolis} - \gamma^w)\,\Delta t\,. \tag{2.21}$$

Once the incremental velocity has been computed, velocities at the present epoch can be obtained as a function of the velocity at the previous epoch and an averaged velocity increment between t_k and t_{k-1} (Eqn. (2.21)), i.e.

$$v_k^w = v_{k-1}^w + \left(\frac{\Delta v_{k-1}^w + \Delta v_k^w}{2}\right). \tag{2.22a}$$

INS height can be calculated using a direct integration of the height velocity, $v_k^w(3)$,

$$h_k = h_{k-1} + v_k^w(3)\,\Delta t\;, \tag{2.22b}$$

while the wander-earth transformation matrix, R_w^e, is needed to compute latitude and longitude, i.e.

$$\phi = \sin^{-1}(R_w^e(3,3))\;, \tag{2.23a}$$

$$\lambda = \tan^{-1}\left(\frac{-R_w^e(2,3)}{R_w^e(1,3)}\right), \tag{2.23b}$$

$$\alpha = \tan^{-1}\left(\frac{-R_w^e(3,1)}{R_w^e(3,2)}\right), \tag{2.23c}$$

where

R_w^e = $R_3(180-\lambda)R_2(90-\phi)R_3(\alpha)$

$$= \begin{pmatrix} -\cos\alpha\sin\lambda - \sin\alpha\sin\phi\cos\lambda & \sin\alpha\sin\lambda - \cos\alpha\sin\phi\cos\lambda & \cos\phi\cos\lambda \\ \cos\alpha\cos\lambda - \sin\alpha\sin\phi\sin\lambda & -\sin\alpha\cos\lambda - \cos\alpha\sin\phi\sin\lambda & \cos\phi\sin\lambda \\ \sin\alpha\cos\phi & \cos\alpha\cos\phi & \sin\phi \end{pmatrix} \quad 2.23d$$

2.2.3 Alignment

The static alignment of the INS precedes the kinematic survey and is required to relate the orientation of the INS body frame to a desired coordinate system, the wander frame in this case. The initial Euler angles (roll, pitch and azimuth) of the INS are required to compute the transformation matrix, $\mathbf{R}_b^w$. Approximate INS coordinates are used to initialize the transformation $\mathbf{R}_w^e$. Alignment can be sub-divided into two phases; coarse and fine alignment.

During coarse alignment, leveling determines system roll and pitch and is computed by examination of the measured accelerations. A system is truly level when no acceleration is sensed in the horizontal axes. Hence, any acceleration in these axes can be attributed to small roll and pitch angles. These angles are estimated by first transforming the local-level velocities (output from the mechanization equations) into the body frame and using the following relationships:

$$v^b = \mathbf{R}_b^n v^n , \quad 2.24a$$

$$\text{pitch} = -\sin^{-1}\left(\frac{v_y^b}{\gamma\,\Delta t}\right) , \quad 2.24b$$

$$\text{roll} = -\sin^{-1}\left(\frac{v_x^b}{\gamma\,\Delta t}\right) . \quad 2.24c$$

Gyrocompassing to determine the north direction is performed by examination of the measured earth rate. Measured gyro rates in the body frame are transformed to the wander frame and the wander azimuth is then computed using the following:

$$\omega_{ie}^{w} = \mathbf{R}_{b}^{w}\,\omega_{ie}^{b} \,, \tag{2.25}$$

$$\text{azimuth}^{w} = -\tan^{-1}\left(\frac{(\omega_x)_{ie}^{w}}{(\omega_y)_{ie}^{w}}\right). \tag{2.26}$$

Eqn. (2.25) requires knowledge of the transformation matrix, $\mathbf{R}_{b}^{w}$, so the computation of azimuth using Eqn. (2.26) is iterative. This transformation matrix is reset every four seconds and updates to the approximate azimuth are then computed.

The coarse alignment phase usually requires about one minute of data to converge. Laboratory tests have shown that the coarse azimuth can be determined to approximately one degree and the roll and pitch to about 40 arcsec with the LTN 90-100 (Wong,1988).

INS fine alignment is performed after the coarse alignment phase and used to refine the initial Euler angles estimates and the pre-calibrated accelerometer biases and gyro drifts. The model for fine alignment is based on the Kalman filter which is presented in Chapter 3. Zero velocity updates (ZUPTS), performed ten seconds apart, are used as updates to the Kalman filter. Tests with the LTN 90-100 have shown that approximately 10-15 minutes of stationary data are required for the fine alignment phase in which accuracies in the order 10 arcsec for roll and pitch and 1 arcmin for azimuth can be achieved with the LTN 90-100 when no iterative processing is done (Schwarz and Liu,1990). More information on the alignment procedure can be found in Wong (1988).

2.2.4 Error Sources

Inertial systems are prone to time dependent errors caused by system misalignments and sensor inaccuracies. These errors can be controlled by external updates such as ZUPTS or by independent coordinate updates, such as those from GPS, however, errors will still grow between these updates. In order to investigate the main INS error sources which occur in the present case of GPS-INS integration, the discussion will be limited to short term errors, i.e. those significant between update rates of 4 - 60 seconds. Longer term errors (say 1-2 hours) are not relevant since GPS measurements are available on a frequent basis.

Table 2.5 summarizes the major INS error sources and their influence on position determination based on 10, 30 and 60 second update rates. These position errors were simulated using the estimated error magnitudes of the LTN 90-100. As can be seen from Table 2.5, for a 10 second update rate, INS errors are generally negligible as they are under 1 cm in each case. For a 30 second update rate, the major sources of error are from gyro random walk and INS misalignment. Acceleration biases and scale factor errors also contribute to a lesser extent, however, the accuracy of the INS position after 30 seconds is still estimated to be less than 10 cm. If the update rate is decreased to 60 seconds, gyro random walk and misalignment errors are the main elements in the error budget, with each contributing over 20 cm. Errors from the acceleration biases are also estimated to be about 9 cm for a total INS position error of more than 30 cm. Gyro drift does not contribute to a significant position error between updates due to the relatively short time interval.

Table 2.5
Effect of INS Errors on Position Using Various Update Rates

	Magnitude of Error (m)		
Error Source	**10 s**	**30 s**	**60 s**
Accel. Noise	0.002	0.014	0.054
Gyro Random Walk	0.001	0.050	0.200
Gyro Drift	0.002	0.005	0.020
Accel. Biases	0.003	0.023	0.090
Scale Factors	0.007	0.021	0.042
Misalignments	0.006	0.055	0.218

An error that is a result of RLG technology, is the effect of the mechanical dither. The dither is required to prevent lock-in of the two counter-rotating light beams when the gyro is subjected to low rates. When the dithered RLG goes through zero-rate, a small angular error is introduced as the two beams couple (Matthews and Welter,1989). A dither rate of approximately 400 Hz (used in the LTN 90-100) implies that lock-in occurs 800 times per second. This increases gyro random walk, which in turn reduces alignment and navigation accuracy. If the dither does not have white noise characteristics (i.e. correlated), the error will be integrated and the positioning accuracy will degrade at a faster rate.

2.3 Aerotriangulation

The concept of *aerotriangulation* was developed for economical mapping of large regions using aerial photography. Specific aspects of aerotriangulation are discussed in the following section but the intent is not to detail the fundamental concepts or historical development. Extensive information on the subject can be found in the literature, e.g. ASP (1980), Moffitt and Mikhail (1980).

2.3.1 Concepts

The two coordinate systems that are used in aerotriangulation are the photocoordinate system, defining image space, and the object system, defining ground space. Image space is defined as the region between the perspective centre, PC, and the photograph. Since the photograph is a two dimensional representation of three dimensional space, image points are measured on the photograph with respect to a two-dimensional coordinate system. However, a three-dimensional Cartesian coordinate system is used to generalize the geometry of the photograph (Moffitt and Mikhail,1980) and is called the *photocoordinate* system. Figure 2.7 shows this system in which the x and y axes are defined by the fiducial marks and the z axis is upward for a right-handed system. For aerial photography, the x-axis is taken to be in the direction of flight. The footprint of the PC is the principal point (pp) and has the coordinates (x^p_{pp}, y^p_{pp}, f) in the photocoordinate system, where f is the camera focal length. For an image point, **a**, the photocoordinates are (x^p_a, y^p_a, 0).

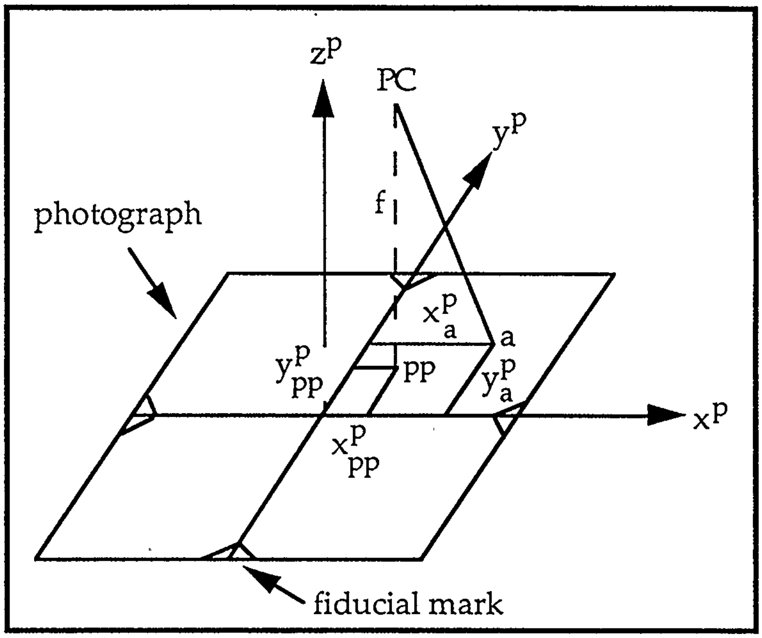

Figure 2.7
Image Space and Photocoordinate System

The position of the PC in the photocoordinate system gives the elements of *interior orientation,* which defines the form of the bundle of rays between the PC and the object point on the ground. The three interior orientation components, namely x_{pp}, y_{pp}, and f, are laboratory-calibrated for a particular camera after the manufacturing process. Once the interior orientation parameters are known and several errors corrected (e.g. lens distortion), the bundle of rays emerging from the PC at the instant of exposure can be reconstructed. The source of the errors is discussed in the following section.

Object space is referenced to a 3-D Cartesian, right-handed, coordinate system. Shown on Figure 2.8 are the object space coordinates of the PC, and of the object (ground) point, A, along with the relationship between the object and photocoordinate systems. The Z-component of the PC, Z^g_{PC}, is actually the flying height above the datum.

The relationship between the photo and object coordinate systems is computed in the *exterior orientation* process. During exterior orientation, the attitude of the camera at the time of exposure as well as the geographic position of the PC are determined. Camera attitude is generally defined by the orientation angles ω, ϕ, κ which are rotations about the x^p, y^p, and z^p axes, respectively. Therefore, the six exterior orientation parameters of a particular photograph are the PC coordinates in the object coordinate system (X^g_{PC}, Y^g_{PC}, Z^g_{PC}) and the three orientation angles (ω, ϕ, κ). At least three ground control points must be observed in the photograph to determine these six unknown parameters.

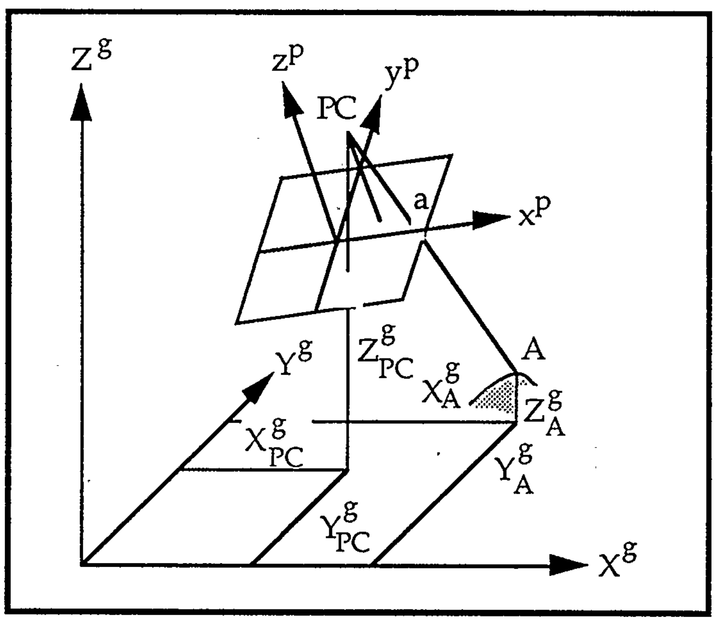

Figure 2.8
Object Coordinate System

The discussion so far has concentrated on the geometry of one single photograph. In most photogrammetric missions, however, a number of photographs covering a block are taken so maps of this area can be generated.

Photographs within a block overlap so that redundant measurements to a particular object can be made and thus the accuracy of estimated positions improved. For aerial photography, a 60% endlap along a strip and a 30% sidelap between strips is considered typical. Clearly, a higher overlap between photos along one strip or between adjacent strips, will give higher reliability of the results, but at an increased cost.

In the case that a block of photographs are taken in a mapping project, the number of required ground control points can be significantly reduced by considering all the photographs simultaneously. This *block adjustment* strategy requires horizontal ground control along the perimeter of the block and vertical control evenly distributed within the block. The number of control points is a function of the number of photos and strips in the block. An increase in the number of control points will strengthen the solution, but may also significantly increase the cost of the mapping project since each ground control point is generally pre-targetted.

The available ground control is photogrammetrically extended throughout the remaining block via tie and pass points. These points are observed on a number of photos along a strip (in the case of a pass point) and between strips (for a tie point) and are usually located on distinct features so they do not have to be pre-targetted. If ground points are replaced by control at flight level no pre-targetting is necessary and the cost-effectiveness of photogrammetry is increased significantly.

2.3.2 Observations and Error Sources

One of the fundamental observation equations in photogrammetry is based on the collinearity equations which express the relationship between the PC, image point and object point, and specifies that these three points must lie on the same line. The two collinearity equations are fundamental equations of photogrammetry and are derived using the projective transformation equations (ASP,1980), to give the following observations,

$$x_a^p = x_{pp}^p - f\frac{x_A^p}{z_A^p} + d_{lens} + d_{ref} + d_{Ecurv} + \varepsilon_{xp} \qquad 2.27a$$

$$y_a^p = y_{pp}^p - f\frac{y_A^p}{z_A^p} + d_{lens} + d_{ref} + d_{Ecurv} + \varepsilon_{yp} \qquad 2.27b$$

where x_a^p, y_a^p ... are the measured photocoordinates of point a in the image

x_{pp}^p, y_{pp}^p ... are the calibrated principal point offsets

f ... is the calibrated camera focal length

x_A^p, y_A^p, z_A^p ... are the coordinates of ground point A in the photocoordinate system

d_{lens} ... is the lens distortion correction

d_{ref} ... is the atmospheric refraction correction

	d_{Ecurv}	... is the earth curvature correction
and	$\varepsilon_{xp}, \varepsilon_{yp}$	... are the measurement errors of the photocoordinates.

Lens distortion, atmospheric refraction and earth curvature corrections can be computed and applied to the measured photocoordinates using well-known formulas, see for example Moffitt and Mikhail (1980), so they do not have to be considered in the adjustment model. The measurement noise of the photocoordinates is a function of the quality of the photography and the measurement procedure.

The principal point offsets and focal length comprise the interior orientation parameters. Any deviation in these calibrated values during photography due to environmental effects may introduce systematic errors into the estimated quantities. For conventional aerotriangulation, the effect is not generally significant due to the projective compensation effect, however, when ground control is replaced by control at flight level, errors in the interior orientation parameters may introduce large systematic errors in the estimated ground coordinates of the tie points. A discussion of the projective compensation effect as well as the influence of interior orientation errors are given in Goldfarb (1987).

The coordinates of the ground point in the photocoordinate system (x_A^p, y_A^p, z_A^p) are defined as

$$\begin{pmatrix} x_A^p \\ y_A^p \\ z_A^p \end{pmatrix} = R_g^p \begin{pmatrix} X_A^g - X_{PC}^g \\ Y_A^g - Y_{PC}^g \\ Z_A^g - Z_{PC}^g \end{pmatrix}, \qquad 2.28$$

where R_g^p is the transformation matrix from the ground coordinate system to the photocoordinate system, and (X_A^g, Y_A^g, Z_A^g) and $(X_{PC}^g, Y_{PC}^g, Z_{PC}^g)$ are the coordinates of point **A** and the PC in the ground coordinate system, respectively.

The number of unknown parameters in Eqns. (2.27) and (2.28) is six per photograph; the three PC positions and the three orientation angles (ω, ϕ, κ) found in R_g^p. Corrections to the three interior orientation parameters may also be modelled. In addition to these six unknown parameters per photo, three unknowns for the ground coordinates of every tie or pass point must also be included.

2.4 Integration Strategies

The preceding sections described the fundamental concepts of GPS, INS and aerotriangulation. In order to integrate these three measurement systems, the strength and weakness of each must be reviewed. An overview is given in Table 2.6.

Although differential GPS is a relative positioning system, almost uniform position accuracy can be determined within 30-40 km of the monitor receiver. Assuming a reasonable satellite geometry, differential GPS is not significantly affected by time dependent errors. However, carrier phase cycle slips can occur which, if not properly accounted for, will degrade the positioning accuracy. Also, initial carrier phase ambiguities must be correctly determined so position drifts will not lower the achievable accuracy. In contrast, an INS provides accurate relative positions (i.e. from one epoch to the next) but is prone to time dependent errors if frequent system updates are not made. Another advantage of an INS is the availability of attitude information. The geometric strength of aerotriangulation is derived from the intersection of the bundles of rays from overlapping photographs. It is a relative method and accuracies deteriorate if ground or camera control is not available. For the 'no ground control case', accurate camera control is needed throughout the photogrammetric block. This implies that a positioning system that provides accurate and consistent position (and possibly attitude) information is required for aerotriangulation without ground control.

Table 2.6
Measurement System Strengths and Weaknesses

System	Strength	Weakness
GPS	accurate and consistent position information	prone to carrier phase cycle slips
INS	accurate short term *relative* position, velocity and attitude	prone to systematic time dependent errors if not updated
Aerotriangulation	accurate *relative* position and attitude from intersection of bundles	systematic errors if not controlled by external information

From the above discussion, it is clear that differential GPS can meet the requirements for aerotriangulation without ground control if system limitations are eliminated. Using GPS with an INS, the carrier phase cycle slip problem can be overcome since the INS provides high accuracy in the short term. Another limitation of current GPS hardware is the data rate (generally 1 Hz) which means that position interpolation to external events (e.g. camera exposure times) must be made. Depending on the vehicle dynamics, interpolation may introduce significant errors. The high data rate INS is well-suited for accurate interpolation. INS errors can be controlled by frequent GPS updates.

The integration of GPS, INS and aerotriangulation can be performed using various strategies. Since INS errors are time dependent, the state space approach is well-suited for error estimation. The integration of GPS and INS forms a kinematic system. In contrast, aerotriangulation can be considered a static case where the errors are geometry dependent. Therefore, in order to combine GPS, INS and aerotriangulation data, the photogrammetric data must be processed in the kinematic domain or conversely, the kinematic GPS/INS data must be considered in the static case.

The kinematic strategy would be to combine all three data types in a unified method using the state space approach, for example. Using this model, the photogrammetric data could be processed sequentially, where each photograph would be considered consecutively. In this case, information derived from the photogrammetric data could be used as feedback to the GPS and INS data in order to gain redundancy in the integrated system. GPS cycle slip detection and correction may be improved with the addition of the accurate relative position and attitude from aerotriangulation. Conversely, the GPS/INS derived positions and attitude would be used to control the camera at times of exposure. However, the disadvantage of this approach is that as each photograph is processed, the size of the state vector is increased significantly due to the addition of exterior orientation elements and tie point ground coordinates. The final state vector is a function of the number photos in the block and in general, the estimation of the state errors would be unmanageable using the state space approach. Therefore, the concept of a unified approach is not practical for block triangulation.

A second approach is to estimate position and attitude with the GPS/INS data and then use this information in a subsequent photogrammetric block adjustment. This is the so-called static approach, where the camera positions are estimated (using a kinematic model) *a priori* then considered as 'static' data, i.e. it is not relevant how these camera positions are estimated. The advantage of this two-step approach is that it is in line with conventional methods for kinematic positioning and aerotriangulation. For example, the state space approach can be used in the GPS/INS case where a Kalman filter estimates the time dependent INS errors as well as the vehicle's trajectory. Information derived from the Kalman filter (i.e. camera position and associated statistics) can then be input to a batch block adjustment of the photogrammetric data. As long as the complete GPS/INS estimated statistics are transferred to the photogrammetric adjustment, the two-step approach should be as effective as the unified method. An additional advantage of separating the kinematic positioning model from the aerotriangulation is that the resulting package is more flexible, i.e. kinematic positioning can be easily applied to other applications.

For the above reasons, the two-step approach for the reduction of GPS, INS and photogrammetric data was chosen. Details of both the kinematic positioning model and the batch photogrammetric block adjustment are given in the following chapter.

CHAPTER 3

MATHEMATICAL METHODOLOGY

In this chapter, the two-step approach of GPS-INS integration for kinematic positioning and the subsequent block adjustment of photogrammetric data is developed. The state space approach for error estimation is reviewed and the Kalman filter algorithm is given. Models are first described for the kinematic GPS and dynamic INS cases. A GPS/INS integration strategy is subsequently developed which addresses the error behavior of both positioning systems. A centralized Kalman filter approach is used to merge the INS and GPS measurement data. Detection and correction of GPS carrier phase cycle slips using a predicted position from the INS is also discussed in detail.

Finally, the bundle block adjustment model for batch processing of the photogrammetric data is given with emphasis on the aerotriangulation without ground control case.

3.1 Kalman Filter Algorithm

A Kalman filter algorithm was chosen to process the data since it has many advantages compared to other estimators. Kalman filtering offers flexibility such that it can be used in either a real-time or post-mission environment. It can also accommodate measurement updates from a wide variety of sensors, GPS in this case. The derivation of the Kalman algorithm is not given here since it is well-documented in the literature, e.g. Gelb (1974) and Brown (1983), instead the fundamental aspects of the state space approach are reviewed and the application to the problem at hand is given.

System dynamics can be represented by the state space model, in which a set of first order linear differential equations express deviations from a reference trajectory, i.e.

$$\dot{x} = Fx + w \,, \tag{3.1}$$

where	x	... is the state vector (n x 1)
	$\dot{x}$	... is the time derivative of the state vector (n x 1)
	F	... is the system dynamics matrix (n x n)
	w	... is the system noise (n x 1)
and	n	... is the number of states in the state vector.

In the absence of system noise, the solution to the set of first-order homogeneous differential equations, $\dot{x} = Fx$, is as follows:

$$x_{k+1} = \Phi_{k+1,k}\, x_k \,. \tag{3.2}$$

The transition matrix, Φ, allows for computation of the state vector at any time epoch based on the state at the previous epoch. For a constant coefficient dynamics matrix **F** (stationary system), Φ can be derived by

$$\Phi = e^{F\Delta t} \tag{3.3}$$

and can be approximated using a Taylor series expansion for the case that **F** remains constant over Δt. Expanding Eqn. (3.3) and truncating after the first two terms gives

$$\Phi \approx I + F\Delta t \ , \tag{3.4}$$

where **I** is the identity matrix. The elements of the dynamics matrix for GPS/INS are given in Section 3.3.1.

While Eqn. (3.2) describes the propagation of the state vector, the covariance matrix of the state vector can be propagated between epochs t_k and t_{k+1} using the following:

$$C^x_{k+1} = \Phi_{k+1,k} C^x_k \Phi^T_{k+1,k} + C^w_{k+1,k} \ , \tag{3.5}$$

where C^x ... is the covariance matrix of the state vector (n x n)

and C^w ... is the process noise matrix (n x n).

Process noise, **w**, has an expected value of zero. The process noise matrix is derived from the integral of the spectral density matrix, **Q**, i.e. for constant Δt,

$$C^w = \int_0^{\Delta t} \Phi(\tau)\, Q(\tau) \Phi^T(\tau)\, d\tau \ . \tag{3.6}$$

Eqn. (3.6) can be approximated using the relationship given in Eqn. (3.4) to give a simplified noise covariance matrix of the form (see Gelb, 1974 for derivation)

$$C^{w} \approx Q\,\Delta t \; . \tag{3.7}$$

The advantage of using this simplified matrix is that it increases the efficiency of the filter algorithm. The elements of the process noise matrix are selected to represent the inadequacy of the Kalman state vector to correctly model the system dynamics.

The prediction equations given in Eqns. (3.2) and (3.5) can be summarized as

$$x_{k+1}(-) = \Phi_{k+1,k}\, x_k$$

and

$$C^{x}_{k+1}(-) = \Phi_{k+1,k}\, C^{x}_{k}\, \Phi^{T}_{k+1,k} + C^{w}_{k+1,k} \; ,$$

where (-) represents a predicted quantity. If measurements are available of the form

$$\mathbf{l} = \mathbf{A}\mathbf{x} + \varepsilon \; , \tag{3.8}$$

where $\mathbf{l}$ is a vector of observations, $\mathbf{A}$ is the design matrix and ε is the measurement noise, the Kalman filter update equations can be used to estimate the state vector, i.e.

$$\hat{x}(+) = \hat{x}(-) + \mathbf{K}\{\mathbf{l} - \mathbf{A}\hat{x}(-)\} \; , \tag{3.9a}$$

$$C^{x}(+) = \{\mathbf{I} - \mathbf{K}\mathbf{A}\}\, C^{x}(-) \; , \tag{3.9b}$$

$$\mathbf{K} = C^{x}(-)\,\mathbf{A}^{T}\{\mathbf{A}\, C^{x}(-)\mathbf{A}^{T} + C^{\varepsilon}\}^{-1} \; , \tag{3.9c}$$

where $\hat{x}$ ... is the estimated state vector (n x 1)

	Φ	... is the transition matrix (n x n)
	C^x	... is the state covariance matrix (n x n)
	C^w	... is the process noise matrix (n x n)
	K	... is the Kalman gain matrix (n x m)
	A	... is the design matrix (m x n)
	C^ε	... is the measurement noise matrix (m x m)
and	m	... is the number of observations.

Subscripts have been omitted in this case because filtering takes place at one instant. The (+) represents estimates after measurement update. The design matrix contains the partial derivatives of the observable with respect to the states and the Kalman gain matrix controls the influence of the update information on the predicted state vector. The vector $\{ 1 - A \hat{x} (-) \}$ is called the innovations sequence, and should have an expected value of zero.

3.2 GPS Kinematic Positioning

The following discussion of high accuracy differential GPS kinematic positioning follows the Kalman filter model development that has been successfully utilized in **SEMIKIN**, a program which incorporates an algorithm capable of cm-level kinematic positioning through post-mission processing (Cannon,1990).

3.2.1 Kinematic Model

Kinematic modelling of a vehicle's trajectory requires measurement data that describes the motion of that vehicle in a given three-dimensional (3-D) coordinate system. For the GPS-only case, kinematic positioning is accomplished using the raw GPS measurements, namely carrier phase and Doppler frequency. Pseudorange measurements may also be used, but since they have significantly higher noise characteristics than the carrier phase data, their application to high accuracy kinematic positioning is limited.

The kinematic models that describe vehicle motion in the local-level frame can be expressed as,

$$r(t) = \{\phi(t), \lambda(t), h(t)\}^T \qquad 3.10a$$

or

$$\dot{r}(t) = \{v_n(t), v_e(t), v_h(t)\}^T \qquad 3.10b$$

or

$$\ddot{r}(t) = \{a_n(t), a_e(t), a_h(t)\}^T \qquad 3.10c$$

where $r(t)$ ... is the position vector of the vehicle at time t

$(\cdot), (\cdot\cdot)$ ... are the first and second derivatives with respect to time, respectively

ϕ, λ, h ... are latitude, longitude and height, respectively

v_n, v_e, v_h ... are the velocities in the north, east and height directions, respectively

and a_n, a_e, a_h ... are the accelerations in the three directions.

In principle, the three representations in Eqns. (3.10a) - (3.10c) are equivalent if the appropriate initial values are known and the time history is continuous. However, in general this is not the case so the representation closest to the measurement is chosen. Since carrier phase and Doppler frequency measurements give position and velocity information, they can be used to estimate $\mathbf{r}(t)$ and $\dot{\mathbf{r}}(t)$. GPS does not provide raw acceleration data, so in order to determine vehicle acceleration, differentiation of Eqn. (3.10b) must be performed, however this is an unstable process. In general, the inclusion of acceleration vector will make no significant improvement in positioning accuracies in the case of moderate vehicle dynamics, so a *constant velocity* model (Schwarz et al.,1989) can be assumed where,

$$\mathbf{r}_{k+1} = \mathbf{r}_k + \dot{\mathbf{r}}_k \Delta t \,. \tag{3.11}$$

In this case a six parameter state vector, $\mathbf{x}$, is used to describe the vehicle dynamics, and can be defined as

$$\mathbf{x} = \{ \delta\phi, \delta\lambda, \delta h, \delta v_n, \delta v_e, \delta v_h \}^T \tag{3.12}$$

where δ represents a correction to the parameter. The dynamics matrix, $\mathbf{F}$, for this model is given as

$$\mathbf{F} = \begin{pmatrix} 0 & 0 & 0 & 1 & 0 & 0 \\ 0 & 0 & 0 & 0 & 1 & 0 \\ 0 & 0 & 0 & 0 & 0 & 1 \\ 0 & 0 & 0 & 0 & 0 & 0 \\ 0 & 0 & 0 & 0 & 0 & 0 \\ 0 & 0 & 0 & 0 & 0 & 0 \end{pmatrix}, \tag{3.13}$$

Since the constant velocity model assumes no vehicle acceleration during the period Δt, the elements of the process noise matrix, $\mathbf{C}^w$, are a function of the vehicle dynamics and GPS data rate. Clearly, for a high dynamic environment and a low data rate, the model will not be complete. The effect of this mismodelling is often alleviated by increasing the process noise. A better approach is to model acceleration by a Gauss-Markov model.

Eqn. (3.12) gives the state vector when only the vehicle dynamics are considered. However, from Eqn. (2.9), the carrier phase ambiguities must also be determined if double differenced carrier phase measurements are used as updates. However, if a differential static survey is performed prior to the kinematic mission, the initial integer ambiguities can be estimated and thus fixed during vehicle motion. In this case, Eqn. (3.12) would completely model the system with the ambiguities considered as known quantities. If the ambiguities are fixed to incorrect values, this can introduce time dependent errors in the estimated positions. This is demonstrated in Section 4.6. In this case, additional states can be added to absorb the effect of the incorrectly resolved ambiguities. Typically, they would be first-order Gauss Markov processes with correlation time between 0.5 and 1 hour.

3.2.2 GPS-Only Cycle Slip Detection and Correction

Since carrier phase ambiguities change when cycle slips occur, reliable cycle slip detection and correction procedures must be implemented in order to maintain highly accurate positioning. Various methods are available to detect cycle slips in kinematic data, e.g. Cannon (1987), and one that can be used with C/A code data is the comparison of the measured carrier phase with the predicted observation, determined from the measured Doppler frequency, e.g. for carrier phase prediction at time t_{k+1}

$$\hat{\Phi}_{k+1} = \Phi_k + \frac{\dot{\Phi}_{k+1} + \dot{\Phi}_k}{2} \Delta t \qquad 3.14$$

where $\hat{\Phi}_{k+1}$ ... is the predicted phase measurement at t_{k+1}

Φ_k ... is the phase measurement at t_k

$\dot{\Phi}_{k+1}$ ... is the Doppler frequency measurement at t_{k+1}

$\dot{\Phi}_k$ ... is the Doppler frequency measurement at t_k

and Δt ... is equal to $t_{k+1} - t_k$.

The absolute difference between the measured and predicted carrier phase is then compared to a threshold, and if the difference exceeds this value, cycle slips are assumed. Since Eqn. (3.14) assumes constant acceleration during Δt, the selection of the threshold is a function of the vehicle dynamics and the GPS data rate. For kinematic positioning, the threshold may reach several cycles (> 1 m), thus the ability for cm-level kinematic positioning is jeopardized. As discussed in Section 3.4, the integration of GPS with an INS is an effective solution to the GPS cycle slip detection problem.

Once cycle slips have been detected, they must be corrected, or alternatively a new ambiguity resolved. Elaborate statistical search techniques have been developed for instantaneous ambiguity resolution, however, many require the use of P code technology in order to be efficient and effective, e.g. Hatch (1990), Seeber and Wübbena (1989). Also, the presence of multipath and severe ionospheric activity can further hamper the accuracy of these techniques (Abidin,1990). A method that has been developed for use in

SEMIKIN for cases where there are at least four 'good' (i.e. cycle slip free) satellites involves the computation of the receiver position without the data from satellites containing cycle slips. This position can then be used to accurately determine the new carrier phase ambiguity for satellite(s) having cycle slips. A similar approach is discussed in Allison and Eshenbach (1989), where simulated GPS data are used to assess the feasibility of such a technique for real-time purposes, and possibly for its introduction into receiver technology. The limitation of this technique is that there must be at least four 'good' satellites, otherwise the state vector given in Eqn. (3.12) must be augmented by the new ambiguity terms, i.e.

$$x = \{ \delta\phi, \delta\lambda, \delta h, \delta v_n, \delta v_e, \delta v_u, \delta N_1, \ldots, \delta N_j \}^T \qquad 3.15$$

where δN is a correction to a satellite's new carrier phase ambiguity and j is the number of satellites having cycle slips. It should be noted that the ambiguities estimated via Eqn. (3.15) will be real numbers. However, over time they will converge, possibly to the 'true' integer value (depending on the satellite geometry, etc.).

A similar technique for cycle slip correction is implemented in the GPS/INS case, with the INS providing the computed position of the GPS antenna. As will be discussed in Section 3.4 and demonstrated using test data in Section 4.4, with GPS/INS integration there is a significant advantage because a solution is possible even if all satellites have cycle slips at any one epoch.

3.3 INS Positioning

In the case of INS positioning, vehicle movement is determined from the separation of the vehicle acceleration from the measured specific forces. Section 2.2 illustrates the concept in which the specific force is measured and models of the earth rotation and gravity field are used to extract the vehicle acceleration.

3.3.1 Dynamics Matrix

The INS state vector contains terms associated with position, velocity and misalignment of the INS as well as for residual sensor errors. These residual sensor errors are often described by six terms, namely three residual gyro drifts and three acceleration biases, and account for the error in the laboratory calibrated values. The calibrated drifts and biases are known to change between operations of the LTN 90-100 strapdown INS (Knickmeyer,1990). INS errors can then be represented by 15 states, i.e.,

$$x = \{\ \varepsilon_n, \varepsilon_e, \varepsilon_h, \delta\phi, \delta\lambda, \delta v_n, \delta v_e, \delta h, \delta v_h, d_n, d_e, d_h, b_n, b_e, b_h\ \}^T \qquad 3.16$$

where $\varepsilon_n, \varepsilon_e, \varepsilon_h$ ... are misalignments in the north, east and height directions, respectively

d_n, d_e, d_h ... are the gyro drift components

and b_n, b_e, b_h ... are the acceleration biases.

A derivation of the dynamics matrix for the 15 states is detailed in Wong (1988). The resulting F-matrix is listed below in Eqn. (3.17).

$$
\begin{bmatrix}
0 & -\omega\sin\phi & -\dot{\phi} & \omega\sin\phi & 0 & 0 & -\cos\phi & 0 & 0 & \frac{R_{21}}{s} & \frac{R_{22}}{s} & \frac{R_{23}}{s} & 0 & 0 & 0 \\
\omega\sin\phi & 0 & -\omega\cos\phi & 0 & 0 & 1 & 0 & 0 & 0 & \frac{R_{11}}{s} & \frac{R_{12}}{s} & \frac{R_{13}}{s} & 0 & 0 & 0 \\
\dot{\phi} & \omega\cos\phi & 0 & -\omega\cos\phi & 0 & 0 & -\sin\phi & 0 & 0 & \frac{R_{31}}{s} & \frac{R_{32}}{s} & \frac{R_{33}}{s} & 0 & 0 & 0 \\
0 & 0 & 0 & 0 & 0 & 1 & 0 & 0 & 0 & 0 & 0 & 0 & 0 & 0 & 0 \\
0 & 0 & 0 & 0 & 0 & 0 & 1 & 0 & 0 & 0 & 0 & 0 & 0 & 0 & 0 \\
0 & \frac{-f_h}{R_M} & \frac{f_e}{R_M} & 0 & 0 & 0 & -\omega\sin\phi & 0 & \frac{-\dot{\phi}}{R_M} & 0 & 0 & 0 & \frac{R_{21}}{R_M} & \frac{R_{22}}{R_M} & \frac{R_{23}}{R_M} \\
\frac{f_h}{R_E} & 0 & \frac{f_e}{R_M} & -\frac{f_n}{R_E} & 0 & 2\omega\tan\phi & 0 & 0 & \frac{-2\omega}{R_N} & 0 & 0 & 0 & \frac{R_{11}}{R_E} & \frac{R_{12}}{R_E} & \frac{R_{13}}{R_E} \\
0 & 0 & 0 & 0 & 0 & 0 & 0 & 0 & 1 & 0 & 0 & 0 & 0 & 0 & 0 \\
-f_e & f_n & 0 & 0 & 0 & 2R_M\dot{\phi} & 2R_E\omega\cos\phi & c & 0 & 0 & 0 & 0 & R_{31} & R_{32} & R_{33} \\
0 & 0 & 0 & 0 & 0 & 0 & 0 & 0 & 0 & -\alpha & 0 & 0 & 0 & 0 & 0 \\
0 & 0 & 0 & 0 & 0 & 0 & 0 & 0 & 0 & 0 & -\alpha & 0 & 0 & 0 & 0 \\
0 & 0 & 0 & 0 & 0 & 0 & 0 & 0 & 0 & 0 & 0 & -\alpha & 0 & 0 & 0 \\
0 & 0 & 0 & 0 & 0 & 0 & 0 & 0 & 0 & 0 & 0 & 0 & -\beta & 0 & 0 \\
0 & 0 & 0 & 0 & 0 & 0 & 0 & 0 & 0 & 0 & 0 & 0 & 0 & -\beta & 0 \\
0 & 0 & 0 & 0 & 0 & 0 & 0 & 0 & 0 & 0 & 0 & 0 & 0 & 0 & -\beta
\end{bmatrix}
$$

where c ... equals $-\frac{2\gamma}{R_E} + k$ where γ is normal gravity and k is a damping factor (if external heights are available)

R_{ij} ... is the ij term of the body to local level frame rotation matrix, $\mathbf{R}_n^b$

R_E ... is the radius of the earth (m)

R_M, R_N ... are the meridian and prime vertical radii of curvature, respectively (m)

f_e, f_n, f_h ... are the specific force measurements in the east, north and height directions, respectively (m s^{-2})

s ... is equal to 206264.8 arcsec rad^{-1}

and α, β ... are the correlation lengths for the Gauss-Markov processes of the gyro drifts and acceleration biases.

The transition matrix can be computed from this matrix using Eqn. (3.4).

For computation of the process noise matrix, the INS spectral densities must be determined. These spectral densities account for sensor noise as well as vehicle vibration. Field trials can be used to calibrate the spectral densities by comparing the estimated results with their associated statistics. However, numerous tests are required to account for different vibration characteristics under various dynamic environments.

External information must be used to update the INS in order to control the error growth. Two types of data are generally used; velocity updates, including zero-velocity updates (ZUPTS), and coordinate updates. ZUPTS require the vehicle to stop for a short period of time. Although this is not a major constraint in the land case, it is clearly not feasible in airborne or shipborne modes. Velocity and coordinate updates for moving vehicles have generally not been accurate enough for precise kinematic surveying. Therefore, the benefit of accurate 'kinematic' GPS measurement updates is that continuous high accuracy inertial positioning is possible.

3.4 GPS/INS Integration Strategy

The preceding sections described the cases when GPS and INS data are processed separately. The integration of GPS and INS gives the advantage of accurate measurement update information from GPS as well as the interpolation and cycle slip detection and correction capabilities of the INS.

For the stand-alone INS case, where zero velocities and coordinates are generally the prime external information, updates may only be available every few minutes when vehicle stops are made. However, with the addition of differential GPS measurements, accurate updates can be made at a rate of 0.25 - 4 Hz, in a static or kinematic environment. This offers flexibility in terms of operating modes, e.g. airborne, and provides a consistent accuracy of the positioning results.

If GPS measurements are used to update the INS as opposed to GPS positions (and possibly velocities), the resulting integrated state vector is identical to that given in Eqn. (3.16). This is due to the fact that the six GPS states (Eqn. 3.12) are a subset of the 15 INS states. However, as discussed in Section 3.2.1, the ambiguity terms must be determined before the mission so they can be assumed to be known quantities. Effective cycle slip detection and correction procedures must also be implemented to ensure that accuracy and reliability are maintained. In the remainder of this section, both the Kalman filter algorithm that is used to process the GPS/INS data, as well as the cycle slip detection and correction procedure are described.

The INS state vector can be augmented to include accelerometer scale factor terms which are typically 10 ppm or larger. These scale factors are unobservable unless external position or velocity are available as updates. For the INS-only positioning, these scale factors are generally estimated in a post-mission adjustment of the traverse. In the GPS/INS case they can, however, be determined directly. This will prevent accumulation of errors during acceleration and deceleration phases as they often occur in road vehicle applications.

The effect of scale factor errors on the acceleration error ($\delta\ddot{r}$) is a function of the measured specific force, i.e.

$$\delta\ddot{r}^{\,w'} = \begin{pmatrix} \delta\ddot{\phi} \\ \delta\ddot{\lambda} \\ \delta\ddot{h} \end{pmatrix} = \delta\ddot{r}^{\,w} + R_b^w \begin{pmatrix} s_1 & 0 & 0 \\ 0 & s_2 & 0 \\ 0 & 0 & s_3 \end{pmatrix} f^b = \delta\ddot{r}^{\,w} + f^w \begin{pmatrix} s_1 & 0 & 0 \\ 0 & s_2 & 0 \\ 0 & 0 & s_3 \end{pmatrix}, \qquad 3.18$$

where s_1, s_2 and s_3 are the three accelerometer scale factors (i.e. 1 + scale factor (ppm)) and the remaining terms have been previously described. The scale factors can be assumed to be constant between GPS updates thus we have

$$\dot{s} = 0\,. \qquad 3.19$$

The dynamics matrix given in Eqn. (3.17) can then be extended to include the three scale factor states, i.e.

$$F_{18\times18} = \left|\begin{array}{c|ccc} & 0 & 0 & 0 \\ & 0 & 0 & 0 \\ & 0 & 0 & 0 \\ & 0 & 0 & 0 \\ & 0 & 0 & 0 \\ & \frac{f_n}{R} & 0 & 0 \\ F_{15\times15} & 0 & \frac{f_e}{R} & 0 \\ & 0 & 0 & 0 \\ & 0 & 0 & f_h \\ & 0 & 0 & 0 \\ & 0 & 0 & 0 \\ & 0 & 0 & 0 \\ & 0 & 0 & 0 \\ & 0 & 0 & 0 \\ & 0 & 0 & 0 \\ \hline 0_{3\times15} & & 0_{3\times3} & \end{array}\right| \qquad 3.20$$

The frequent updates available from GPS are well-suited for determination of the INS accelerometer scale factor errors. However, since the main application of this research is for airborne positioning, where the velocity is generally constant, the augmentation of the 15 state vector by the scale factor terms was not included.

The approach of using GPS measurements as linear functions of the velocity and position states is called *centralized* Kalman filtering, as opposed to the use of separate GPS and INS filters, denoted as a *de-centralized* filter, see Wei and Schwarz (1990) for formulas and a comparison. Lapucha (1990) discusses the de-centralized approach where a six-state Kalman filter (Eqn. 3.12) is used to process the GPS data to estimate position and velocity. These are then fed into the Kalman filter containing the 15 INS states (Eqn. 3.16). However, since the six GPS states are a subset of the INS states assuming double difference processing and known ambiguities, consolidating the two systems into one filter reduces processing time significantly. The centralized approach gives a 'tighter' integration in that the fundamental GPS observables are used as updates, and is especially beneficial for real-time applications where processing speed is a major concern (see Dayton and Nielson,1989). Also, GPS updates with less than four observations can be made using a centralized filter. In Wei and Schwarz (1990), no statistically significant differences between the two approaches are reported.

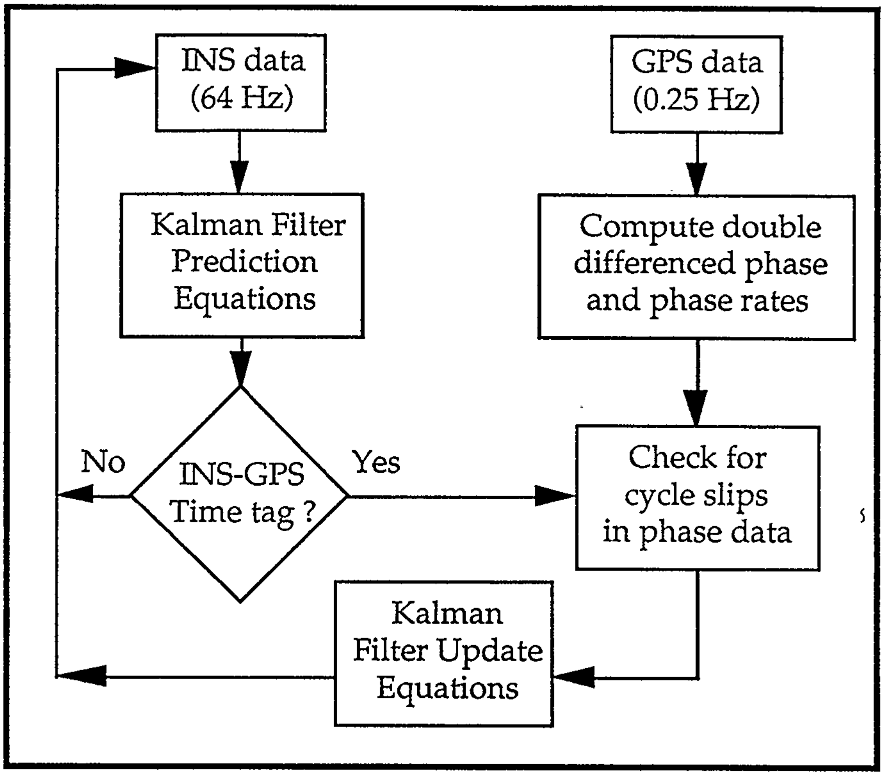

Figure 3.1
GPS/INS Integration Scheme

An overview of the integration approach is given in Figure 3.1 where the INS defines the reference trajectory while the much lower rate GPS measurements are used as updates to that trajectory. The near-continuous data rate of the INS is well-suited for position-referencing external events such as camera exposures. This is further discussed in Chapter 5 for the aerotriangulation case.

GPS double differenced carrier phase and Doppler frequency measurements provide the update data in the case of GPS/INS integration using the centralized approach. The design matrix, **A**, used in the Kalman update equations contains the partial derivatives of the GPS observations with respect to the elements of the state vector (for satellites i to n where i is the base satellite), i.e

$$
\mathbf{A} = \begin{vmatrix}
0 & 0 & 0 & \frac{\partial \Delta\nabla\Phi^{ij}}{\partial \phi_r} & \frac{\partial \Delta\nabla\Phi^{ij}}{\partial \lambda_r} & 0 & 0 & \frac{\partial \Delta\nabla\Phi^{ij}}{\partial h_r} & 0 & 0 & 0 & 0 & 0 & 0 & 0 \\
: & : & : & : & : & : & : & : & : & : & : & : & : & : & : \\
0 & 0 & 0 & \frac{\partial \Delta\nabla\Phi^{in}}{\partial \phi_r} & \frac{\partial \Delta\nabla\Phi^{in}}{\partial \lambda_r} & 0 & 0 & \frac{\partial \Delta\nabla\Phi^{in}}{\partial h_r} & 0 & 0 & 0 & 0 & 0 & 0 & 0 \\
0 & 0 & 0 & \frac{\partial \Delta\nabla\dot{\Phi}^{ij}}{\partial \phi_r} & \frac{\partial \Delta\nabla\dot{\Phi}^{ij}}{\partial \lambda_r} & \frac{\partial \Delta\nabla\dot{\Phi}^{ij}}{\partial v_n} & \frac{\partial \Delta\nabla\dot{\Phi}^{ij}}{\partial v_e} & \frac{\partial \Delta\nabla\dot{\Phi}^{ij}}{\partial h_r} & \frac{\partial \Delta\nabla\dot{\Phi}^{ij}}{\partial v_h} & 0 & 0 & 0 & 0 & 0 & 0 \\
: & : & : & : & : & : & : & : & : & : & : & : & : & : & : \\
0 & 0 & 0 & \frac{\partial \Delta\nabla\dot{\Phi}^{in}}{\partial \phi_r} & \frac{\partial \Delta\nabla\dot{\Phi}^{in}}{\partial \lambda_r} & \frac{\partial \Delta\nabla\dot{\Phi}^{in}}{\partial v_n} & \frac{\partial \Delta\nabla\dot{\Phi}^{in}}{\partial v_e} & \frac{\partial \Delta\nabla\dot{\Phi}^{in}}{\partial h_r} & \frac{\partial \Delta\nabla\dot{\Phi}^{in}}{\partial v_h} & 0 & 0 & 0 & 0 & 0 & 0
\end{vmatrix} \qquad 3.21
$$

where $\frac{\partial \Delta\nabla\Phi^{ij}}{\partial \phi_r}$ is the partial derivative of the double differenced carrier phase with respect to the remote receiver latitude, and $\frac{\partial \Delta\nabla\dot{\Phi}^{ij}}{\partial v_n}$ is the partial derivative of the double differenced Doppler frequency with respect to the remote north velocity (similarly for the longitude and height components). The superscripts on the observable indicate the satellites to which the double difference measurement is taken. For the carrier phase, $\Delta\nabla\Phi^{ij}$, the partial derivative is computed as follows;

$$
\frac{\partial \Delta\nabla\Phi^{ij}}{\partial \phi_r} = \frac{\partial \Delta\nabla\Phi^{ij}}{\partial x_r}\frac{\partial x_r}{\partial \phi_r} + \frac{\partial \Delta\nabla\Phi^{ij}}{\partial y_r}\frac{\partial y_r}{\partial \phi_r} + \frac{\partial \Delta\nabla\Phi^{ij}}{\partial z_r}\frac{\partial z_r}{\partial \phi_r} . \qquad 3.22
$$

Explicit expressions for the components in Eqn. (3.22) as well as the partial derivatives of the carrier phase with respect to longitude and height are given in the Appendix. Doppler frequency partial derivatives can also be found in the Appendix.

Since the raw GPS measurements are double differenced, the resulting observations are correlated (Remondi,1984). However, this correlation was neglected in order to increase the numerical efficiency of the data processing. This will not significantly affect the quality of the positioning results.

Optimal smoothing, a post-mission technique for improving the accuracy of the estimated results using all the data collected during the mission, can be very effective for INS positioning where updates are relatively infrequent (Wong,1988). In this case, time-dependent INS errors increase significantly between ZUPTS or coordinate updates, so optimal smoothing will reduce much of this error. However, in the GPS/INS case, measurement updates are available at a high data rate, e.g. 0.25 - 4 Hz, so INS errors are continually controlled. Therefore, optimal smoothing will not significantly improve the estimated results. For this reason, optimal smoothing was not implemented and will not be further discussed in the sequel. However, traverse position closures may be used to eliminate initial ambiguity resolution errors.

3.4.1 Cycle Slip Detection and Correction Algorithm

The success of the centralized filtering scheme is dependent on the ability of the integrated system to detect and correct cycle slips in the GPS carrier phase data. If this can be done properly, the GPS phase data (or alternatively ambiguity) can be corrected and no additional terms need to be added to the state vector given in Eqn. (3.16).

Many methods exist for the detection and correction of cycle slips in the kinematic GPS-only case. One such method which uses the Doppler frequency observation was discussed in Section 3.2.2. An alternative method is to use reliability analysis. In this case, statistical testing based on a comparison of the innovations sequence, i.e. $\{ 1 - A \hat{x}(-) \}$ in Eqn. (3.9a), and a Chi-squared test statistic is performed to determine if cycle slips occurred. *Minimum Detectable Biases* (MDB) can be computed which represent the minimum number of carrier phase cycle slips that can be detected by the test statistics (Teunissen,1989). Clearly, it would be desirable for the MDB to be less than one cycle for cm-level kinematic positioning to be achieved, however, as shown in Lu and Lachapelle (1990), the magnitude of the MDB is a function of satellite geometry which is directly related to the number of satellites tracked. Although an MDB of 0.5 cycles was shown for the case of cycle slips on one satellite when a total of seven satellites were tracked, the MDB increased to 15 cycles with cases of only four satellite geometry. When less than four satellites are tracked due to severe satellite masking, this reliability analysis technique is rendered ineffective. In this case, an 'independent' positioning system will benefit the cycle slip detection and correction process.

The high relative accuracy of the INS can be used for this purpose. By using the predicted GPS antenna position at the measurement epoch in the computation of the 'approximate' double difference, it can be compared to the measured double difference (to form the innovations sequence) using the following relationship,

$$\delta = \frac{\Delta\nabla\rho}{\lambda} - \Delta\nabla\phi \ , \qquad 3.23$$

where δ ... is the difference between the computed and measured double difference (cycles)

$\Delta\nabla\rho$ ... is the computed double difference (m)

λ ... is the carrier phase wavelength (m cycle^{-1})

and $\Delta\nabla\phi$ ... is the measured double difference (cycles).

The absolute value of δ is then compared with a cutoff threshold to determine if cycle slips have occurred since the last GPS measurement epoch, i.e.

$$|\delta| > \text{threshold ?} \qquad 3.24$$

Obviously, the threshold must be less than one cycle (e.g. 0.85 cycles) if positioning accuracies at the cm-level are required. If the threshold is larger, there is a risk that small cycle slips will not be detected in the GPS carrier phase data. Not only will positioning accuracies be reduced, the system reliability will be decreased since the statistics of the estimated quantities will not reflect the presence of undetected cycle slips. However, if the threshold is exceeded, the ambiguity on that particular double difference pair can be corrected by the number of cycles slipped using the equation,

$$N_{new} = N_{old} - \text{nint}(\delta) \ , \qquad 3.25$$

where N is the ambiguity and nint is the 'nearest integer' function (reflecting the integer nature of a cycle slip). It is not even necessary to know on which satellite the slip occurred, i.e. the base or non-base satellite. The advantage of correcting the ambiguity instead of the raw data is that the correction is instantaneous, rather than correcting all subsequent measurements by the cycles slipped. Figure 3.2 summarizes the cycle slip detection and correction scheme. The benefit of GPS/INS integration for cycle slip detection and correction is that the number of satellites that have cycle slips at any one instant is irrelevant. In contrast, GPS-only positioning requires at least four cycle-slip free measurements to detect cycle slips on the redundant measurements.

In order to correct cycle slips at the one cycle level (≈ 20 cm), the relative accuracy of the INS must be good to a few cm between GPS measurement epochs. Therefore, a high GPS data rate is beneficial to ensure that this accuracy criterion is met. Periods of satellite shading that cause GPS data gaps may reduce the ability of the INS to correct cycle slips below the one cycle threshold. This issue is further discussed in Section 4.5.

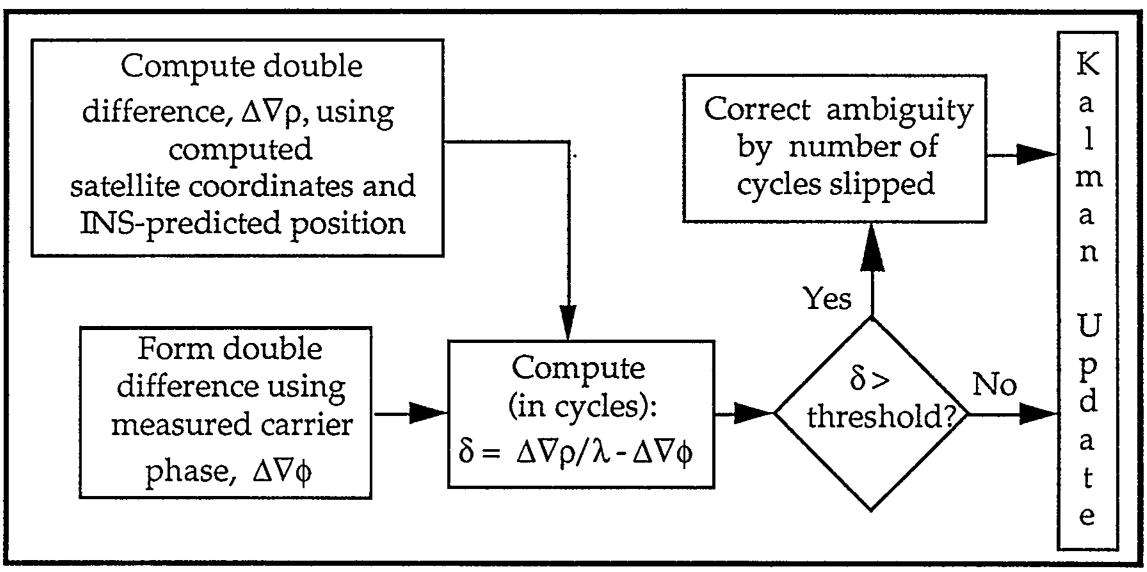

Figure 3.2
GPS/INS Cycle Slip Detection/Correction Scheme

3.4.2 GPS/INS Software Design

A software package, **GPSINS**, was developed by the author which implements a centralized Kalman filter for estimation of the 15 states using the raw INS and GPS data. The program, written in FORTRAN for use on a personal computer, incorporates many aspects of the **SEMIKIN** package (Cannon,1990), as well as INS modules developed by Wong (1988). The integration of GPS and INS data and the implementation of the cycle slip detection and correction scheme were specifically developed for the **GPSINS** program. The program was designed to accommodate a range of dynamic environments.

GPS raw data are corrected for the satellite clock errors using the broadcast model, as well as for the tropospheric effect using a modified Hopfield model (Goad and Goodman,1974). Ionospheric correction capabilities were not introduced into the program since only C/A code data were to be processed. Along with the capability of GPS measurement updates, the program can also accommodate ZUPTS and coordinate updates. These are used in the fine alignment stage. Figure 3.3 outlines the main aspects of the **GPSINS** package.

3.5 Aerotriangulation Adjustment Model

The adjustment of a block of photographs can be performed using a number of models. One such model is the *independent model adjustment* (Blais,1985), where all the models are simultaneously adjusted to the ground control. An alternative approach which was selected for this research is the *bundle block adjustment*. The use of this model is direct, rigorous and relatively easy to implement the aerotriangulation without ground control

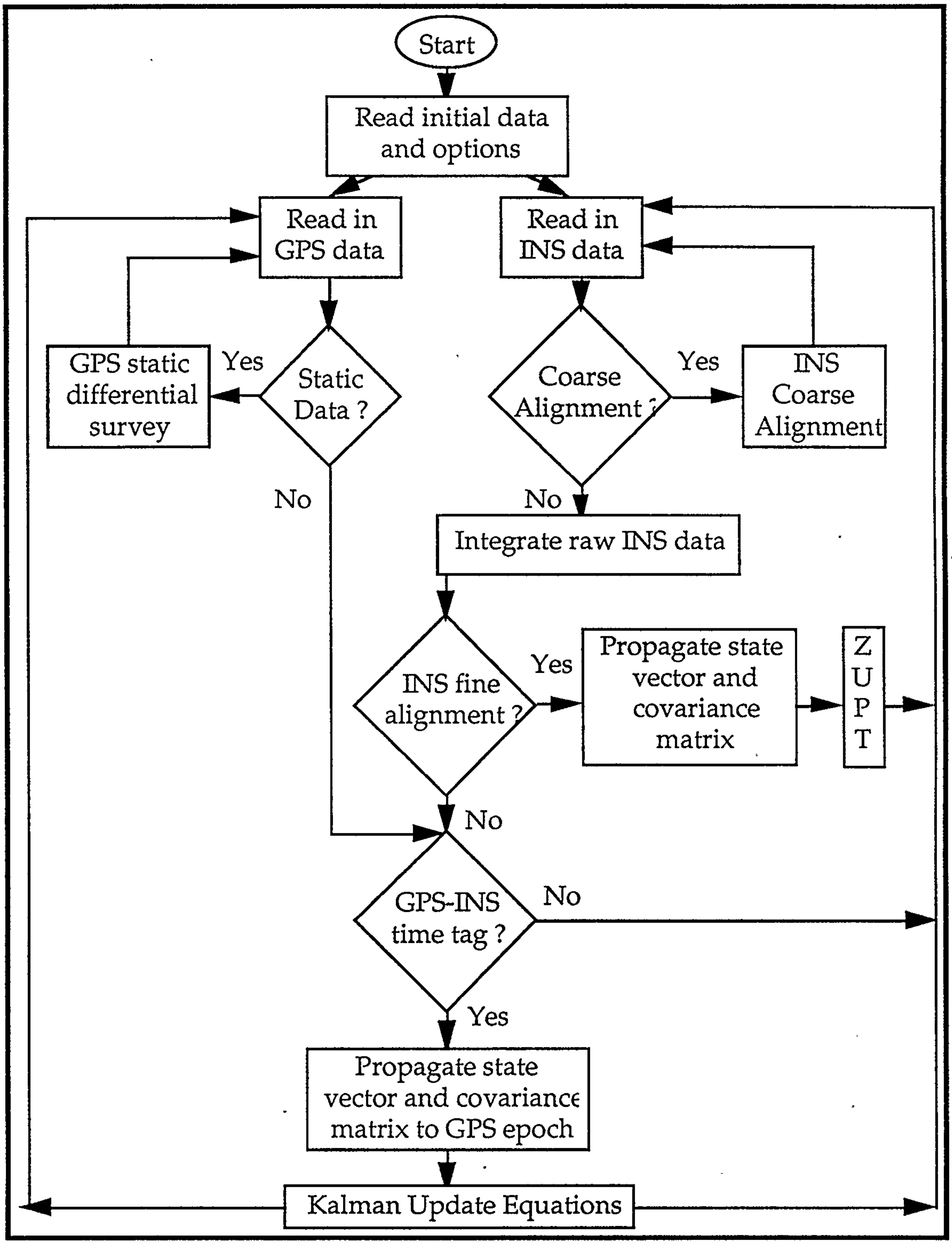

Figure 3.3
Outline of GPSINS Package

concept. It is based on the rotation and translation of each bundle, i.e. the set of rays originating at the PC and passing through the ground points, in space into such a position that all rays going through the photographic positions of each ground control point intersect at the correct object space point (Moffitt and Mikhail,1980).

The bundle adjustment uses the collinearity equations given in Section 2.3.1. There are six per photograph; the three PC positions and the three orientation angles (ω, ϕ, κ) found in R_g^p, as well, three unknowns for the ground coordinates of every tie or pass point must also be included. Corrections to the three interior orientation parameters (i.e. a *self-calibrating* bundle adjustment) has not been implemented.

The observations in Eqns. (2.27a) and (2.27b) are adjusted using a standard least-squares approach utilizing *a priori* information (Vanícek and Krakiwsky,1986), i.e.

$$\hat{x} = x_0 + \delta \qquad 3.26a$$

$$\delta = -(A^T C_\varepsilon^{-1} A + C_{xo}^{-1})^{-1} (A^T C_\varepsilon^{-1} w + C_{xo}^{-1} w') \qquad 3.26b$$

where x_0 is the vector of approximate values of the unknown parameters, C_{xo}^{-1} is its associated covariance matrix, w is the misclosure vector, and w' is the vector of the differences between the *a priori* and adjusted parameters (null on the first iteration). All other terms in the above equations have been previously defined.

Approximate coordinates of the PCs can be estimated using an index map of the photography, and zero can be assumed for ω and ϕ, since the camera is nearly vertical during photography. The flight direction can be used as an approximation to κ. Finally, initial ground coordinates of the tie and pass points can be estimated using space intersection.

The *a priori* covariance matrix of the parameters expresses the uncertainty in the selected initial values. For conventional aerotriangulation, the variances of the PCs is relatively large, say 10,000 m^2, and also of the orientation angles, e.g. 25 deg^2. In contrast, the ground points will have a small variance depending on how they were established, for example 1 cm^2. The variance of the tie point ground coordinates will generally be large, say 10,000 m^2.

The net result of the bundle adjustment are corrected PC coordinates and orientation angles for each photograph, corrected ground coordinates (with small corrections depending on the *a priori* variance) and corrected tie and pass points.

For the case of aerotriangulation without ground control, all ground points are considered as tie or pass points, hence a large variance will be assumed for each. However, if PC coordinates can be determined independently, as in the case of GPS/INS, positions and variances from the GPS/INS estimator can be used as *a priori* information in the bundle adjustment. Covariance information between the three position components can also be included in the bundle adjustment. If accurate orientation angles can be estimated from the INS data, they may also be included as *a priori* information.

One problem that may arise in aerotriangulation without ground control concerns the datum to which the ground positions refer. In many cases, ground control refers to a local datum, and the estimated tie points must also be reported in this system for map generation. In contrast, GPS is referenced to WGS-84, so if GPS/INS-derived positions are only used in the bundle adjustment, the estimated tie ground points will refer to this system. The transformation between the local system and WGS-84 may not be known, so a datum problem will arise. Clearly, the most effective means of treating this problem is to establish the WGS-84 coordinates of three tie points using static GPS techniques, so the transformation can be explicitly determined. This problem is further discussed in Chapter 5.

The feasibility of using GPS/INS-derived PC positions instead of, or in addition to conventional ground control by means of the bundle block adjustment is investigated in Chapter 6.

CHAPTER 4

RESULTS - LAND CASE

In order to assess the GPS/INS integration methodology and cycle slip detection and correction scheme discussed in Chapter 3, a detailed analysis of a land kinematic test was done. By establishing the feasibility of GPS/INS for precise kinematic positioning in land mode, system improvements can be made to overcome certain limitations before the airborne case is investigated. This chapter presents land mode results of a kinematic test on a well-controlled traverse.

4.1 Test Description

The land vehicle data were collected on May 10, 1990, in the Kananaskis region, located approximately 80 km west of Calgary. This region is a mountainous area which is heavily forested, making satellite masking a potentially serious problem. An 8 km stretch of Highway 40, where a series of control points had previously been established, was used for the test. These control points are located on each side of the road for easy vehicle accessibility and are accurate to a few cm relative to the monitor station, also located in the area. Figure 4.1 illustrates the layout of the traverse as well as the six control points that were occupied by the vehicle during the campaign.

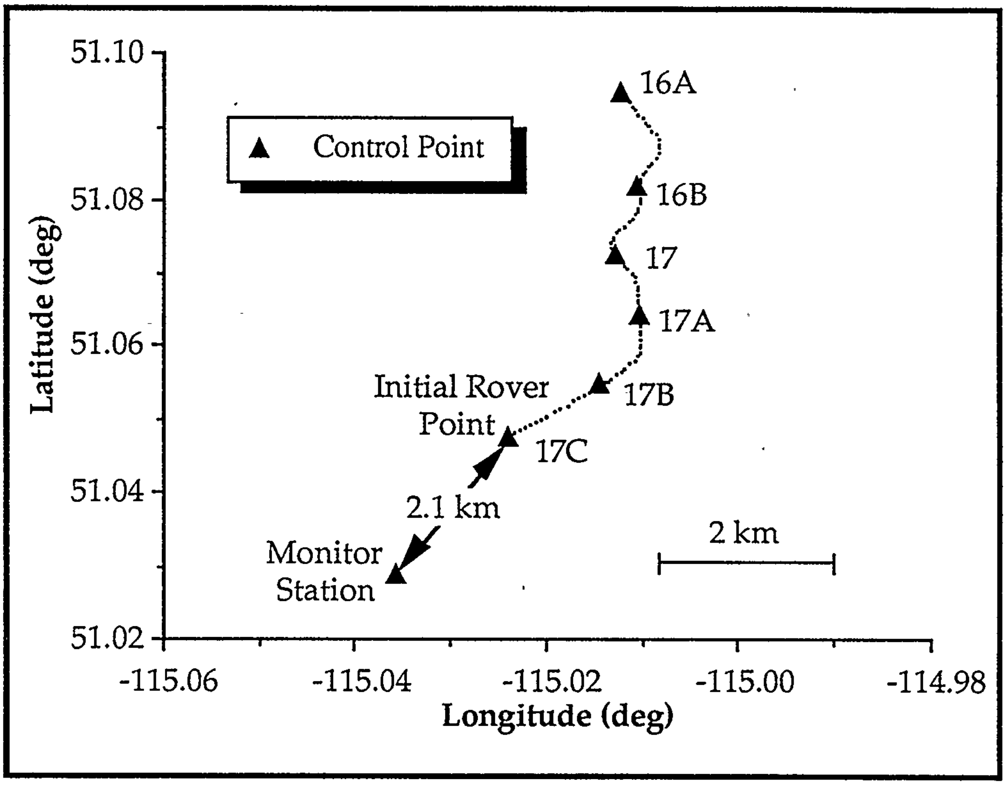

Figure 4.1
Land Test Trajectory

Data were collected using two Trimble 4000SX GPS receivers (C/A-code, five channels), one installed in a vehicle and the other located at the monitor station. Also mounted in the vehicle was the Litton LTN 90-100 strapdown INS. Portable computers were used in the vehicle as well as at the monitor station to record the raw GPS/INS and GPS data, respectively. The remote GPS antenna was mounted on a lever arm attached to a rack on the vehicle roof. In this way, the antenna could be fixed during vehicle movements, but accurately centered over control points near the vehicle when it was stopped. See Lapucha et al. (1990) for more details concerning the hardware configuration. Table 4.1 summarizes the details of the test. Five satellites were tracked for the duration of the 65 minute run. The geometric dilution of precision (GDOP), shown in Figure 4.2, was approximately six for the entire run. SA, although implemented at the time of this test, was not a concern since the separation between the monitor and remote receivers was less than 8 km (Tolman et al., 1990).

Table 4.1
Summary of GPS/INS Land Test Data

Region:	**Kananaskis Country**
Date:	**May 10, 1990**
GPS:	- 2 Trimble 4000SX receivers (C/A) - 0.25 Hz data rate (i.e. 4 seconds) - 5 Block I satellites: 6,9,11,12,13
INS:	- LTN 90-100 strapdown system - 64 Hz data rate
Test:	- 65 minute duration - Max. vehicle speed of 65 km h^{-1}
Control:	- 6 control points on each side of road - accurate to a few cm

Raw GPS data were collected at a 0.25 Hz rate, the maximum Trimble 4000SX raw data output rate when logging to an external computer. In contrast, INS data were recorded at a 64 Hz rate. Time tagging between the GPS and INS was performed via the computer and is estimated to be accurate to a few ms on average. A second generation time-tagging algorithm was used in this test since timing problems were encountered with previously collected airborne data (see Chapter 5).

The land test was conducted using the 'semi-kinematic' approach, for details see e.g. Cannon (1990). An initial survey of approximately ten minutes was performed between the initial remote point (station 17C) of the traverse and the monitor station (also shown in Figure 4.1), a baseline length of about 2.2 km. This data could then be used in post-processing for INS fine alignment as well as to determine the correct GPS integer ambiguities. After initialization, the vehicle was driven at a speed of 65 km h^{-1} to the next point along the traverse, at which the antenna was centered over the control point. This point and subsequent points along the traverse were occupied for about 2-3 minutes in order to record redundant GPS data.

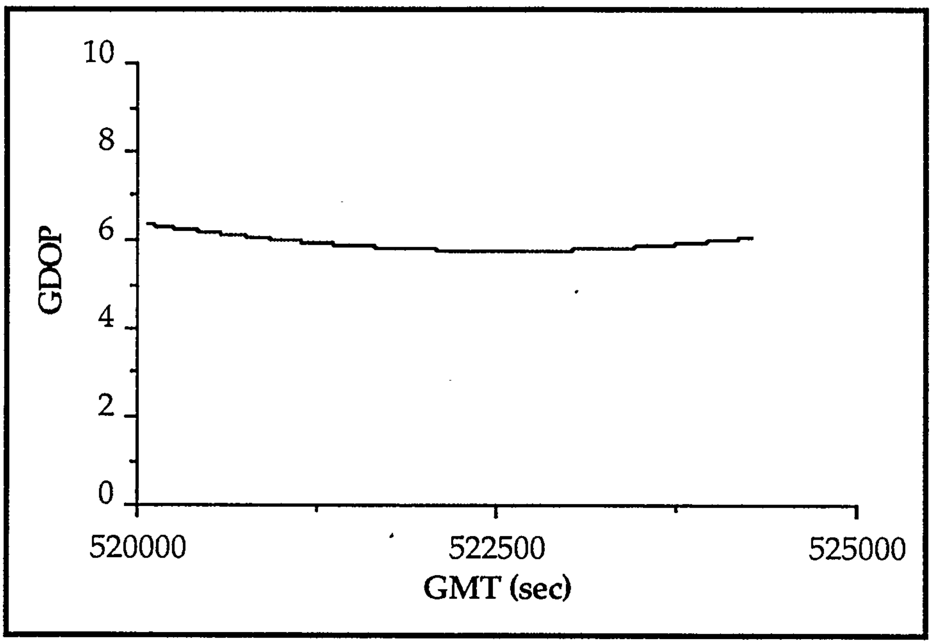

Figure 4.2
Land Test Geometric Dilution of Precision

4.2 GPS/INS Land Data Processing

The land data were processed using the **GPSINS** program which uses the methodology previously described in Chapter 3. Table 4.2 gives the user-selectable input parameters that were used in the Kalman filter algorithm. In this way, the statistical assumptions represented in the standard deviations and spectral densities can be modified depending on the dynamic environment of the vehicle, in this case land mode.

The initial standard deviations of the position and velocity components are a reflection of the knowledge of the initial point; in this case the position is known to ± 10 cm from the GPS static survey and the velocity is known to ± 1 mm s^{-1} since the vehicle was stationary. Similarly, the initial statistics of the misalignment states are related to the knowledge of those parameters after the coarse alignment procedure using an LTN 90-100 (Wong,1988). Note that roll and pitch components are more accurately determined than the azimuth component. The standard deviations of the INS gyro drifts and acceleration biases reflect the uncertainty in the values calibrated in the laboratory.

Table 4.2
GPS/INS Kalman Filter Input Parameters for Land Data

Parameter	Initial Standard Deviation (1σ)	Spectral Density	Correlation Length
Position	0.1 m	0	-
Velocity	0.001 m s^{-1}	$2.5*10^{-7}$ m^2 s^{-3}	-
Misalignments	40 arcsec (roll,pitch) 3600 arcsec (azimuth)	1 $arcsec^2$ s^{-1}	-
Gyro Drifts	0.01 deg h^{-1}	$1.39*10^{-9}$ deg^2 h^{-3}	144000 s
Accel. Biases	0.0001 m s^{-2}	$1.39*10^{-12}$ m^2 s^{-5}	144000 s

The spectral densities that were selected for the land data are a representation of the inadequacy of the 15 Kalman states (Section 3.3) to correctly model the vehicle dynamics in land mode. For example, the velocity spectral densities, when integrated to get process noise, will allow the velocity components to change when the vehicle is experiencing accelerations. The sensitivity of the positioning accuracy with respect to the misalignment spectral densities was very low in the case of the land data so the selection of the magnitudes of the spectral densities for the misalignments was not critical. The correlation length and spectral densities of the gyro drifts and acceleration biases allow for the slow time variation in these parameters due to unmodelled temperature change effects and other phenomenon (Knickmeyer,1990).

After the INS coarse alignment, the estimated coordinates determined from the differential GPS solution were used as coordinate updates to the Kalman filter. When the vehicle was moving between control points on the traverse, GPS measurements were used as updates to the filter as outlined in Section 3.4. However, when the vehicle was collecting static data at control points, the two systems remained independent and ZUPTS were used to update the filter instead of raw GPS data. At the end of the static data, GPS-derived coordinates were used to update the INS.

4.3 GPS versus GPS/INS

Since no independent 'kinematic' control was available to estimate the achievable accuracy of GPS/INS in motion, results at the stationary points were used to assess the positioning accuracy between points. In order to determine the quality of the GPS data, measurements were first processed with **SEMIKIN** (Cannon,1990); no cycle slips were detected in the carrier phase data. Figure 4.3 shows the differences between the GPS-only **SEMIKIN** solution and the control coordinates at the six points along the traverse. The differences are generally less than 5 cm throughout the run. A previous investigation comparing **SEMIKIN** to Ashtech's **KINSURVY** program showed sub-centimetre agreement between the two solutions, even during the kinematic segments of the traverse (Cannon et al., 1990) when the carrier phase tracking bandwidth was obviously wider. From Figure 4.3, it can therefore be assumed that the accuracy of the GPS-only solution between the static points is compatible with the accuracy at these points. Using the expected residual GPS errors given in Table 2.4, GPS should provide positions with an accuracy of 2-5 cm (1σ). Considering the control accuracy is a few cm, the results shown Figure 4.3 are within these expected values.

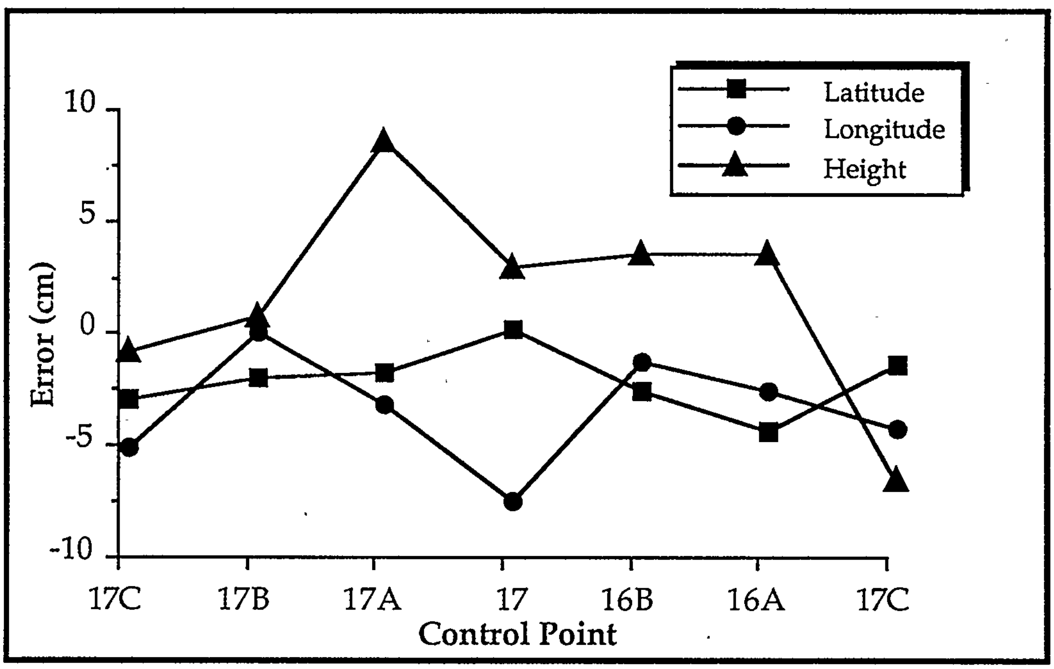

Figure 4.3
Semi-Kinematic GPS Results

The integration of GPS and INS will improve the cycle slip detection/correction capability as well as the reliability of the estimated coordinates. No cycle slips were detected in the GPS phase data collected in the land vehicle, so there should be a high level of compatibility between the estimated GPS-only and GPS/INS positions. Table 4.3 gives a statistical summary of the differences between these two solutions at each of the kinematic check points along the trajectory. The root mean square (RMS) differences for latitude, longitude and height are 0.5, 0.7 and 1.3 cm, respectively, indicating that the two solutions are virtually identical. Also, the mean values are zero, confirming that there are no significant unmodelled systematic effects remaining in the INS data and the vehicle dynamics have been modelled properly. The maximum differences between the two solutions is less than 4 cm in all three coordinates. Figure 4.4 shows a plot of the differences between the GPS and GPS/INS heights for the kinematic land data. The breaks in the figure are during periods of vehicle stops when no comparisons were made.

Table 4.3
Comparison of GPS-only Kinematic Positioning with GPS/INS
(Sample size = 356)

Coordinate	Mean (cm)	RMS (cm)	Abs. Max. (cm)
ϕ	0.0	0.5	-1.9
λ	0.0	0.7	3.2
h	0.0	1.3	3.5

The results listed in Table 4.3 establish the compatibility of GPS and INS using the Kalman filter algorithm described in Chapter 3 under the vehicle dynamics encountered in this test. Using this statistically significant sample, it can be seen that the INS will be effective for interpolation between the 4 second GPS measurement updates. This is very important when accurate positions are needed at events occurring between these updates. The 64 Hz INS data gives a near-continuous profile of the trajectory.

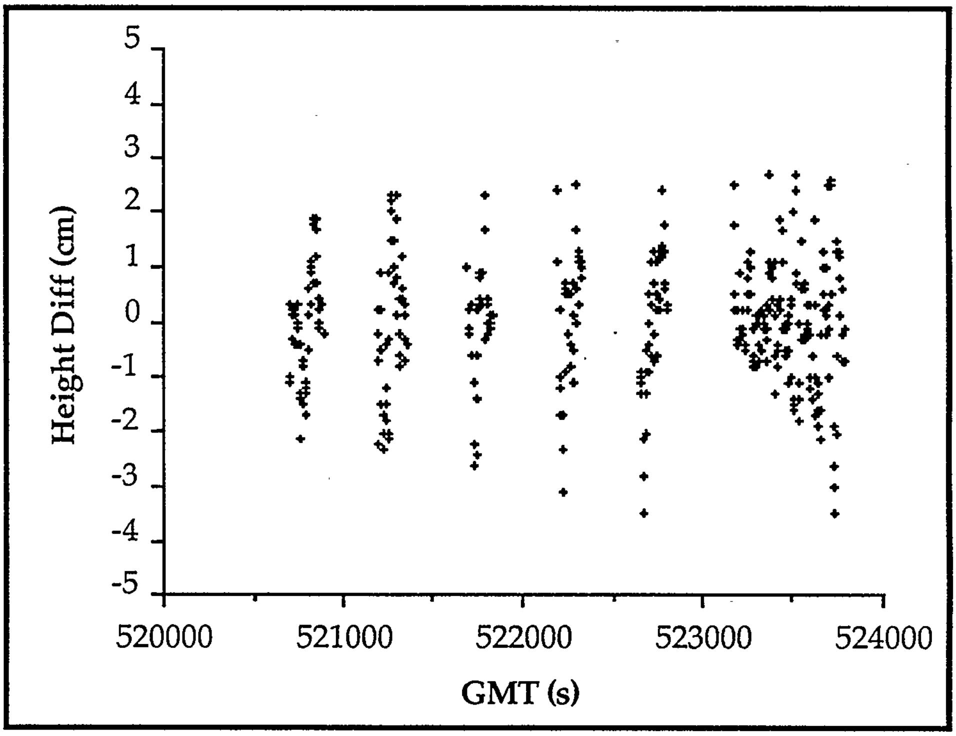

Figure 4.4
Comparison of GPS and GPS/INS Heights

Along with improved interpolation, the INS can significantly benefit the cycle slip detection and correction process. The degree of accuracy and reliability of this process can be characterized by the agreement of the measured double differenced phase observable with the computed observable using the predicted INS coordinates and calculated satellite coordinates (i.e. innovations sequence). Any significant difference (e.g. > 0.75 cycle) between the two observables would indicate cycle slips (see Section 3.4.1).

Listed in Table 4.4 are the statistics between the measured and computed double differences for each of the four 'non-base' satellites. The RMS differences are below 0.2 cycles (< 4 cm) for each satellite, and the mean values are close to zero (< 4 mm). The small RMS differences illustrate the level of cycle slip detection, one cycle in this case, and the small mean values reconfirms the compatibility between GPS and INS. The maximum differences between the two observables range from -0.53 cycles (-10.1 cm) for satellite 9, to -0.86 cycles (-16.4 cm) for satellite 11, with the satellite geometry affecting each satellite differently. These maximum differences may be due to small deviations in the computed time-tags between the GPS receiver and the INS, or it may also be due to filter overshooting. Multipath or an increased carrier tracking bandwidth may be a contributing factor. A higher GPS data rate, say 1 Hz, should improve these results since the time-dependent INS errors would be better controlled. Receivers of this type are currently available from many GPS manufacturers.

Table 4.4
Comparison of Observed Double Differenced Carrier Phase Observation with Computed Observation using Predicted INS Coordinates

Satellite	Mean (cyc)	RMS (cyc)	Max (cyc)
6	-0.01	0.15	0.72
9	0.00	0.10	-0.53
11	0.02	0.19	-0.86
12	-0.01	0.16	-0.84

4.4 Cycle Slip Detection and Correction

In order to investigate the effectiveness of GPS/INS integration for cycle slip detection and correction, cycle slips can be simulated in the otherwise cycle slip-free land vehicle data, and the recovery of these known slips can be monitored. Hence, cycle slips of 1000 cycles were simulated in the data collected at the remote receiver during each of the six 'kinematic' segments of the traverse. The data were then processed using the GPS-only **SEMIKIN** software and the **GPSINS** package to demonstrate the effectiveness of the INS integration.

Table 4.5
Cycles Detected in Cycle Slip Simulation Test for GPS-only and GPS/INS (1000 cycles simulated at each epoch)

		Detected Cycle Slips	
Satellite	GMT (sec)	GPS-only (cyc)	GPS/INS (cyc)
6	520804	1000.065	999.810
9	521252	1000.001	999.984
11	521752	999.994	1000.003
12	522268	1000.137	999.955
6	522744	1000.018	1000.122
9	523436	1000.027	999.992

As a first test, cycle slips were only simulated on one satellite at any one epoch, thus leaving four satellites unaffected. Summarized in Table 4.5 are the number of cycles recovered at each simulated cycle slip epoch for both the

GPS-only and GPS/INS cases. It shows that once the cycles given in Table 4.5 are rounded to the nearest integer number, the correct number of cycles is recovered at all epochs with or without the addition of the INS. The **SEMIKIN** methodology is such that the estimated position from the four 'good' satellites can be used to accurately detect the number of cycles slipped on the fifth satellite (Cannon,1990). In this case, the INS does not assist the cycle slip detection/correction process since the estimated positions using these data are identical with those reported in Table 4.3. The detection ability is within one cycle as shown in Table 4.4.

Table 4.6
Cycles Detected in Cycle Slip Simulation Test for GPS/INS
(1000 cycles simulated at each epoch)

	Detected Cycle Slips			
GMT (sec)	Satellite 6	Satellite 9	Satellite 11	Satellite 12
520804	999.810	1000.031	999.874	1000.205
521252	999.673	999.984	999.804	1000.169
521752	1000.126	1000.006	1000.003	999.913
522268	1000.028	999.984	999.893	999.955
522744	1000.122	999.958	999.764	999.667
523436	1000.171	999.992	999.964	999.897

The next case which was tested was the loss of lock on all satellites tracked, i.e. slips of 1000 cycles were simulated on all satellites at each of the six epochs. In this case, **SEMIKIN** cannot instantaneously correct the number of cycles, since all satellites are affected. Instead, the algorithm will estimate the new ambiguities in the Kalman filter, however, a degradation in positioning accuracy can be expected in this case. With the integration of GPS and INS, the number of satellites with cycle slips at any one epoch is not critical, since the two positioning systems are complementary. Table 4.6 summarizes the cycle slips detected for the GPS/INS case. When the detected cycle slips are set to the closest integer, to represent the theoretical nature of a cycle slip, the correct cycle slips are recovered in each case. Therefore, the estimated positions from the Kalman filter will be identical to those estimated without the presence of cycle slips. This clearly emphasizes the benefit of an auxiliary positioning system to aid the GPS receiver during periods of severe satellite shading, e.g. under tunnels or in urban areas. As previously discussed in Chapter 3, methods for instantaneous ambiguity determination using GPS-only data are currently being investigated, but require the use of P-code technology in a multipath-free, low ionospheric activity environment in order to be effective (Abidin,1990).

Table 4.7
Accuracy of GPS-Only Kinematic Positioning with Multiple Cycle Slips
(Sample size = 386)

Coordinate	Mean (m)	RMS (m)
ϕ	0.00	0.25
λ	-1.43	1.78
h	0.88	1.44

Although the correct cycle slips cannot easily be estimated with GPS-only data when multiple cycle slips occur, the Kalman filter implemented in **SEMIKIN** (Cannon, 1990) will continue to estimate position. A discontinuity in the positioning results will occur after multiple cycle slips, but will be reduced as the estimated ambiguities move toward convergence. Table 4.7 lists the differences between the GPS-only results with and without cycle slips simulated on all satellites at each of the six epochs. This table quantifies the degree of degradation that may be expected when no auxiliary INS is used to aid the GPS with single epoch cycle slip detection and correction. The RMS of the differences are 0.25, 1.78 m and 1.44 m for latitude, longitude and height, respectively. Mean values of the differences are also large for the longitude and height components, indicating a systematic effect in the results due to incorrect estimation of the number of cycles slipped. Longitude and height are more sensitive to cycle slips then latitude due to the specific satellite geometry during the data collection, i.e. there is a weaker correlation between the ambiguities and the latitude component.

4.5 Effect of GPS Update Rate and Outages

The land GPS data were collected once every four seconds and thus the results reported in Table 4.4 are for four second GPS measurement updates to the Kalman filter. In this particular data set, no GPS outages occurred so consistent GPS updates could be made. However, there may be cases during periods of satellite shading where no GPS data are recorded for several seconds, e.g. in forested or urban areas (McLellan et al.,1990). With the integration of GPS and INS, predicted positions are still available from the

INS but with a decreased accuracy over time. The ability of the INS to navigate during these outage periods is a function of the characteristics of the INS. For example, an INS with a high gyro drift rate will show larger position error over time than one with a lower drift rate.

An investigation into the use of the LTN 90-100 for bridging satellite outages was made using the land data and various GPS update rates. By decreasing the GPS measurement interval from 4 seconds to 8, 16, and 32 seconds, a measure of the INS time-dependent errors can be realized. Therefore, the land data were re-processed using for each of these data rates. Various spectral densities of the misalignment states were tested to determine the optimum combination of data rate versus spectral density. However, no significant improvement in the results was gained by changing the spectral densities. Therefore, the initial value of 1 $arcsec^2\ s^{-1}$ (Table 4.2) was selected for all data rates as providing the best agreement between the GPS and INS data.

Table 4.8 summarizes the mean and RMS statistics for the differences between the computed and observed double difference observations (as per Table 4.4) for each of the four 'non-base' satellites. This table shows the decreasing compatibility of the GPS and INS, hence a drop in the effectiveness of cycle slip detection and correction. For example, results of satellite 6 show that at an 8 second update rate, the RMS of the differences is 0.31 cycles, indicating that a cycle slip of 1 cycle would be detectable. When a 32 second update rate is used, the RMS increases to 2.56 cycles, meaning that the smallest cycle slip that can be detected is about three cycles. Obviously, with a decrease in the detection capability comes an uncertainty in the correction procedure as well.

Table 4.8
Comparison of Observed and Computed Double Differenced Phase for Various GPS Update Rates

		Satellite 6		Satellite 9		Satellite 11		Satellite 12	
Update Rate (s)	Sample Size	Mean (cycle)	RMS (cycle)	Mean (cycle)	RMS (cycle)	Mean (cycle)	RMS (cycle)	Mean (cycle)	RMS (cycle)
8	180	0.01	0.31	-0.02	0.21	0.05	0.43	0.02	0.35
16	92	-0.01	0.70	-0.07	0.54	0.00	1.07	0.00	0.92
32	47	0.04	2.56	-0.05	1.38	0.15	2.65	0.19	2.14

Figure 4.5 illustrates the RMS statistics as a function of the update rate for each of the satellites. It includes the four second update rate data given in Table 4.4 and shows that the degradation in the INS is not linear with time, but instead has second-order effects. Further investigations are needed to determine whether, e.g. the inclusion of accelerometer scale factors, will eliminate this non-linearity. Simulation results indicate that the curves given in Figure 4.5 are too steep.

Update rates lower than about 12-14 seconds do not meet the 1 cycle slip detection criterion. Since the land vehicle was travelling at approximately 65 km h^{-1}, the distance travelled in 12-14 seconds is 215-250 m, which exceeds the length of many tunnels and underpasses that may be encountered during normal GPS operation. This figure emphasizes the need for regular, consistent GPS updates to the INS to maintain cm-level accuracies. This may require the modification of operational procedures when collecting data as in the airborne case discussed in Chapter 5.

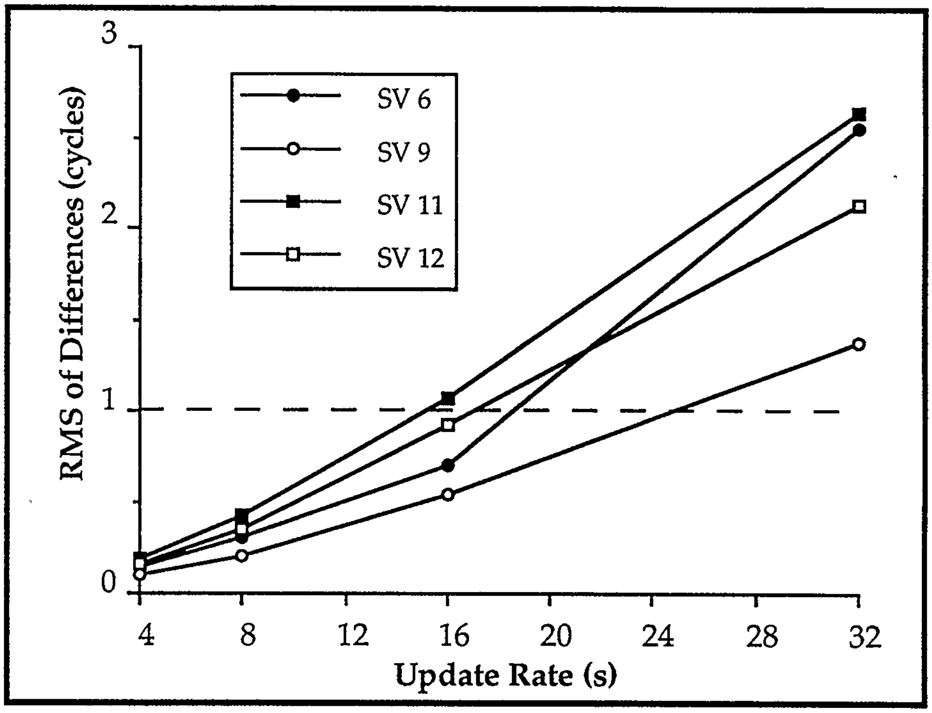

Figure 4.5
Cycle Slip Detection/Correction Capability with Lower GPS Update Rates

The reliability of the estimated results will decrease with a lower GPS update rate or data outages. For example, if no GPS data are recorded for 16 seconds, and the difference between the measured and computed phase double difference is 0.92 cycles (as in the case of Satellite 12 in Table 4.8), the dilemma is whether a cycle slip occurred or whether the INS predicted position has degraded by that amount over the 16 second interval. This emphasizes the proper identification of the time-dependent INS errors used in GPS/INS integration.

The error curves shown in Figure 4.5 show a larger accuracy degradation over time than the simulated errors given in Table 2.5. This is most likely due to unmodelled INS errors. One such effect is a possible colored noise component in the mechanical dither which was not considered in the simulation.

4.6 Errors in Carrier Phase Ambiguity Resolution

For static applications, the double differenced carrier phase ambiguities are estimated using a data set collected in an observation span of 1-2 hours. In this case, the ambiguities can be estimated fairly accurately, usually to the true integer value for shorter baselines. However, for high accuracy kinematic applications, this may not be possible since static data are usually collected for only 10 - 20 minutes prior to the remote receiver being moved. In this case, unless the baseline is very short (e.g. a few km), the correct ambiguities may not be recovered. Accurate knowledge of the remote receiver's relative position with respect to the monitor receiver will assist in the determination of these ambiguities, but still may not be sufficient for ambiguity recovery for longer separations.

In order to assess the effect an incorrect estimation of the initial carrier phase ambiguity has on kinematic positioning, a test was performed using the land data. The true integer ambiguities were correctly estimated during the initial static survey and held fixed during the kinematic segment of the survey (so only the remote receiver's position was estimated). To simulate the case where the incorrect ambiguities are recovered, cycles were consecutively added to the correct carrier phase ambiguity for one of the satellites, and the kinematic data re-processed.

Figures 4.6 and 4.7 show the error in latitude and height, respectively, when one, two and three cycle errors are simulated in the initial ambiguity for one of the double difference pairs. These errors are the difference between the kinematic solution with and without ambiguity errors. Although different error curves will result for different satellites, the drift trends will remain. By comparing the two figures, it is easily seen that the effect of the simulated ambiguity errors is much greater for height than latitude. This is due to the correlation between the ambiguity parameter and these two components; the correlation between the ambiguity and latitude is -0.08 while it is -0.22 for height.

Figures 4.6 and 4.7 show a drift in the error over the observation span of approximately one hour. This is important since it may otherwise be assumed that an incorrect initial ambiguity determination would only cause a bias in the estimated results. However, due to the changing satellite geometry, the influence of the ambiguity error will not remain constant for the duration of the run. For the case that a one cycle error is applied to the initial carrier phase ambiguity, the latitude drift is about 6 cm, while it is 14 cm in height. The drift for a two cycle error is 12 cm in latitude and 28 cm in height, twice the one cycle error. This relationship also holds for the three cycle case, i.e. three times the one cycle error. Similar relationships occur when different base satellites are chosen, although the magnitude of errors is different for each configuration.

This phenomenon of a drifting GPS solution due to incorrect resolution of the initial carrier phase ambiguities is important for high-accuracy kinematic positioning. Numerous investigations into these types of applications have detected drifts in the GPS solutions, e.g. van der Vegt et al. (1988), Friess (1988), Dorrer and Schwiertz (1990). Drift components ranging from 0.25 mm s^{-1} to 6 mm s^{-1} have been identified when kinematic GPS positions have been compared to accurate independent control. These drifts have most likely been the result of incorrect initial ambiguity resolution.

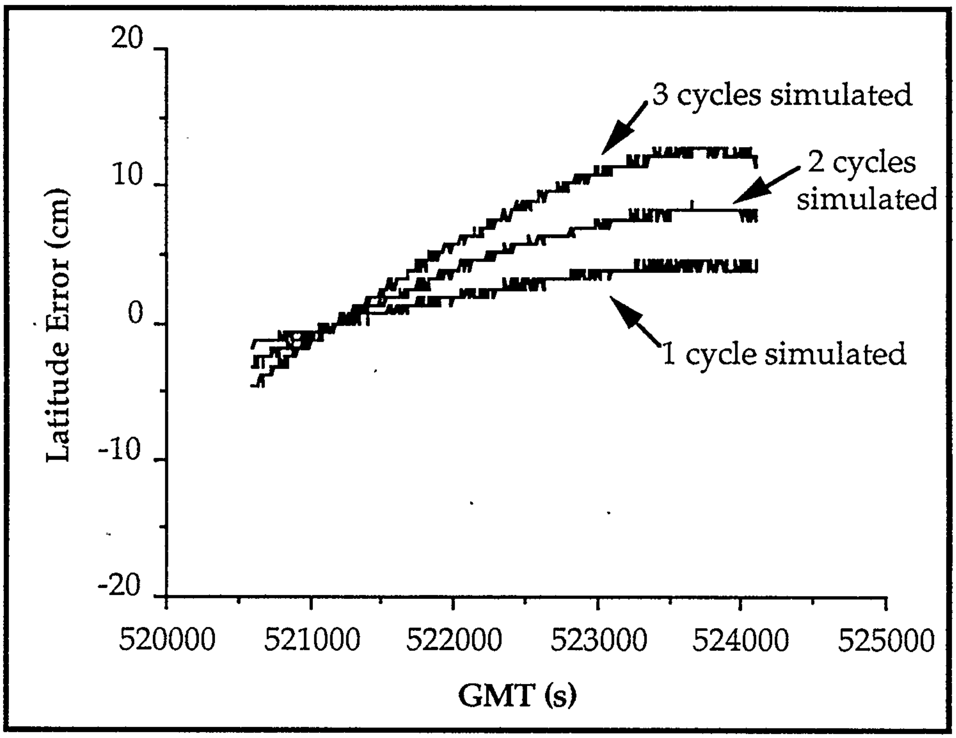

Figure 4.6
Effect of Incorrect Ambiguity Resolution on Latitude

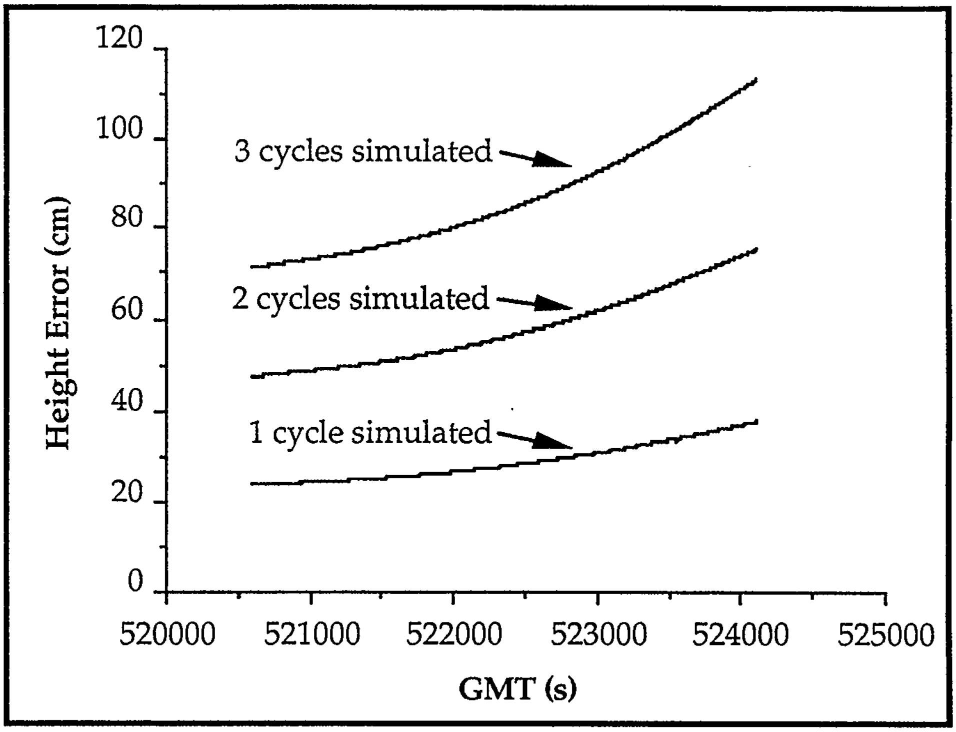

Figure 4.7
Effect of Incorrect Ambiguity Resolution on Height

In order to effectively resolve the initial ambiguities properly, various operational procedures may be implemented. The most straightforward one is to ensure that the monitor GPS receiver is located near, say within a few km, to the remote receiver at initialization. This, however, may not be feasible for some applications. In aerotriangulation, for example, the remote antenna is mounted on the aircraft which is located at the airport. The photogrammetric test area may be far away (tens of km) and if the monitor receiver is located in the photogrammetric test area to maintain short GPS baselines during the actual photography, a short initial baseline cannot be achieved. In this case, a modified operational procedure of multiple monitor receivers would be beneficial. One monitor receiver would still be situated in the photogrammetric test area, and an additional receiver would be placed in the airport vicinity. Therefore, the airport monitor could ensure a short initial baseline with the remote receiver so proper initial ambiguity resolution could occur, and the test area monitor would ensure short baselines during the crucial photogrammetric stage.

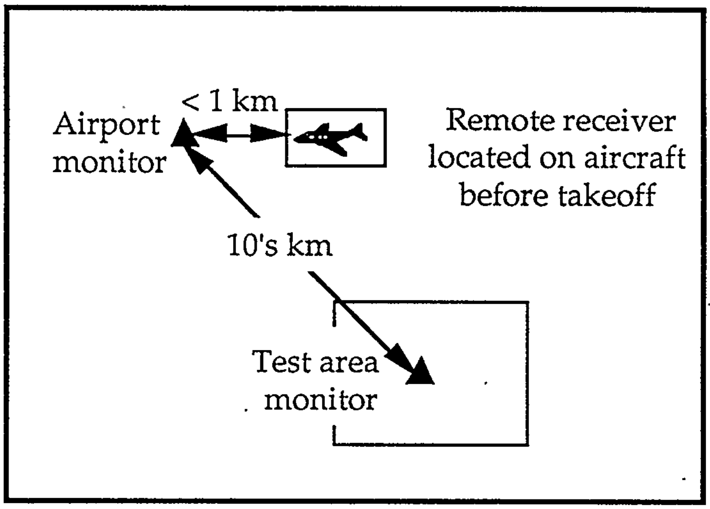

Figure 4.8
Multiple Monitor Station Concept for Initial Ambiguity Resolution

Since the two monitors would have simultaneous static data over the entire observation span, generally 1-2 hours, ambiguities would be accurately resolved between these two monitor stations. Using the estimated ambiguities between the monitor receivers and the estimated ambiguities between the airport monitor and remote receivers, accurate initial ambiguities could also be computed between the test area monitor receiver and remote receiver at initialization. This multiple monitor concept is illustrated in Figure 4.8. Using this technique, not only will the position drifts be removed, the reliability of the survey is also increased dramatically. A discussion on further operational improvements for GPS-aerotriangulation surveys can be found in Merrell et al. (1990).

CHAPTER 5

RESULTS - AIRBORNE CASE

The application of GPS/INS positioning for the airborne case was realized through a combined GPS/INS - Aerotriangulation campaign. An adjustment of the photogrammetric data gave accurate perspective centre (PC) control for the camera at the time of exposure and could subsequently be used to assess the capability of GPS/INS in an aircraft environment. This chapter describes the test and gives results pertaining to the achievable accuracy of GPS/INS for the airborne case.

5.1 Test Description

Airborne tests were carried out in August-September, 1988, near Cologne, Germany, by the University of the Federal Armed Forces, Munich, The University of Calgary and the Rheinbraun Company, Cologne. The purpose of the tests were to assess the feasibility of GPS, or alternatively GPS/INS, for replacing conventional ground control in a photogrammetric adjustment.

The flight area covered an open pit mine in which photogrammetric monitoring missions of the terrain slope movements were conducted on a regular basis. Numerous accurate ground control points had been established in the region so it was well-suited for a comprehensive test of aerotriangulation without ground control.

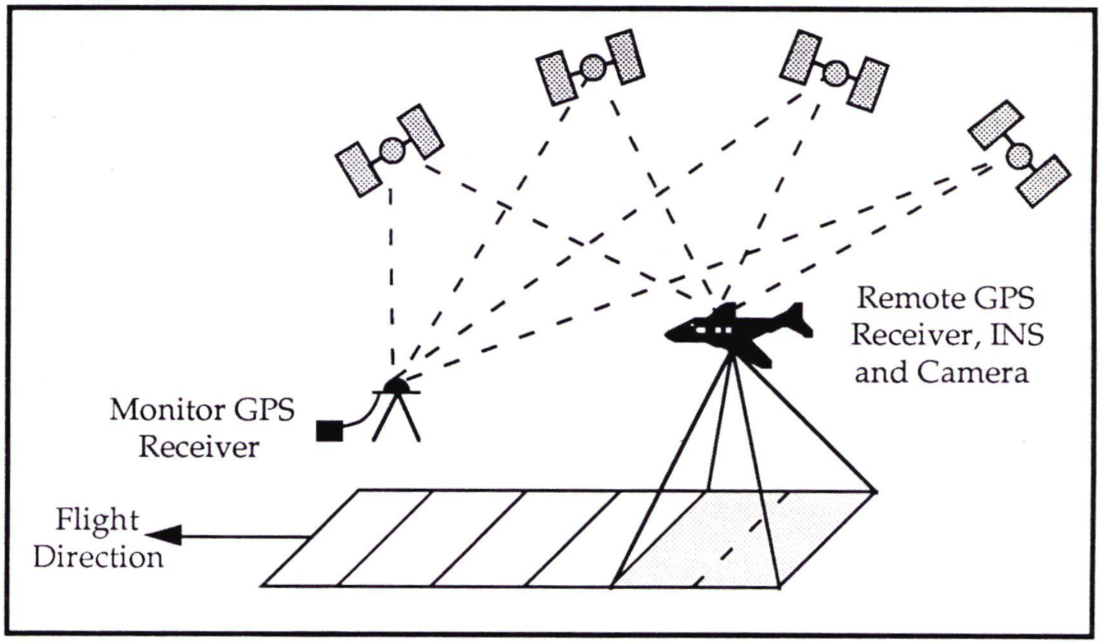

Figure 5.1
GPS/INS - Aerotriangulation Concept

Three days of tests were performed, two with Texas Instruments TI4100 receivers and one with Trimble 4000SX receivers. Since satellite shading was a severe problem with the data collected with the TI4100 equipment, only the August 31 Trimble data were used for integration with the INS. The main hardware components used for the test in addition to the two GPS receivers, were The University of Calgary's Litton LTN 90-100 strapdown inertial system and an RMK 15a/23 photogrammetric camera which were installed in the

Cessna aircraft. Portable computers were also used for data collection and time-tagging purposes. Figure 5.1 illustrates the differential GPS-INS concept as well as the photogrammetric procedure.

The monitor GPS receiver was located near the test area while the remote unit was located in a Cessna aircraft with the INS and the camera. The GPS antenna was mounted on the upper part of the fuselage of the aircraft. Offsets between the GPS antenna, the INS and the camera were accurately measured by conventional techniques before the test so they could be used in the GPS/INS integration and also for the comparison of the GPS antenna coordinates with the camera.

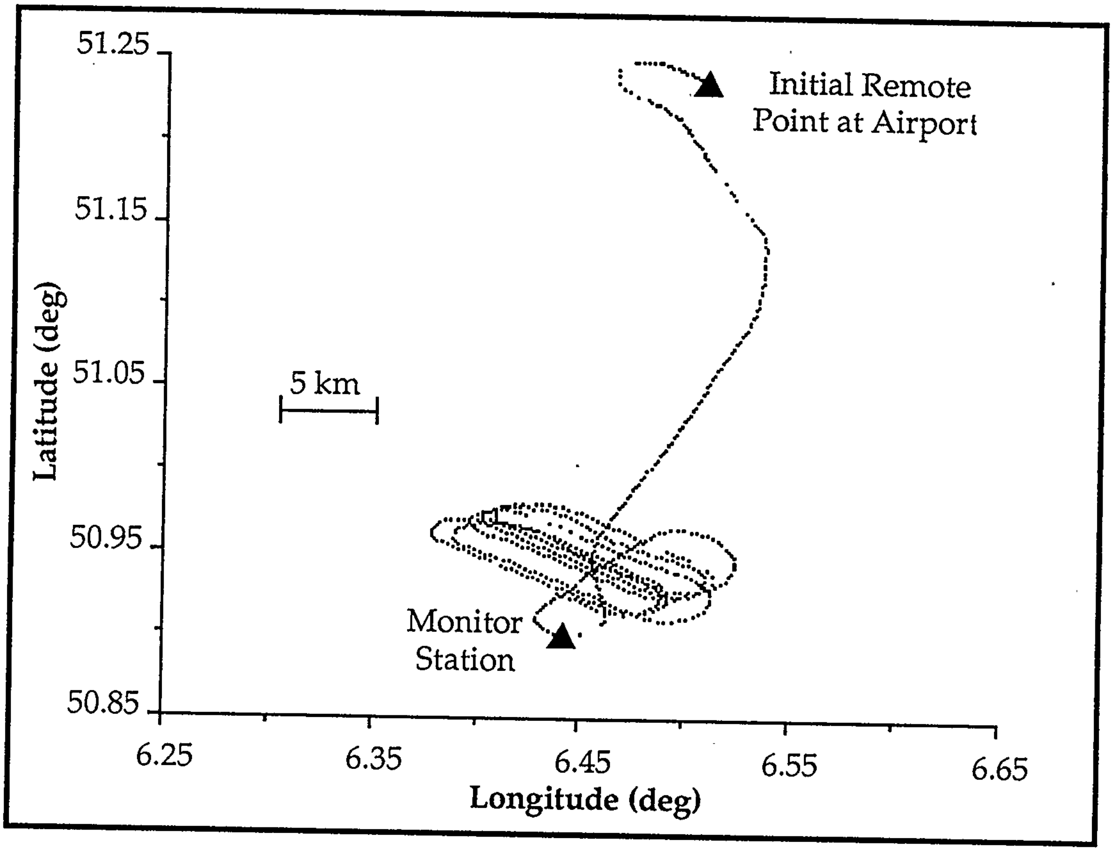

Figure 5.2
GPS/INS Flight Trajectory

At the start of the run, an adequate amount of static data could not be collected at the remote receiver due to hardware problems. However, at the end of the run, after the aircraft had landed at the airport, a 20 minute differential static survey was performed between the monitor station and the remote receiver. Therefore, the data were processed in a reverse time sequence to allow for an adequate static survey to recover the initial carrier phase ambiguities. Figure 5.2 shows the reverse aircraft trajectory, i.e. from the end of the run to the start of the photography. The flying height was approximately 700 m above the ground and aircraft speeds reached 250 km h^{-1} (70 m s^{-1}). The airport is located at the north end of Figure 5.2. As the diagram shows, the initial separation between the monitor and remote receivers was approximately 30 km in length. Ideally, this separation should be smaller, less than 20 km to ensure that the integer ambiguities can be recovered. About 72 minutes of data were collected including the 20 minutes of static data. A special operational consideration of performing wide turns instead of severe banked turns were made during data collection to reduce the possibility of satellite masking. The maximum aircraft roll angle was ten degrees.

GPS data were collected at a 0.25 Hz (once every four seconds) on five Block I satellites (6,9,11,12,13) throughout the run. SA was not on during this experiment. Figure 5.3 shows a GDOP of below five during the campaign. INS data were logged at a 64 Hz rate. Data were time-tagged through the 1 PPS output of the GPS receiver and also through time marks that were interrogated from the GPS receiver. Time-tagging with the camera was accomplished through an Hewlett-Packard portable computer.

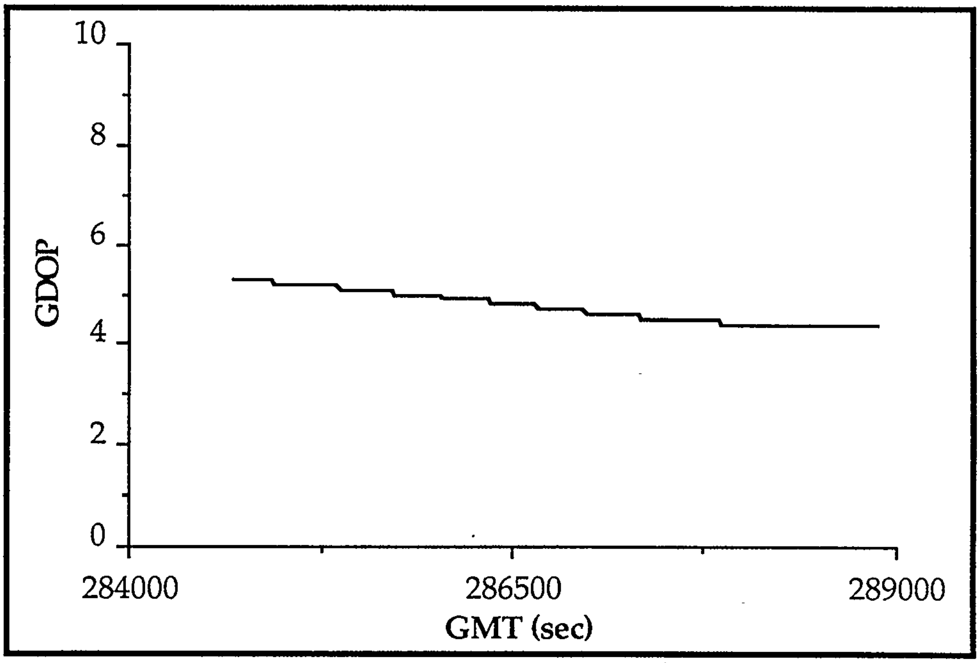

Figure 5.3
Airborne Test Geometric Dilution of Precision

A bundle block adjustment of the photogrammetric data was performed by the Munich Bundeswehr University using the photo coordinates measured by Rheinbraun. All the available ground control were used in this case, i.e. no information from the GPS/INS system was used in the bundle adjustment. PC coordinates of the camera at the exposure times were estimated and then translated to the GPS antenna using the measured offsets. Camera orientation parameters at the exposure times were also output from the adjustment. The RMS accuracy of the estimated PCs were about 5 cm in position and several arcseconds in orientation. This control could then be used to assess the accuracy of the estimated GPS/INS position and attitude.

5.2 Airborne GPS/INS Processing

The GPS and INS data were processed using the **GPSINS** program which was also used to process the land kinematic data. Time-tagging problems between the GPS and INS data were evident mainly due to the poor timing information interrogated from the GPS receiver. The GPS time-tag was only accurate to ±20 ms which at the aircraft speed, is 1.4 m, however, this error is random in nature. Trial and error was used to find the best fit of the GPS and INS time scales, however, small discrepancies between the two time frames remained in the data, most likely at the 5 ms level, i.e. about 35 cm.

Input parameters to the Kalman filter are summarized in Table 5.1. Note that they are very similar to the land case (see Table 4.1), except for the spectral densities of the misalignment states. In the case of the airborne data, they are significantly larger, i.e. 100 $arcsec^2\ s^{-1}$ versus 1 $arcsec^2\ s^{-1}$ for the land case. The spectral densities were chosen to give a 'best fit' of the INS and GPS data. In the case of the land data, very small spectral densities of the misalignments could be used since there were no time-tagging problems between the two data sets. As previously discussed in Chapter 4, the results of the land test were not very sensitive to the magnitude of the misalignment spectral densities. However, in the case of airborne data, large discrepancies between the GPS and INS data were detected when small spectral densities were utilized. This is most likely due to unsystematic time-tagging errors between the two measuring systems, but may also be due to the noise characteristics of the INS in an aircraft environment. This is discussed further in Section 5.5.

Table 5.1
GPS/INS Kalman Filter Input Parameters for Airborne Data

Parameter	Initial Standard Deviation	Spectral Density	Correlation Length
Position	0.1 m	0	-
Velocity	0.001 m s^{-1}	$2.5*10^{-7}$ m^2 s^{-3}	-
Misalignments	40 arcsec (roll,pitch) 3600 arcsec (azimuth)	100 $arcsec^2$ s^{-1}	-
Gyro Drifts	0.01 deg h^{-1}	$1.39*10^{-9}$ deg^2 h^{-3}	144000 s
Accel. Biases	0.0001 m s^{-2}	$1.39*10^{-12}$ m^2 s^{-5}	144000 s

At the initial baseline, the relative coordinates of the remote antenna with respect to the monitor were not known, so the remote receiver's position was estimated along with the initial carrier phase ambiguities using the 20 minutes of static data. Since the initial baseline was approximately 30 km in this test compared to a few km in the land case, the initial GPS phase ambiguities were not set to their integer values, but instead were fixed at the estimated 'real' numbers.

5.3 Cycle Slip Detection and Correction

In order to assess the compatibility of the INS and GPS data and also the cycle slip detection and correction capabilities of the methodology, the misclosures of the computed and measured double differences were statistically analyzed. Figure 5.4 shows the differences between the measured and computed double differences for satellite 13 (using satellite 12 as the base satellite) at each kinematic epoch. Also plotted on this figure is the aircraft speed. Note that the data were processed in a reverse sequence. The misclosures are very small for the first 250 kinematic epochs or 1000 seconds. However, once the aircraft begins a turn (illustrated by the sudden changes in aircraft velocity) the misclosures become larger and exceed one cycle in some cases. This is likely due to time-tagging problems between GPS and INS or to filter overshooting. The mean and RMS of the differences of the misclosures is 0.03 and 0.30 cycles, respectively, for satellite 13.

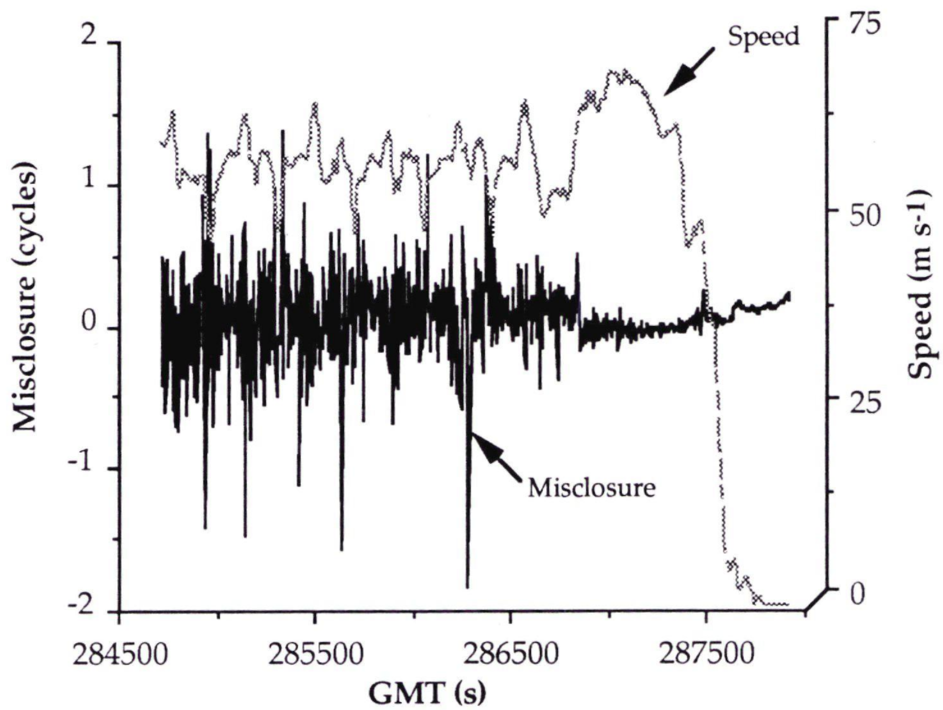

Figure 5.4
Comparison of Misclosures with Aircraft Dynamics for Satellite 13

Table 5.2 summarizes the agreement between the INS and the other satellites tracked. The RMS of the differences reach 0.94 cycles for satellite 3. The differences between the statistics of the various satellites are due to satellite geometry. It clearly shows that the cycle slip detection and correction capability using this particular data set is not at the one cycle level, as in the land case, but is more likely at the 1-2 cycle level (approximately 0.2-0.4 m). However, Table 5.2 also shows that the mean difference between the observed and predicted double differences for all satellites is close to zero. This indicates that there are no large unmodelled effects between the two systems and that RMS differences are mainly due to random errors.

Table 5.2
Comparison of Observed Double Differenced Phase Observation with Computed Observation using Predicted INS Coordinates

Satellite	Sample Size	Mean (cycles)	RMS (cycles)
3	760	-0.04	0.94
9	749	-0.02	0.45
11	760	0.03	0.53
13	760	0.03	0.30

Four cycle slips were detected on satellite 9 in the remote GPS data during the mission. Table 5.3 gives the number of cycle slips detected as well as the aircraft speed at the time of the slip. Although the exact number of cycles slipped is not known, the fact that the number of cycles are close to integer numbers (except for the last case) may indicate that the correct number of cycles was recovered. The results of Figure 5.4 and Table 5.3 indicate that good agreement between GPS and INS results in an effective cycle slip recovery for lower aircraft velocities.

Table 5.3
Cycle Slips Detected in Airborne GPS Data

Satellite	GMT (sec)	Cycle Slips Detected	Aircraft Speed (m s^{-1})	Aircraft Accel (m s^{-2})
9	287868	382504.986	0.05	-0.01
9	287756	367250.102	0.18	0.14
9	287648	121624.879	2.23	0.07
9	287600	9580514.546	4.41	0.00

5.4 Positioning Results

Coordinates of the GPS antenna and the attitude of the INS were required at the camera exposure times to compare with the photogrammetrically-derived exterior orientation. Since these times did not coincide with either a GPS or INS measurement, the high rate INS measurements were used to interpolate between two successive measurement epochs as shown in Figure 5.5. These data were then used in the Kalman filter to predict the aircraft position and attitude at the exact camera exposure time. Since the INS data rate is 64 Hz, this interpolation will not introduce significant error into the results.

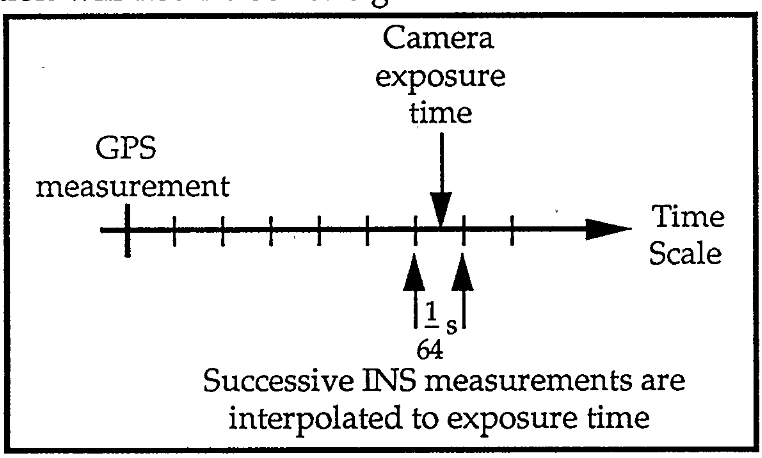

Figure 5.5
Interpolation of INS Measurements to Camera Exposure Time

PC control for seven strips of photography, for a total of 34 control points, were available for comparison with the GPS/INS-derived positions. The PCs were translated to the GPS antenna so direct comparisons could be made between the two sets of positions. Attitude information resulting from the bundle adjustment was used in the translation, however, the INS attitude components could be also used as will be discussed in Section 5.5. PC positions resulting from the bundle block adjustment were reported in the local datum. Since GPS is referenced to WGS-84, a transformation had to be performed before GPS/INS positions could be compared with the photogrammetric results. Unfortunately, no ties were made between the two coordinate systems. Therefore, PC coordinates from the block of photography were selected along the corresponding GPS/INS positions, and a three parameter translation between them was estimated. Once the GPS/INS positions were transformed to the local datum they were converted to mapping plane coordinates (Gauss-Krüger System).

As a first analysis, GPS data were processed using the **SEMIKIN** program (Cannon, 1990). Since only isolated cycle slips occurred in the data (see Table 5.3), GPS-only results can be expected to be satisfactory. Table 5.4 summarizes the RMS and maximum statistics when comparisons are made between the GPS results and photogrammetrically-derived GPS antenna coordinates. RMS differences between the two are 25.0, 26.5 and 18.7 cm for the east, north and height components, respectively, for a 3-D RMS of 23.6 cm. Although these results are good, the maximum difference reaches -84.5 cm for the north coordinate. Some of this error is due to interpolation of the GPS positions to the time of camera exposure. Since the GPS data were only recorded every 4 seconds and the aircraft speed reached 70 m s^{-1}, interpolation errors can conceivably reach several decimetres.

Table 5.4
Comparison of GPS with Photogrammetrically-derived Coordinates

Coordinate	RMS (cm)	Max (cm)	3-D RMS (cm)
East	25.0	76.5	23.6
North	26.5	-84.5	
Height	18.7	60.2	

The data were re-processed using **GPSINS** and Table 5.5 shows the agreement between the GPS/INS positions and the photogrammetrically antenna positions. In this case, RMS accuracies are 16.0, 13.5 and 17.0 cm for the east, north and height components, respectively, for a total RMS of 15.6 cm. This is a significant improvement over the GPS-only results, mostly due to the improved interpolation capability with the addition of the INS. This is clearly evidenced by the maximum differences, e.g. the north maximum difference is reduced from -84.5 cm to -30.0 cm.

Table 5.5
Comparison of GPS/INS with Photogrammetrically-derived Coordinates Using a Block 3 Parameter Transformation

Coordinate	RMS (cm)	Max (cm)	3-D RMS (cm)
East	16.0	-52.4	15.6
North	13.5	-30.4	
Height	17.0	42.7	

Figure 5.6 shows a plot of differences between the GPS/INS and photogrammetric positions for the 34 points. For each of the three dimensions, the discrepancies are generally a few decimetres. A few outliers exist in the east component and a drift is evident in both east and height, although the height drift is more significant. The outliers are most likely due to unresolved time-tagging errors between the GPS and INS systems, whereas the 50 cm height drift is most likely a result of time-dependent systematic effects in the GPS position estimation.

Position drifts have been detected in similar investigations, e.g. van der Vegt et al. (1988), Friess (1988), Dorrer and Schwiertz (1990). In the case of van der Vegt et al. (1988), a drift of up to 0.45 mm s^{-1} was detected in the height component when differentially corrected GPS heights were compared to bundle adjustment results, whereas in Friess (1988), drifts of the order of 6 mm s^{-1} were observed in all three components, and 3 mm s-1 drifts were detected in the Dorrer and Schwiertz investigation. In the present case, the drift between GPS/INS and photogrammetrically-derived heights is approximately 0.25 mm s^{-1}, in agreement with the van der Vegt investigation. The source of these errors is most likely the result of incorrectly

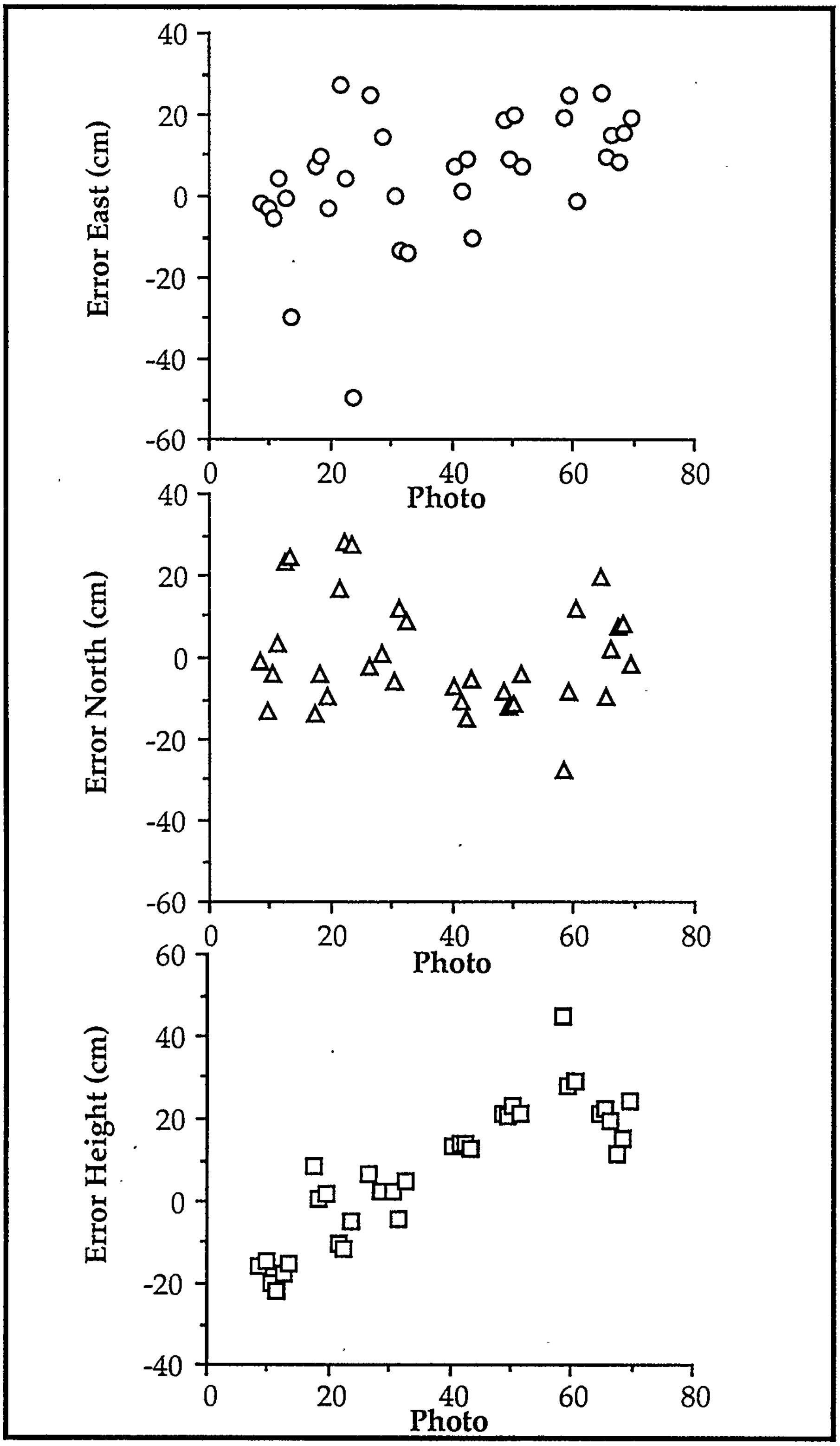

Figure 5.6
GPS/INS Positioning Results

resolved initial carrier phase ambiguities. Since the initial baseline is 30 km and only 20 minutes of static data were collected, it is extremely difficult to estimate the correct ambiguities with C/A code, five channel GPS hardware. As discussed in Section 4.6, errors in the initial ambiguities will cause drifts in the estimated position at a magnitude dependent on the satellite geometry. The results presented in Figure 5.6 generally agree with those given in Section 4.6, i.e. the east (longitude) and height components are more severely affected due to the correlation between the ambiguities and these components.

Dorrer and Schwiertz (1990) analyze a different set of data collected in the same test area but investigate various transformations between the local datum and WGS-84 such as a linear time variant Helmert transformation. This type of transformation would absorb most of the drift since it allows for a time variation in the WGS 84-local datum transformation. In reality, this scenario has no physical basis and in general is not appropriate since the errors are merely modelled in the post-processing stage rather than during position estimation. However, since the correct ambiguities cannot be recovered with the present airborne data due to limitations with the operational procedures and hardware used, a linear time variant Helmert transformation or a three parameter translation of each strip can be used to show the potential of GPS/INS positioning if the initial ambiguities can be correctly recovered. Table 5.6 shows the results when the strip transformation is applied. Compared to Table 5.5, the results are improved, especially in height in which the drift is virtually removed. Note that the maximum values are not significantly reduced in the east coordinate since it is due to time-tagging which is not modelled in the transformation.

Table 5.6
Comparison of GPS/INS with Photogrammetrically-derived Coordinates Using a Strip 3 Parameter Transformation

Coordinate	RMS (cm)	Max (cm)	3-D RMS (cm)
East	13.5	-49.4	10.6
North	11.5	-21.1	
Height	4.6	12.9	

The *a posteriori* standard deviations of the positions as estimated from the covariance matrix are about ± 1-2 cm in all three coordinates during the satellite window. These are clearly optimistic when the true accuracy of the results are considered. Standard deviations of ±1 cm and ±1 cm s^{-1} were assumed for the accuracy of the carrier phase and Doppler frequency, respectively. These values only consider the true noise characteristics of the receiver tracking loops in kinematic mode and assume that all systematic effects have been modelled correctly. Errors such as multipath, residual orbit and atmospheric errors and incorrect ambiguities, that have not been explicitly considered in the magnitude of the measurement noise will cause errors in the estimated positions that will not be represented in the *a posteriori* statistics (Lachapelle et al.,1991).

These results are slightly worse than those reported by Baustert et al. (1988) using TI 4100 receivers in the same test area. Agreement of 4-6 cm between the GPS-only and photogrammetrically-derived coordinates was reported in this case. This is most likely due to time-tagging problems with the Trimble receivers, but also improved results with the P-code TI 4100 receivers, since this gives the addition of the L2 frequency for ionospheric corrections. Since the distance between the monitor and remote receivers ranges from a few km to 30 km during the photography, the ionosphere could contribute several cm (see e.g. Lachapelle and Cannon, 1986).

5.5 Attitude Determination

The ability of the GPS/INS system to provide accurate and reliable attitude information will create many new and novel uses of the system. For photogrammetric applications, accuracies of ten arcseconds or better are required in order to benefit the block adjustment (Schwarz et al.,1984). Although for photogrammetric applications, external attitude information is not necessary in a block adjustment if accurate PC coordinates are available, they are required for single strip photography in order to constrain the roll orientation component. Also, for many digital scanning systems the attitude is critical since single strip data are collected.

In order to appreciate the attitude dynamics of the Cessna aircraft, the attitude of one photogrammetric strip was analyzed. Figures 5.7 and 5.8 show the roll and azimuth of the aircraft for the strip (about 25 seconds of time) generated from GPS/INS results. Note that the roll component has a higher frequency than azimuth.

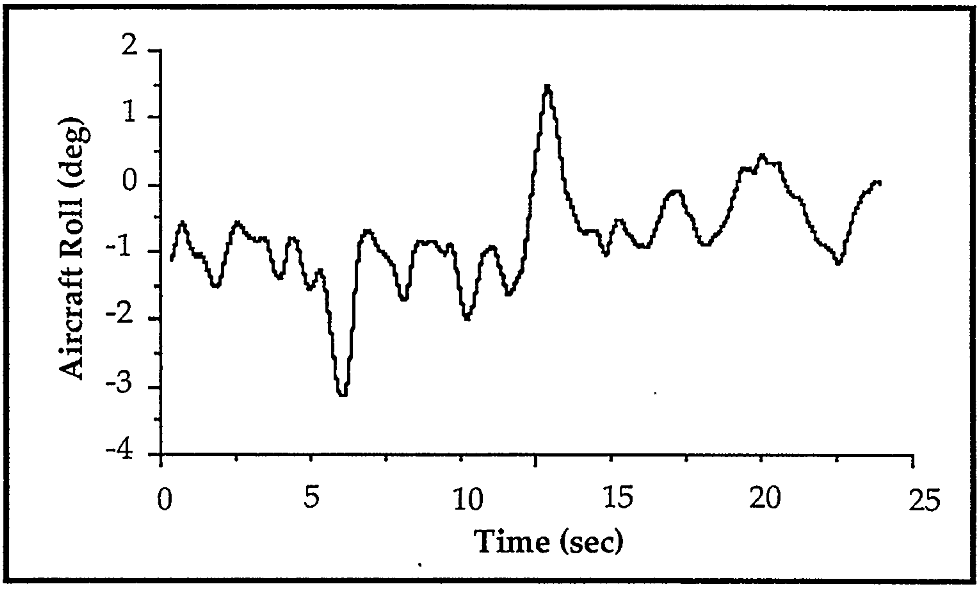

Figure 5.7
Aircraft Roll for One Photogrammetric Strip Generated from GPS/INS

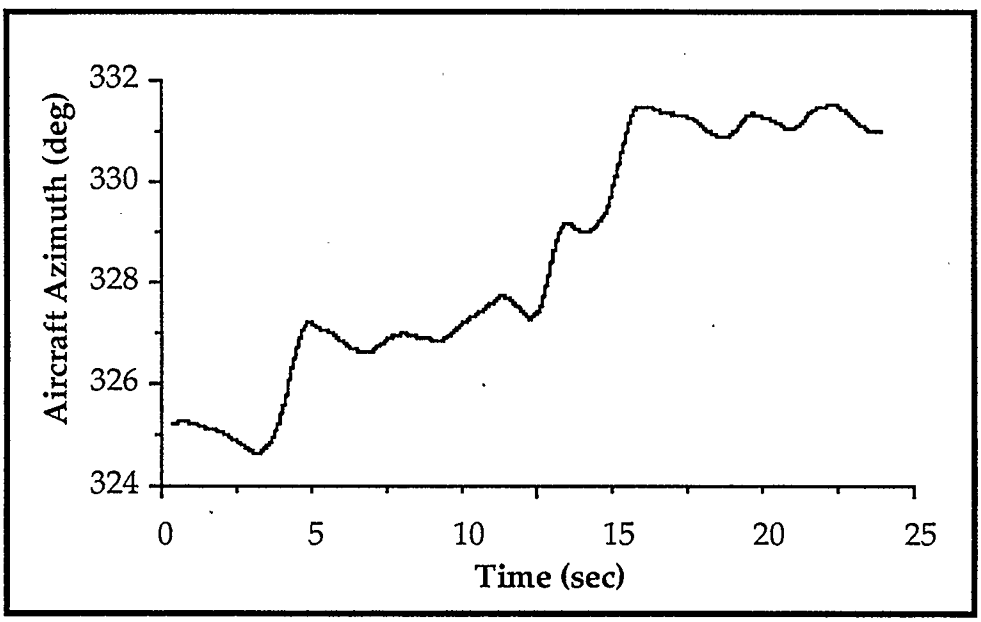

Figure 5.8
Aircraft Azimuth for One Photogrammetric Strip Generated from GPS/INS

The Rheinbraun bundle block adjustment using all available ground control gave the estimated aircraft attitude at each exposure time with an accuracy of several arcseconds. Using this information as control, the feasibility of using GPS/INS-computed orientation could be assessed. Rather than compare the absolute orientation between the two sets of attitude, only the change in attitude from one exposure time to the next was compared. Using this relative approach, any discrepancies between the absolute reference of the camera and INS coordinate frames could be removed. This is justified since only relative attitude information between consecutive photographs is required in a bundle adjustment. Table 5.7 summarizes the ability of the strapdown system to provide attitude data for each of the exposure times. Clearly, the achievable accuracy does not meet the requirements needed as *a priori* information for PC control in a bundle adjustment.

Table 5.7
Comparison of GPS/INS with Photogrammetrically-derived Attitude

Direction	RMS (arcsec)
Roll (y)	1329
Pitch (x)	1593
Azimuth (z)	414

The reasons for the very large discrepancies between the INS and camera attitudes may be attributed to one of the two following scenarios:

1) The discrepancies may be due to the hardware installation during data collection. The camera was mounted on vibration shocks during the flight while the INS was rack-mounted, so relative movements between the INS

and the camera occurred. If these movements are significant, the orientation of the two systems may be incompatible.

2) The noise on the gyros may be too high, hence precise attitude determination using the LTN 90-100 strapdown system may not be feasible.

The first scenario can be illustrated by the fact that the offset between the camera and INS centers was approximately 62 cm and a lateral shift of 1 mm between the two systems from one exposure to the next would cause an orientation discrepancy of over 5 arcmin. Therefore, it is recommended that the INS and camera be mounted together so they experience identical dynamics.

In order to test the hypothesis that the gyros are not suitable for precise attitude determination, the noise of INS gyro measurements was computed using a Fast Fourier Transform (FFT) on the raw gyro data to compute the power spectral density (PSD). Using this technique, the computed noise can be compared to the estimated attitude accuracy listed in Table 5.7 to determine if they are compatible. The PSD of a random process, $x(\tau)$, describes the frequency content of that process and is defined by the Fourier transform of its autocorrelation function, i.e. from (Brown,1983)

$$PSD = F[R_X(\tau)] = \int_{-\infty}^{\infty} R_X(\tau)\, e^{-j\omega\tau}\, d\tau \qquad 5.1$$

where $F[\cdot]$ ... denotes Fourier transform

$R_X(\tau)$ ... is the autocorrelation function of $x(\tau)$

and ω ... is 2π.

Figure 5.9 shows the PSD of the y-gyro for the time period shown in Figures 5.7 and 5.8. Note the discontinuities in the low frequencies due to the vertical scale of the graph. Several distinct spectral ranges can be identified; for frequencies smaller than 4 Hz aircraft dynamics dominate, between 7 and 11 Hz there is some engine vibration, apparently centered around one of the aliased dither frequencies at about 9 Hz. The other aliased dither frequencies are at approximately 22 and 24 Hz. Otherwise, there seems to be mainly system noise above 10 Hz.

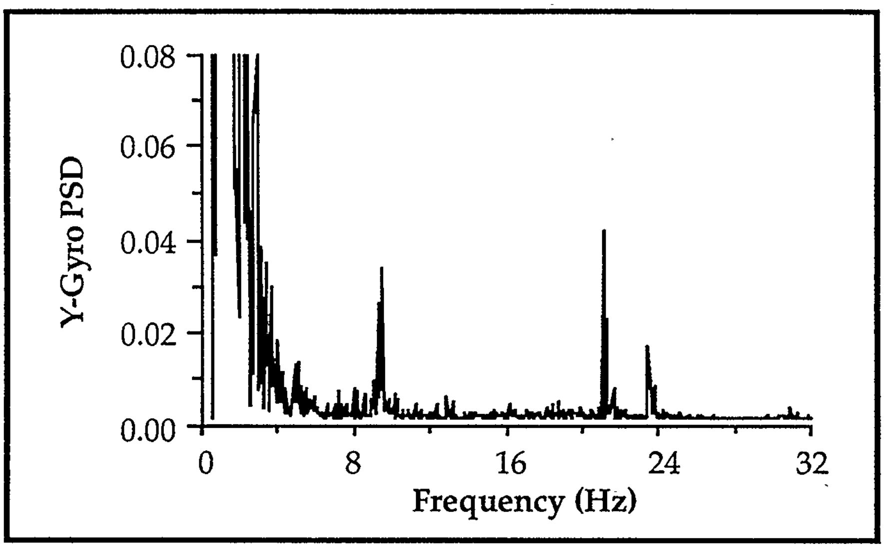

Figure 5.9
FFT of Raw y-Gyro INS Output

By eliminating the mean value and dither frequencies (Czompo,1990) and integrating only the power in the frequencies above the aircraft dynamics, a fairly reliable estimate of the measurement noise can be obtained. Assuming the dynamic threshold to be 4 Hz, the computed 1σ-attitude noise is 765, 926 and 403 arcsec.s^{-1} for the x, y, and z gyros, respectively. These values are very large and well above the requirement for attitude determination at the 10 arcsecond level. However, they are below the estimated accuracies shown in Table 5.7 (except for the azimuth z-gyro), indicating that the large discrepancies given in the table may be due to both unexpectedly high gyro noise and small relative shifts between the camera and INS.

If appropriate smoothing techniques are applied to the frequencies above the dynamics threshold, a dependable estimate of the resolution of the aircraft attitude dynamics through INS can be obtained. Table 5.8 summarizes gyro noise characteristics using various cutoff frequencies and different smoothing intervals. For example, in the case that the dynamic cutoff frequency is 4 Hz (i.e. only noise above 4 Hz), the noise on the y-gyro decreases from 0.2573 deg s^{-1} to 0.0149 deg s^{-1} when 32 y-gyro measurements are averaged. This means that instead of 64 Hz INS data, one would only get 2 Hz data but with much lower noise. Nevertheless, even under this dynamic cutoff frequency assumption and degree of the smoothing, the noise can only be reduced to 54 arcsec s^{-1}, still above the necessary level for a photogrammetric adjustment.

With higher cutoff frequencies, the gyro noise decreases as expected. However, the correct cutoff frequency is dependent on the type of aircraft used in the data collection since the dynamics of different sizes and types of aircraft is vastly different. If the cutoff frequency is set too low, aircraft dynamics are smoothed and a deterioration in positioning accuracy will result. In contrast, if the cutoff frequency is set too high, the effectiveness of the smoothing algorithm will not be fully exploited.

The estimated attitude from GPS/INS is sufficiently accurate to be used to determine the instantaneous translations between the camera and GPS antenna in the camera reference frame. Since the distance between the antenna and the camera was 1.11 m, an error of 0.25 degrees in the attitude would cause a position error of approximately 5 mm, within the error budget of the current achievable accuracy.

Table 5.8
Spectral Analysis of Raw INS Gyro Output Using Various Cutoff Frequencies
(All values are in deg s^{-1})

Cutoff Freq (Hz)	Gyro	Std Dev (all meas)	Std Dev (average of 2 meas)	Std Dev (average of 4 meas)	Std Dev (average of 8 meas)	Std Dev (average of 16 meas)	Std Dev (average of 32 meas)
<2	x	0.2148	0.1587	0.1137	0.0474	0.0210	0.0101
	y	0.3564	0.3157	0.2690	0.2142	0.1164	0.0372
	z	0.1212	0.0843	0.0619	0.0520	0.0260	0.0156
<4	x	0.2125	0.1556	0.1089	0.0380	0.0157	0.0096
	y	0.2573	0.2005	0.1303	0.0581	0.0289	0.0149
	z	0.1121	0.0705	0.0471	0.0231	0.0126	0.0079
<6	x	0.2062	0.1472	0.0978	0.0263	0.0133	0.0087
	y	0.2361	0.1738	0.0978	0.0294	0.0179	0.0107
	z	0.1087	0.0651	0.0323	0.0158	0.0097	0.0056
<8	x	0.1757	0.1079	0.0536	0.0233	0.0079	0.0053
	y	0.2237	0.1588	0.0874	0.0275	0.0154	0.0111
	z	0.1065	0.0614	0.0269	0.0151	0.0085	0.0047

Lindenberger (1989) reports much lower gyro noise characteristics (several arcseconds) when a local-level platform INS is mounted in an aircraft.

Errors in the GPS updates will also introduce errors in the estimated attitude components. Since the integrated system relies on GPS updates to define the trajectory, the predicted INS attitudes will be corrected to fit the GPS data. Therefore, any errors in the GPS data will directly affect the attitude estimation. Table 5.9 summarizes the effect of various GPS position errors on the estimated azimuth for different GPS update rates. From the table it is clear that a higher update rate will result in a larger error in the estimated azimuth. For example, a 5 cm GPS error will cause an azimuth error of 147 arcsec when 1 Hz updates are used. This error is reduced to 10 arcsec when a GPS update is only available every 16 seconds.

Table 5.9
Effect of GPS Position Error on Estimated Azimuth
(Assumed aircraft speed of 70 m s^{-1})

		Azimuth Error (arcsec)			
Update Rate (s)	Distance (m)	1 cm GPS Error	5 cm GPS Error	10 cm GPS Error	15 cm GPS Error
1	70	29	147	294	441
4	280	7	37	74	111
8	560	4	19	37	56
16	1120	2	10	19	29
32	2240	1	5	9	14

For the present case of 4 second GPS updates, azimuth errors range from 7-111 arcsec, depending on quality of the GPS data. This clearly shows that for high accuracy attitude determination, accurate GPS data are needed.

CHAPTER 6

GPS/INS APPLIED TO AEROTRIANGULATION

The application of GPS/INS to aerotriangulation is investigated in this chapter using the results discussed in Chapter 5. Scenarios ranging from the use of several ground control points to the sole use of GPS/INS-derived exterior orientation and no ground control are analyzed to determine the requirements for large-scale mapping. The impact of systematic effects in the GPS/INS estimated positions as well as the calibration of interior orientation parameters are also discussed in this chapter.

6.1 Photogrammetric Test Area

As outlined in Chapter 5, the GPS/INS airborne test was conducted over an open pit mine in order to monitor the side-slope deformations. Table 6.1 lists the equipment and flight information pertaining to the collection of the photogrammetric data. A Zeiss RMK 15a/23 camera equipped with an electronic shutter release pulse was used. The camera focal length of 152 mm, along with a flying height of about 750 m above ground, translates to a photo scale of approximately 1:5000. A 70% sidelap and a 60% endlap in the photography gives extensive coverage of the test area.

Table 6.1
GPS/INS - Aerotriangulation Flight Data

Region:	**Hambach - Sophienhöhe**
Date:	**August 31, 1988**
Aircraft:	- Fixed-wing Cessna - Speed: 70 m s^{-1} (approximate)
Camera:	- Zeiss RMK 15a/23 Camera - Focal length: 152 mm
Flight:	- 13 strips of photography - 73 photos - 70% sidelap, 60% endlap - 1 : 5000 photo scale (approximate) - Altitude: 750 m above ground
Area:	- 3 km x 3 km (approximate) - Terrain elevations: -110 m to 260 m - 175 control points (1 cm accuracy)

Thirteen strips of photography for a total of 73 photos were taken, however, due to the poor satellite coverage, two flights at separate times were required to complete the photography. The aircraft travelled at approximately 250 km h^{-1} (70 m s^{-1}) and a photo was taken about every 4 seconds on each strip.

The mine covered an area of approximately 3 km in both the north-south and east-west directions. Figures 6.1 and 6.2 show the flight paths and photo coverage for the two flight directions. The number beside each strip indicates the strip number. In the southeast direction, shown in Figure 6.1, eight strips of photography (39 photos) were taken, whereas Figure 6.2 shows the cross flights in the southwest direction where five strips comprised of 34 photos were recorded. Terrain heights range from -110 m to 260 m (related to the local vertical datum) in the test area.

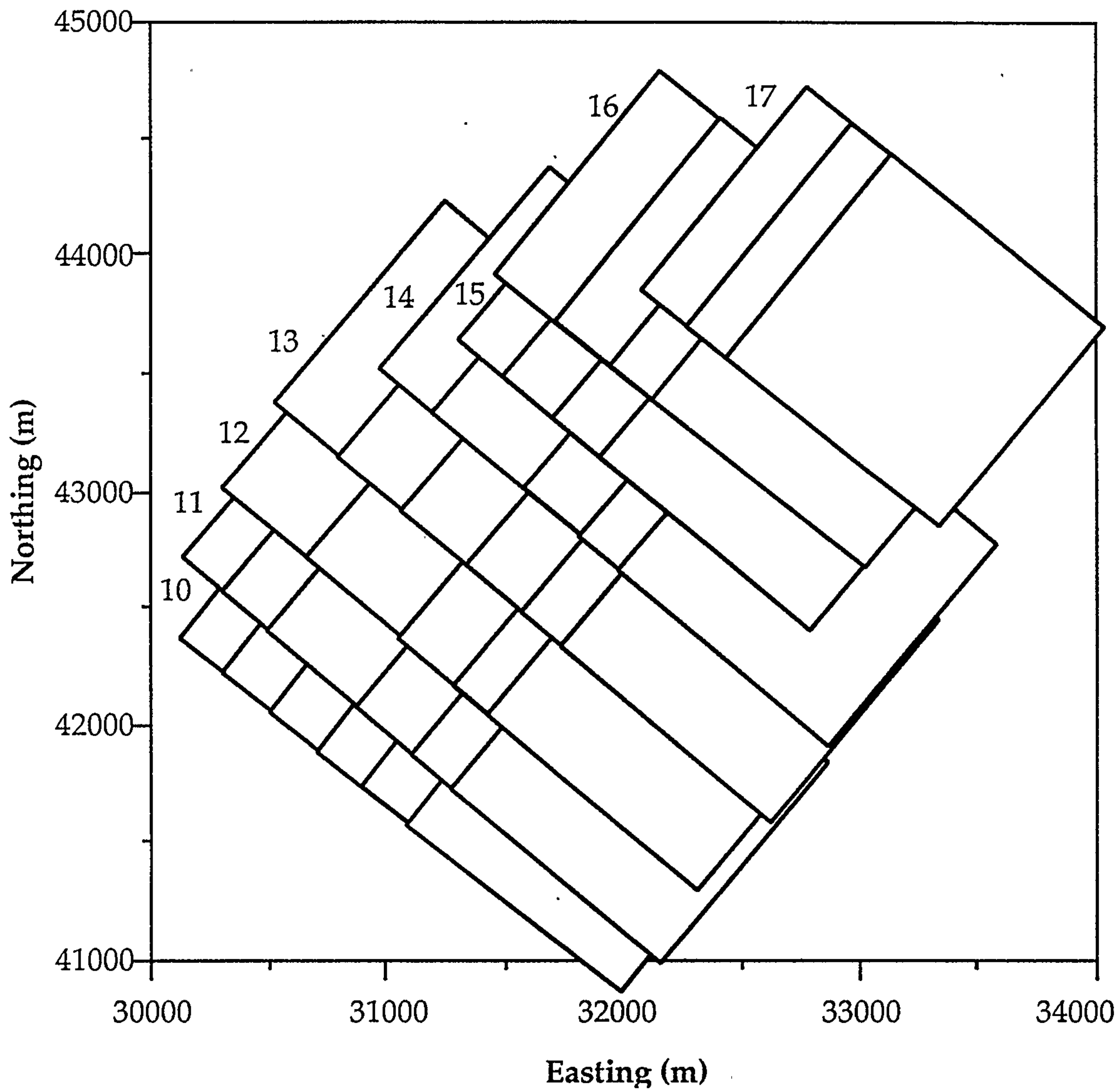

Figure 6.1
Flight Pattern in SE Direction

Figure 6.3 shows the distribution of control located in the test area. Dense ground stations (175 points) accurate to about the 1 cm level are available to allow for a statistically significant analysis of aerotriangulation with little or no ground control, by using these points as check points. This is discussed in more detail in Section 6.3.

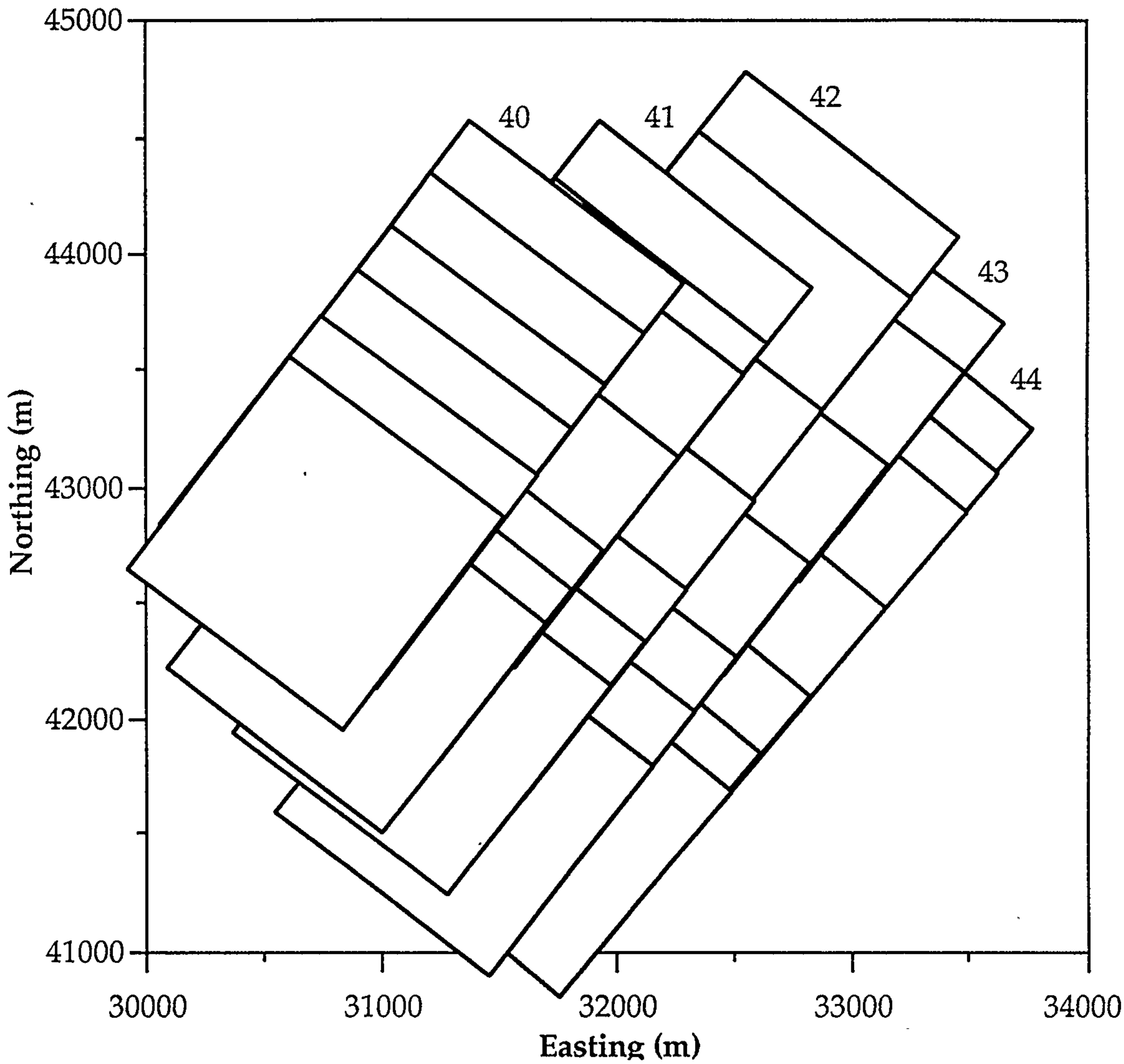

Figure 6.2
Flight Pattern in SW Direction

To test aerotriangulation with minimal or no ground control, a subset of photographs were identified for assessment. All photos could not be considered in the analysis since they were collected during two separate missions, and GPS/INS data were only available for one of the missions.

Also, computer memory constrained the number of strips that could be considered simultaneously. Figure 6.4 shows the two strips (numbers 10 and 12) and the associated ground control that were selected for analysis. These two strips contain 11 photos and capture 103 of the ground control points. By eliminating Strip 11 from the test block and only using Strips 10 and 12 (see Figure 6.1), the sidelap was reduced from 70% to about 35%, a typical sidelap used in most photogrammetric campaigns.

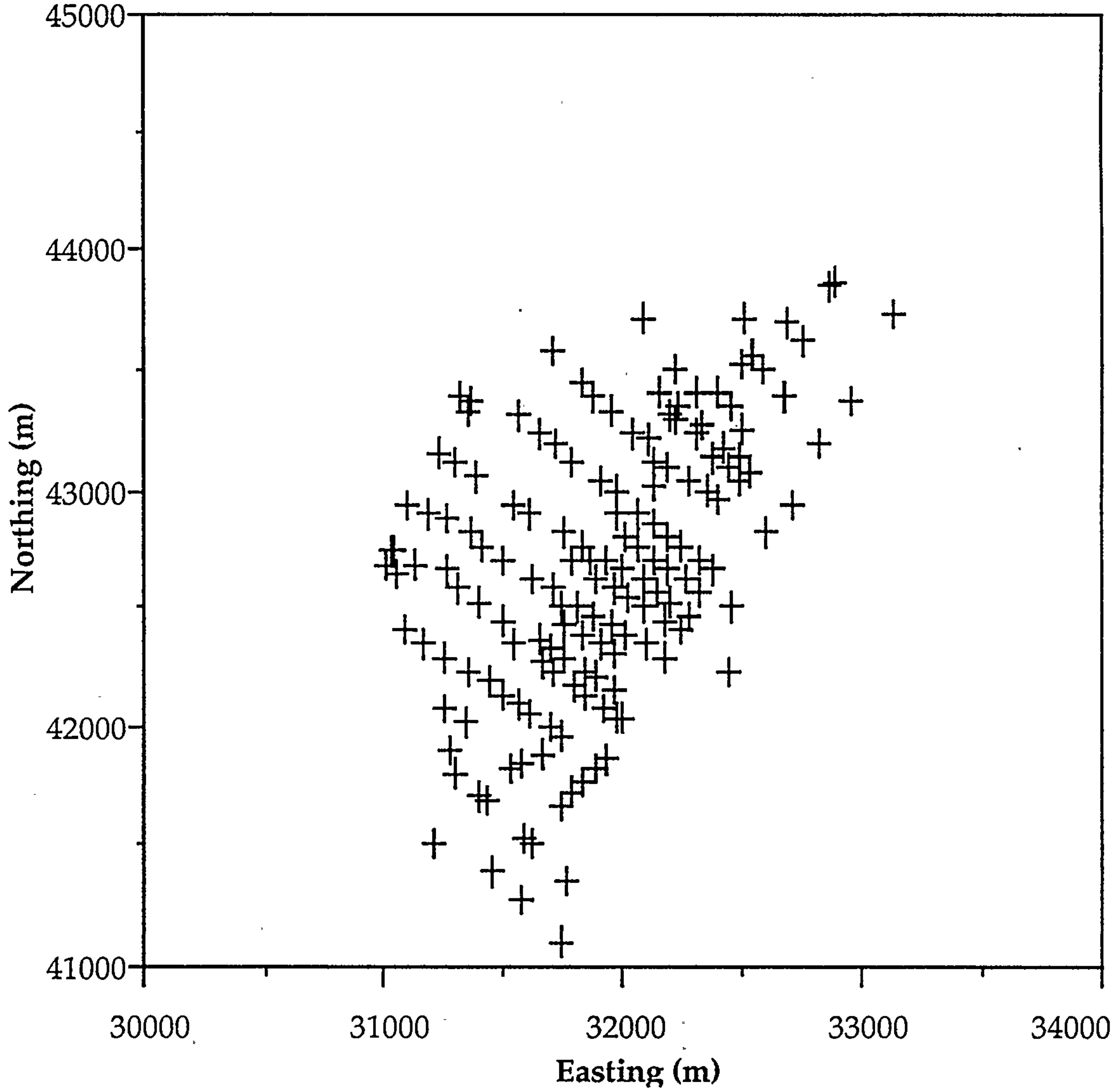

Figure 6.3
Ground Control Distribution

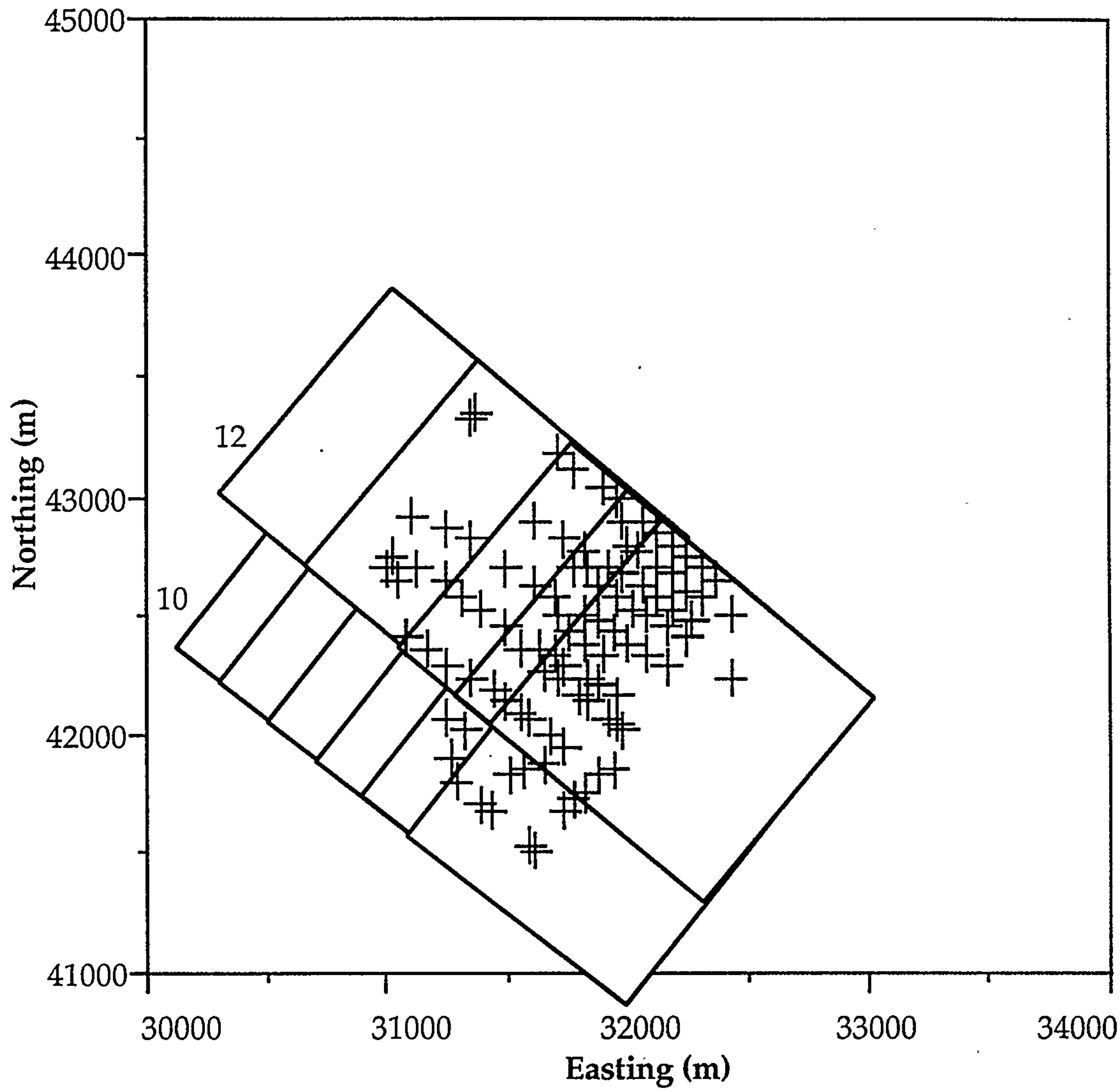

Figure 6.4
Photogrammetric Test Area

6.2 Photogrammetric Data Processing

The photogrammetric data were processed using **PCBUN**, a bundle adjustment program using the algorithms given in Section 3.5 and developed by Dr. M.A. Chapman, The University of Calgary. This package has the flexibility to process conventional photogrammetric adjustments in which the only control is from ground points, but it can also incorporate independent PC position and attitude information from an auxiliary positioning system. This program was used extensively in Goldfarb (1987) for a study of aerotriangulation without ground control using simulated data. **PCBUN** cannot estimate corrections to the calibrated interior orientation parameters so this was not attempted in any of the cases described in Section 6.3. However, the effect of deviations of the interior orientation during flight from the calibrated values is discussed in the sequel.

The output of **GPSINS** provides position and attitude as well as their statistical quality for each of the photos. The attitude components can be used to translate the GPS positions to the camera principal point using the measured offsets at the start of the mission. However, the estimated attitude was not used in the bundle adjustment since the accuracy of these parameters is well below the 10 arcsecond requirement (Section 5.5). Approximate values for camera orientation (ω, ϕ, κ) were used and standard deviations of five degrees were assigned in each case.

Estimated standard deviations from the Kalman filter estimator of ± 1-2 cm for the GPS/INS-derived PC positions were input to the bundle adjustment program as *a priori* information. The two cases of GPS/INS-derived PC positions were used in the bundle adjustment, namely those transformed with a three parameter translation of the block, and those transformed by a three parameter translation of each individual strip. Covariances between the three position components, output from **GPSINS**, were also included in the adjustment. Typical correlations for this particular data set are -0.347, 0.354, and 0.479, between the east-north, east-height, and north-height components, respectively. However, these values vary throughout the run due to the changing satellite geometry.

Photo coordinates measured by Rheinbraun were estimated to be accurate to ±3 μm. These coordinates were corrected for lens distortion, atmospheric refraction and subsequently for the earth curvature effect before being used in the bundle adjustment. All ground control were referenced to the Gauss-Krüger (3TM) mapping plane and a local vertical datum, so the adjustment was performed in this coordinate system.

6.3 Aerotriangulation without Ground Control

The first test of the bundle adjustment was for the case that no ground control were available. Therefore, the only source of external information are the PC positions determined from GPS/INS. The ground control, although known to an accuracy of ± 1 cm, were given standard deviations of ± 1000 m so they would not have any effect on the adjustment, however the estimated coordinates of these ground points from the bundle adjustment could then be compared to their 'true' values. This provides an assessment of the ability of aerotriangulation without ground control to estimate terrestrial points in the photogrammetric area.

PCBUN outputs the estimated exterior orientation parameters and the corrected ground 'check' point coordinates. The corresponding *a posteriori* statistics as well as the mean and RMS of the differences between the true and estimated check point coordinates were also recorded.

Table 6.2 summarizes the mean, RMS and standard deviation statistics of the differences for the case without ground control. Mean differences between the true and estimated ground check points are 10.8, 36.0 and 11.7 cm for the east, north and height components, respectively when a block three parameter translation is performed. Similarly, the RMS values of the differences are 12.6, 37.5 and 18.4 cm for each of the three coordinates. When the positions determined by a three parameter translation of each strip is used, the mean differences are -7.8, 10.4 and 15.1 cm, and the RMS statistics are 11.7, 14.9 and 15.7 cm. The improvement of the RMS values when a strip translation is done is significant, and demonstrates the requirement for proper initial ambiguity determination. There is a definite systematic effect present in the estimated coordinates of the ground check points in both cases, indicated by the large mean differences which result in the standard deviations (mean removed) being significantly better than the RMS values.

Table 6.2
Accuracy of Check Points with No Ground Control
(Sample Size = 103)

	Block/3 Parameter Translation			Strip/3 Parameter Translation		
Coordinate	Mean (cm)	RMS (cm)	Std Dev (cm)	Mean (cm)	RMS (cm)	Std Dev (cm)
East	10.8	12.6	6.5	-7.8	11.7	8.7
North	36.0	37.5	10.5	10.4	14.9	10.7
Height	11.7	18.4	14.2	15.1	15.7	4.3

Figures 6.5, 6.6 and 6.7 show the error in the estimated ground check points for the east, north and height components, respectively, when the block translation is performed. The position error is plotted against the ground control point number, sorted according to easting. Therefore, the errors on the left hand side of the figures are for ground control points located on the west side of the test area (see Figure 6.4). Also shown is the estimated 1σ *a posteriori* standard deviation of each ground point determined from the bundle adjustment using the *a priori* standard deviations of ±1-2 cm for the PC coordinates. Each figure shows that the estimated standard deviations of the ground points, generally less than 5 cm, is optimistic compared to the true error. This means that systematic effects present in the PC control have not been properly accounted for in the bundle adjustment. Therefore, a subsequent adjustment using *a priori* standard deviations of 15 cm for each of the PC coordinate components was run in order to compute more realistic *a posteriori* statistics. The value of 15 cm was chosen to represent the true accuracy of the PC coordinates, determined from external coordinate comparisons, as listed in Table 5.5. The revised ground coordinate standard deviations are also plotted in Figures 6.5, 6.6 and 6.7. Note that an overall shift in the *a priori* PC statistics will not change the estimated parameters, only the *a posteriori* standard deviations (Vanícek and Krakiwsky,1986).

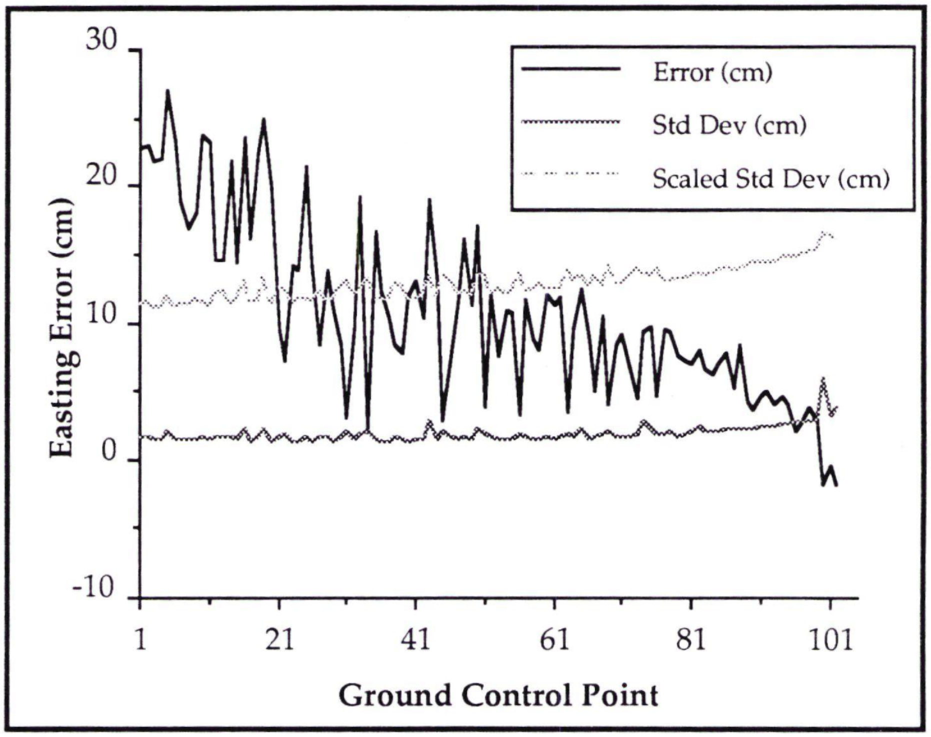

Figure 6.5
Easting Error with No Ground Control 3 Parameter Translation of Block

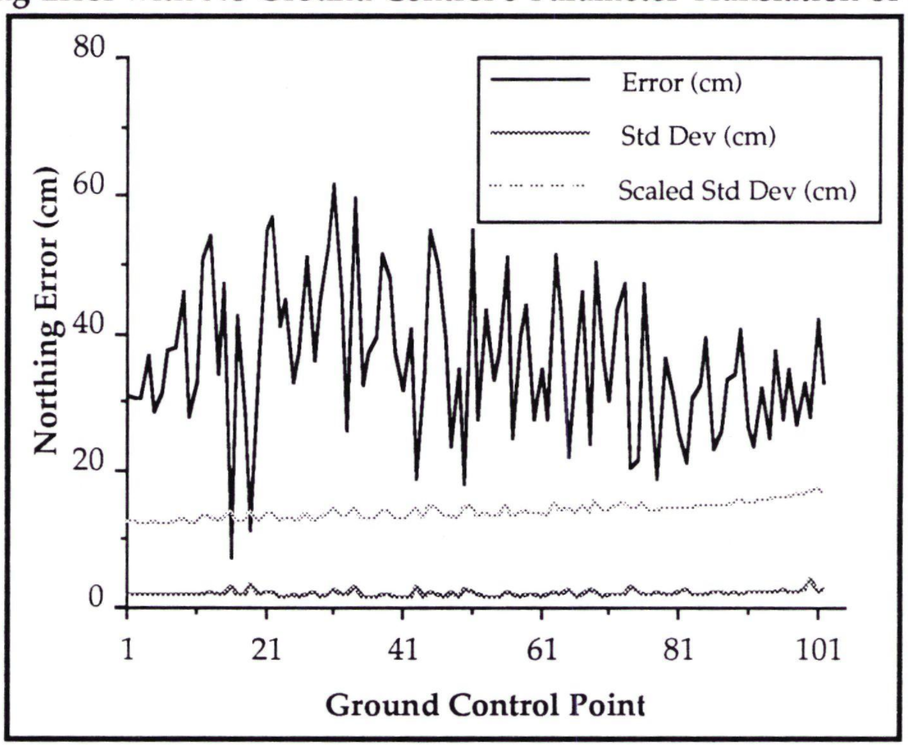

Figure 6.6
Northing Error with No Ground Control 3 Parameter Translation of Block

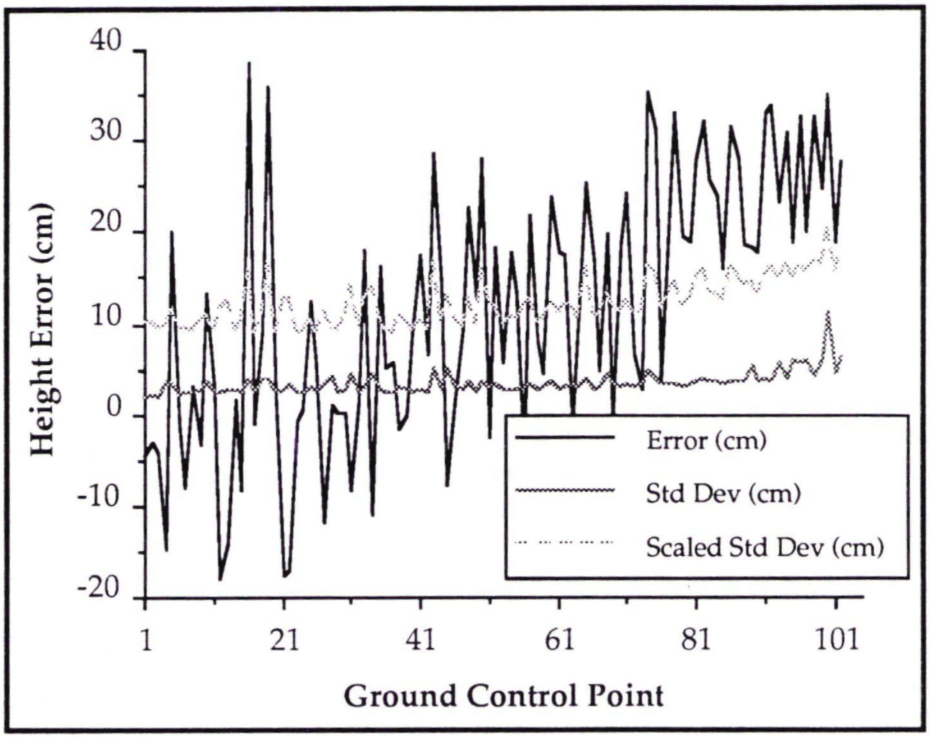

Figure 6.7
Height Error with No Ground Control and 3 Parameter Translation of Block

While Figures 6.5 and 6.7 show a drift in the error, the errors plotted in Figure 6.6 contain a bias. The drift in the easting error is approximately 25 cm over the entire test area and 35 cm in height. Although the revised *a posteriori* standard deviations plotted in the figures are closer to the true accuracy (within 3σ) of the photogrammetric results, a shift in the input PC statistics does not account for the drifts in the height and east components or the large bias in the north component. Most of these errors are due to incorrect initial ambiguity resolution, as demonstrated by the improved RMS statistics when the GPS/INS-derived PC positions are transformed to the local datum by a three parameter translation of each strip (Table 6.2). Figure 6.8 shows the revised height error when the strip translation is performed.

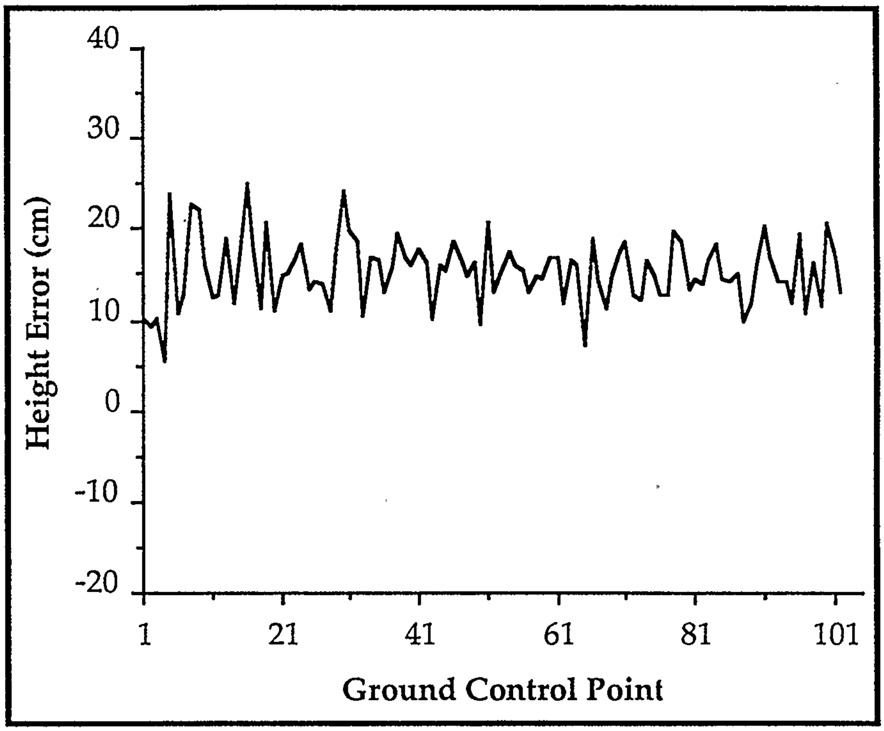

Figure 6.8
Height Error with No Ground Control and 3 Parameter Translation of Strip

Although the height drift has been removed, a bias remains in the results. This error is most likely due to the lack of self-calibration of the interior orientation parameters. The **PCBUN** program does not allow for the self-calibration of the interior orientation parameters (i.e., focal length and principal point offsets). However, for high-accuracy large scale photogrammetry, self-calibration is generally required since any deviation of the interior orientation from the laboratory calibrated values due to the environment will result in systematic effects occurring in the exterior orientation and transformed ground points (Ackermann,1988). This is especially pronounced in the case of aerotriangulation without ground control; the PC coordinates are constrained so the error will be propagated into the estimated camera attitude and ground points (i.e. no perspective compensation). For example, if the pre-calibrated focal length of a camera is 152.80 mm and is actually 152.82 mm during the flight due to temperature effects, a height bias of 10.0 cm will result if the photo scale is 1:5000. This bias will change by a few cm with variations in the photo scale, e.g. in the case of a large terrain relief. A bias of about 15 cm is evident in Figure 6.8 which translates into a focal length error of 30 μm. Similar effects can occur in planimetry due to principal point offset errors.

For self-calibration of the interior orientation parameters, at least one ground control point is required in the photo area (Schwarz et al.,1984). This may be accomplished in the differential GPS case by proper location of the monitor GPS receiver so it will be photographed during the mission. However, for reliable estimation of interior orientation, the use of two or three ground control points is recommended (Gruen and Runge,1988).

RMS requirements for ground control residuals for 1:5000 photography in Alberta are 12.5 cm in east-north, where

$$\text{east-north RMS} = \sqrt{(\text{east RMS})^2 + (\text{north RMS})^2} \qquad 6.1$$

and 10.0 cm in height (LISD,1989). The results indicated in Table 6.2 (block three parameter translation) and illustrated in Figures 6.5-6.7 clearly do not meet these requirements. When the strip three parameter translation is performed, the results are much closer to the requirements. However, in order to satisfy the large scale mapping accuracies with this particular data set, supplemental ground control must be included in the bundle adjustment.

6.4 Aerotriangulation with Minimal Ground Control

The advantage of incorporating ground control into the photogrammetric adjustment is that it provides an increased level of reliability in the results. Not only can self-calibration of the interior orientation parameters be performed, any datum transformation between the GPS datum (WGS-84) and a local datum can be explicitly modelled rather than using 'best-fitting' transformations. To overcome the datum transformation problem, at least three ground control points are required. Depending on the mapping area, the establishment of ground control using conventional differential GPS static surveys may be economical. Also, semi-kinematic techniques would be useful if the area is relatively small (Cannon,1990).

As a first test of aerotriangulation with minimal ground control, four ground control points were selected in one of the photos; points 9729, 3000, 9522 and 9311 in Figure 6.9. The use of these points in the bundle adjustment provides a reliable estimate of orientation for the last photo in strip 10. Since these points are close together, their establishment would be relatively inexpensive compared to the establishment of ground points throughout the photogrammetric area. An assessment can then be made as to the resulting ground point accuracy using this limited ground control configuration.

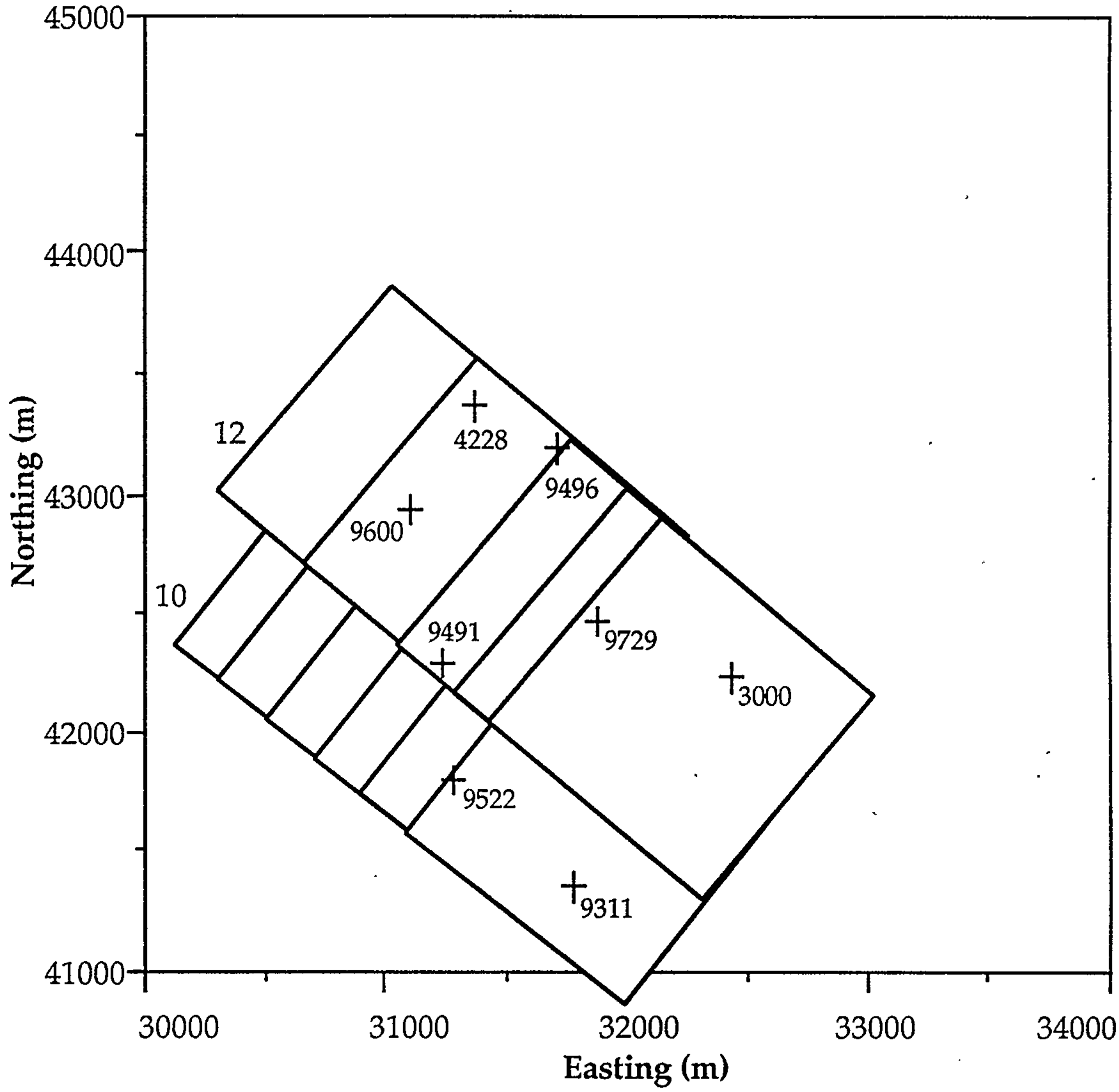

Figure 6.9
Selected Minimal Ground Control

Summarized in Table 6.3 are the results when these four ground control points are introduced along with the GPS/INS-derived PC coordinates for the block and strip translation cases. Mean values are greatly reduced in this case, indicating that much of the systematic effects evident in Figures 6.5 and 6.7 has been removed and thus the standard deviations are closer to the RMS values. RMS statistics of the differences has been significantly improved, especially in the north component, i.e. a reduction in the RMS statistics to 5.1, 10.5 and 8.5 cm (block translation) and 2.6, 5.5 and 5.9 cm (strip translation) in the east, north and height components is gained with the addition of the four ground control points. This significant improvement in the determination of the check points compared to the case without ground control is a result of the four points solving the exterior orientation of the last photo in strip 10. Constraining this photo will clearly affect the orientation of the remaining photos through the relative orientation process.

Table 6.3
Accuracy of Check Points using Four Ground Control Points

	Block/3 Parameter Translation			Strip/3 Parameter Translation		
Coordinate	**Mean (cm)**	**RMS (cm)**	**Std Dev (cm)**	**Mean (cm)**	**RMS (cm)**	**Std Dev (cm)**
East	3.9	5.1	3.3	0.5	2.6	2.6
North	8.8	10.5	5.7	4.0	5.5	3.8
Height	-6.4	8.5	5.6	-1.7	5.9	5.6

The planimetric RMS accuracy (i.e. east-north) is 11.7 cm (block translation) and 6.1 cm (strip translation), and along with the 8.5 cm (block translation) and 5.9 cm (strip translation) RMS accuracy in height, this configuration meets the Alberta requirement of 12.5 and 10.0 cm in east-north and height, respectively, for 1:5000 mapping (LISD,1989).

A second test of aerotriangulation with minimal ground control is the use of eight points; the four used in the above case, and the inclusion of an additional four in the first photo of strip 12 (points 9600, 9491, 4228 and 9496 in Figure 6.9). These eight points will tie down the two photos at opposite ends of the block. Shown in Table 6.4 are the mean, RMS and standard deviation statistics of the differences between the true and estimated check point coordinates. Compared to Table 6.3, there is not a significant improvement in the results when the eight ground control points are used instead of four, and although the reliability of the results is improved with additional ground control, the cost-effectiveness of the photogrammetric campaign may be increased substantially. Therefore, the use of eight points versus four would not be required for this particular data set.

Table 6.4
Accuracy of Check Points using Eight Ground Control Points

	Block/3 Parameter Translation			Strip/3 Parameter Translation		
Coordinate	Mean (cm)	RMS (cm)	Std Dev (cm)	Mean (cm)	RMS (cm)	Std Dev (cm)
East	1.5	3.2	2.8	0.2	2.1	2.1
North	7.8	9.6	5.6	3.7	5.0	3.4
Height	-6.5	8.4	5.3	-2.8	6.3	5.6

Since it has been determined that with four ground control points the Alberta large-scale mapping requirements can be achieved, a final test using less than four points was made to determine if fewer points could be utilized. Subsequent adjustments with one (point 9729) and two (points 9729 and 9311) ground control points were run with the results tabulated in Table 6.5. Mean and RMS statistics show an increasing accuracy with the addition of the ground control points. Even with one ground control point, a significant improvement is made compared to the case without any ground control. For strip translation of the GPS/INS results, the Alberta requirements are met. (12.5 cm in planimetry and 7.6 cm in height). The inclusion of two ground points gives a better estimate of the ground control points. More than two ground points are clearly required for the block translation case.

Table 6.5
RMS Accuracies of Check Points using One and Two Ground Control Points

	Block/3 Parameter Translation				Strip/3 Parameter Translation			
	1 Point		2 Points		1 Point		2 Points	
Coordinate	Mean (cm)	RMS (cm)	Mean (cm)	RMS (cm)	Mean (cm)	RMS (cm)	Mean (cm)	RMS (cm)
East	5.1	7.9	6.6	7.5	-4.4	7.2	-0.7	3.8
North	22.7	24.5	16.7	17.8	7.6	10.2	6.3	8.2
Height	3.0	8.4	-4.2	7.4	5.8	7.6	2.3	5.6

Figures 6.10, 6.11 and 6.12 show the errors in easting, northing and height when one ground control point is used. The addition of the ground control not only improves the check point accuracy, but also removes most of the trend evident in the 'no ground control' case. In summary, the use of ground control points has three distinct advantages compared to the 'no ground control' case, namely

1) Alberta 1:5000 mapping requirements: These requirements cannot be fulfilled using this particular data set without the addition of at least one ground control point in the bundle adjustment. The reliance on only PC

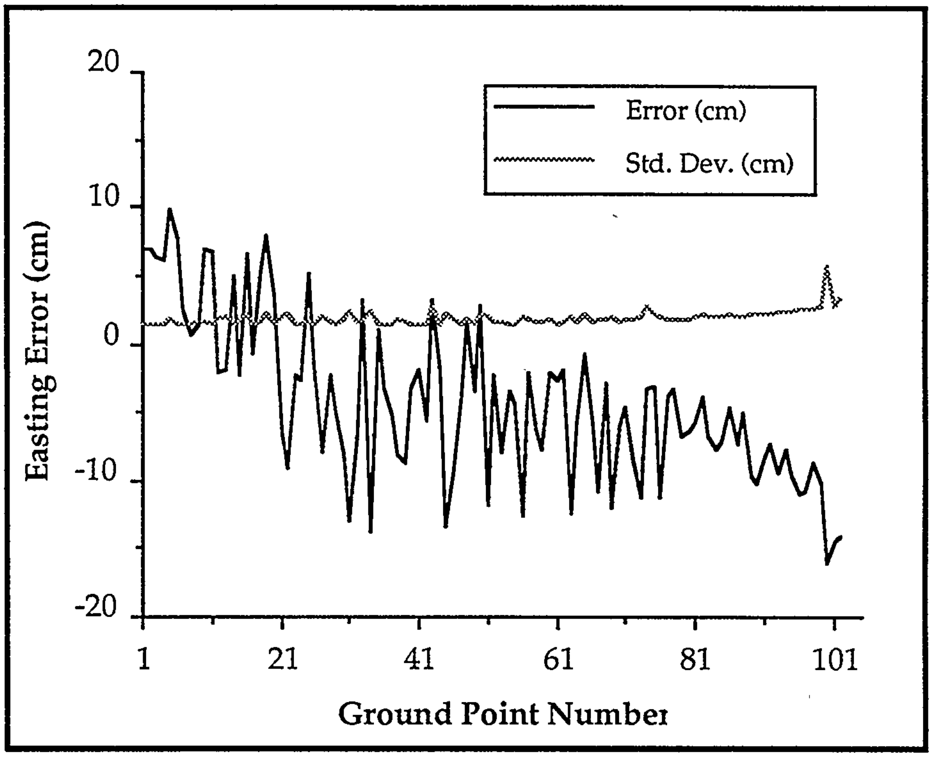

Figure 6.10
East Error using One Ground Control Point

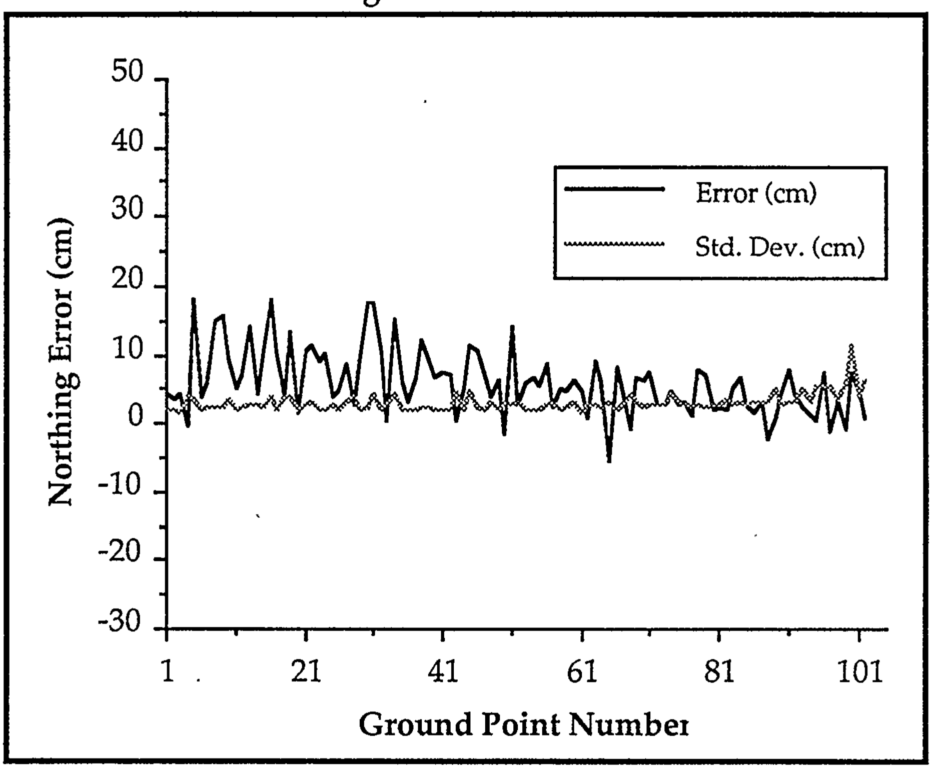

Figure 6.11
North Error using One Ground Control Point

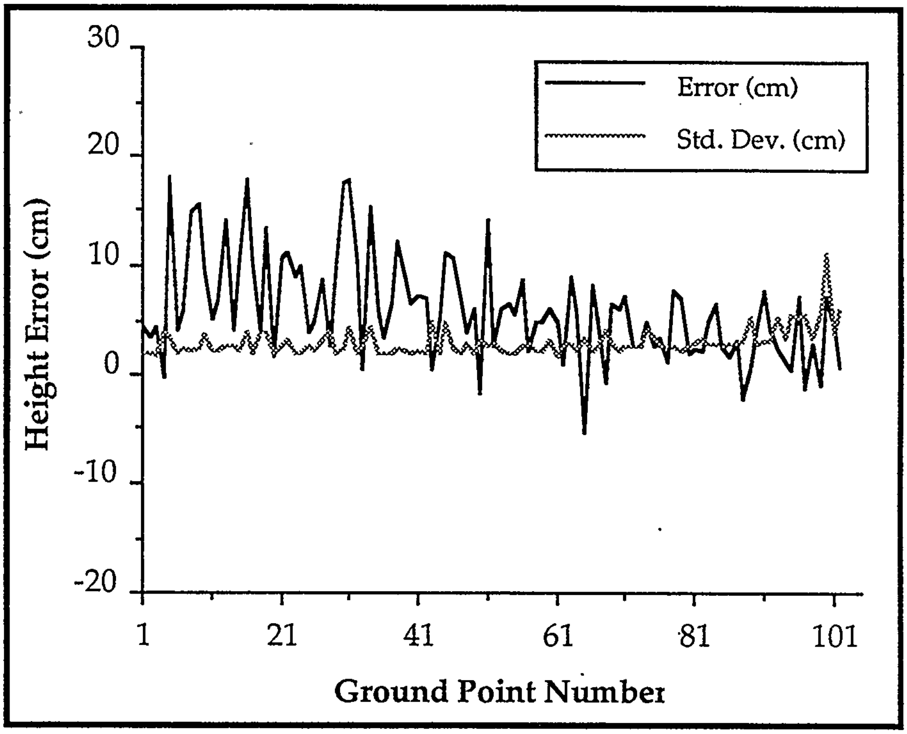

Figure 6.12
Height Error using One Ground Control Point

control is not sufficient. Two ground control points gives a further improvement in the tie point accuracy.

2) Interior Orientation Calibration: The use of one ground point will allow for an estimate of the camera interior orientation parameters in the bundle adjustment. This will reduce the occurrence of systematic effects in the estimated terrestrial ground points. Two or three ground points will give a *reliable* estimate of these parameters due to the addition of redundancy.

3) Determination of datum transformation: Since the relationship between WGS-84 and many local datums is not known, the establishment of three ground coordinates is sufficient to determine the transformation parameters.

CHAPTER 7

CONCLUSIONS AND RECOMMENDATIONS

The contribution of this research was in the development and testing of a GPS-INS integration strategy for precise airborne positioning. GPS modules developed through the research and existing INS modules were combined in a centralized Kalman filter approach. A GPS cycle slip detection and correction algorithm was developed and extensively tested using land data. The capabilty of the LTN 90-100 for precise attitude determination in airborne applications was also assessed. This had not previously been investigated. Finally, an application of GPS/INS to aerotriangulation was made to determine if ground control is required to meet large-scale mapping specifications. The application of GPS/INS to aerotriangulation with minimal or no ground control has not been studied in the past.

Precise kinematic positioning using GPS/INS was successfully demonstrated using land data collected on a well-controlled traverse. A subsequent application of this technology to the airborne case showed a slight decrease in positioning accuracy but was sufficient for a realistic assessment of using GPS/INS positions as control for aerotriangulation with minimal or no ground control. The following conclusions address the findings in both the kinematic positioning and aerotriangulation areas.

7.1 Conclusions

The following conclusions regarding GPS/INS integration for high-accuracy kinematic positioning can be made from this research:

1) The achievable accuracy of GPS/INS is at the level of a few centimetres in land mode when consistent GPS updates are available. Agreement with pre-surveyed control points was generally better than 5 cm in all three coordinates when four second measurement updates were performed.

2) The LTN 90-100 strapdown INS is effective for GPS carrier phase cycle slip detection and correction. Simulated cycle slips in the GPS carrier phase were successfully recovered using the predicted GPS antenna position based on integrated INS data. The advantage of using the INS for cycle slip detection and correction is that the number of satellites with cycle slips at any one epoch is not relevant. For the GPS-only case, cycle slip correction is severely affected when fewer than four satellites without cycle slips are tracked.

3) The 15 GPS/INS error states are adequate for cm-level kinematic positioning with high update rates. A centralized filter approach for error estimation is well-suited for real-time applications.

4) Outages in the GPS data will affect the achievable accuracy of GPS/INS positioning since the effectiveness of cycle slip detection and correction is reduced. Tests using the LTN 90-100 INS showed that when the GPS update rate is reduced from 4 to 32 seconds, the cycle slip detection capability deteriorated from 1 cycle to about 3 cycles. Although this will decrease the overall accuracy of the integrated system, an accuracy of less than 1 m after loss of GPS phase lock is adequate for many applications.

5) The INS is effective for position interpolation between GPS measurement epochs. It was demonstrated using airborne data that the high rate INS data can effectively interpolate the system position to an event (camera exposure in this case) between GPS updates.

6) The recovery of the correct initial GPS carrier phase ambiguities is imperative for precise kinematic positioning. Errors in the initial ambiguities will generate an apparent drift in the estimated position due to satellite geometry changes. Tests using land kinematic data over short monitor-remote separations (< 8 km) show that incorrect initial ambiguity determination will degrade the kinematic results as a function of time (and geometry). Apparent drifts in the remote receiver's position will result with a magnitude dependent on the ambiguity-coordinate correlation. For the land data used in the test, apparent drifts ranging from 0.03 to 0.08 mm s^{-1} were detected when an error of two cycles was simulated in one initial carrier phase ambiguity.

7) The *a posteriori* statistics of the GPS/INS positions are very optimistic compared to the true accuracy. Standard deviations of ± 1-2 cm were

estimated for the positions when the actual accuracy was computed to be ± 15 cm based on comparisons with independent positions. This is due to inadequate modelling of the residual GPS error sources.

8) Attitude determination from the LTN 90-100 was estimated to be accurate to about 0.4 degree in the roll and pitch components and 0.1 degree in azimuth when the orientation components were compared to photogrammetrically-derived values. Part of this disagreement is most likely due to relative movements between the INS and camera, while the remaining error is due to high INS gyro noise.

9) Accurate time-tagging between the GPS receiver and INS is necessary for precise kinematic positioning. The level of time synchronization is dependent on the vehicle speed; for example, the aircraft used in the photogrammetric test travelled at speeds reaching 70 m s^{-1}, so time-tagging should be better than 0.1 ms (about 7 mm in position) in order for the two data streams to be integrated properly.

For the application of GPS/INS to aerotriangulation with minimal or no ground control, a further series of conclusions can be made:

10) Aerotriangulation without ground control was demonstrated to be accurate to better than 15 cm in terms of the estimated tie point ground coordinates for 1:5000 photography. With the addition of one ground control point, the accuracy improved to 12.5 cm in the east-north component and 7.6 cm in height, which meets the Alberta large scale

mapping requirements of 12.5 and 10 cm in the east-north and height components, respectively.

11) The transformation of GPS/INS-derived positions into a local datum can pose a significant problem for reliable aerotriangulation with minimal or no ground control. Although the problem becomes non-existent when ground points are reference to WGS-84 using static GPS techniques, this cannot be accomplished in the 'no ground control' case. The post-processing technique of using transformation models can lead to incorrect and physically misleading methods which absorb inherent errors in the estimated positions.

12) Deviations from the pre-calibrated camera interior orientation parameters during photography will affect the bundle block adjustment such that biases will be introduced into estimated tie point ground coordinates. These biases can reach a few dm, depending on the photo scale.

13) The attitude determined from the LTN 90-100 using the present data set and model is not sufficiently accurate to be incorporated into the bundle block adjustment since accuracies of better than ten arcseconds are required.

7.2 Recommendations

Based on the results of this research, the following recommendations regarding improved performance using GPS/INS for precise kinematic positioning and aerotriangulation with no ground control can be made:

1) Improved GPS hardware would be beneficial from a users point of view. Warnings when cycle slips are detected in the receiver, which is currently implemented on some receivers, would assist in the detection phase. This is important, especially when INS errors may be significant, so a separation of INS errors and GPS cycle slips can be made.

2) The operational procedures for precise kinematic positioning should be improved. The initial separation between the monitor and remote GPS receivers should be small (e.g. < 1 km) so that the initial integer ambiguities can be easily recovered with a short static observation span (e.g. 20 minutes).

3) When operational constraints dictate that a monitor receiver be placed far from the initial remote position (e.g. test area is located far away from the airport), additional monitor receivers should be used. For example, one monitor can be located near the airport and another placed in the test area. Improved ambiguity resolution and cycle slip detection/correction will be possible with additional monitor receivers.

4) Improved error estimation through the inclusion of adaptive filtering techniques should be investigated. The implementation of these techniques may benefit those kinematic applications where the vehicle experiences a wide range of dynamic conditions. Another model improvement necessary for GPS-only or GPS/INS kinematic positioning is a more realistic statistical assessment of the estimated results. With the current GPS model, the *a posteriori* variances are very optimistic compared to the true accuracy.

5) A refined INS model should be investigated in order to extend accurate bridging during intervals of GPS outages. This would not only increase the integrated system accuracy but also the reliability of the results and the range of environments in which the system could be used.

6) The hardware configuration for precise attitude determination in airborne mode should be modified. For the airborne photogrammetric tests performed as part of this research, the INS and camera were separated in the aircraft. Furthermore, the camera was mounted on shock-absorbers so small movements of the camera may exist. In order to minimize any relative movements between the INS and camera, the INS should be 'hard-mounted' on the camera so they experience identical dynamic conditions.

7) A further analysis of precise attitude determination in a kinematic environment using the LTN 90-100 is necessary. The technique of smoothing the noise of the output gyro measurements while retaining the lower frequency vehicle dynamic information should be tested to determine its feasibility for improved attitude determination.

8) Self-calibration of the aerotriangulation interior orientation elements should be incorporated into the block adjustment. A definitive transformation between a local datum and WGS-84 should be made to so physically misleading transformation models will not be used. Also, further aerotriangulation tests should be conducted over larger areas and at various photo scales to assess the feasibility of GPS/INS in these cases.

Overall, the potential of GPS-INS integration for precise kinematic positioning has been demonstrated for both the land and airborne environments. However, numerous challenges remain before the potential of this exciting technology will be fully realized. With improved hardware design, operational procedures and processing techniques, not only will accuracies be further improved, the reliability of the estimated results will be strengthened and the applications of this integrated technology will extend far beyond the aerotriangulation case used in this research.

REFERENCES

Abidin, H. (1990), *Extra Widelaning for 'On the Fly' Ambiguity Resolution: Simulation of Mulipath Effects,* **Proceedings of the Third International Technical Meeting of the Satellite Division of the ION, GPS-90,** Colorado Springs, September 19-21.

Ackermann, F. (1988), *Combined Adjustment of Airborne Navigation Data and Photogrammetric Blocks,* **Proceedings of the 16th International Congress of the International Society for Photogrammetry and Remote Sensing,** Commision III, Kyoto, July 1-10.

Allison, T. and R. Eshenbach (1989), *Real-Time Cycle-slip Fixing During Kinematic Surveys,* **Proceedings of the 5th International Geodetic Symposium on Satellite Positioning,** Las Cruces, March 13-17.

American Society of Photogrammetry (ASP) (1980), **Manual of Photogrammetry,** Fourth Edition, Church Falls, VA.

Andersen, O. (1989), *Experience with Kinematic GPS During Aerial Photography in Norway,* **Proceedings of the 42nd Photogrammetric Week, Stuttgart University, Schriftenreihe 13,** Stuttgart, September 11-16.

Baustert, G., M.E. Cannon, E. Dorrer, G. Hein, H. Krauss, H. Landau, K.P. Schwarz and Ch. Schwiertz (1989), *German-Canadian Experiment in Airborne INS-GPS Integration for Photogrammetric Applications,* **Proceedings of the IAG Geodesy Symposia 102,** Springer Verlag, New York.

Beutler, G., I. Bauersima, W. Gurtner, M. Rothacher, T. Schildknecht and A. Geiger (1988), *Atmospheric Refraction and Other Important Biases in GPS Carrier Phase Observations,* **Atmospheric Effects on Geodetic Space Measurements,** Monograph 12, School of Surveying, University of New South Wales.

Black, H.D. and A. Eisner (1984), *Correcting Satellite Doppler Data for Tropospheric Effects,* **Proceedings of the International Symposium on the Use of Artificial Satellites for Geodesy and Geodynamics,** National Technical University of Athens.

Blais, J.A.R. (1985), **Least Squares Block Adjustment of Stereoscopic Models and Error Analysis,** Report No. 30001, Department of Surveying Engineering, The University of Calgary.

Brown, R.G. (1983), **Introduction to Random Signal Analysis and Kalman Filtering,** John Wiley & Sons, New York.

Cannon, M.E. (1987), **Kinematic Positioning Using GPS Pseudorange and Carrier Phase Observations,** Report No. 20019, Department of Surveying Engineering, The University of Calgary.

Cannon, M.E. (1990), *High-Accuracy GPS Semikinematic Positioning: Modeling and Results,* **Navigation,** Journal of the Institute of Navigation, Vol. 37, No. 1, pp. 53-64.

Cannon, M.E., G. Lachapelle, H. Ayers and K.P. Schwarz (1990), *A Comparison of SEMIKIN and KINSURVY for Kinematic Applications,* **Proceedings of the Third International Technical Meeting of the Satellite Division of the ION, GPS-90,** Colorado Springs, September 19-21.

Colomina, I. (1988), *High Altitude Aerial Triangulation without Ground Control,* **Proceedings of the 16th International Congress of the International Society for Photogrammetry and Remote Sensing,** Commision III, Kyoto, July 1-10.

Colomina, I. (1989), *Combined Adjustment of Photogrammetric and GPS Data,* **Proceedings of the 42nd Photogrammetric Week, Stuttgart University, Schriftenreihe 13,** Stuttgart, September 11-16.

Czompo, J. (1990), *Use of Spectral Methods in Strapdown ISS Data Processing,* **Proceedings of the International Symposium on Kinematic Systems for Geodesy, Navigation and Remote Sensing**, Banff, September 10-14, Springer-Verlag, New York.

Dayton, R.B. and J.T. Nielson (1989), *A Flight Test Comparison of Two GPS/INS Integration Approaches,* **Proceedings of the Second International Technical Meeting of the Satellite Division of the ION, GPS-89**, Colorado Springs, September 27-29.

Dorrer, E. and Ch. Schwiertz (1990), *Kinematic GPS and Aerial Triangulation - A Comparative Study,* Presented at the **ISPRS Commission III Symposium, Progress in Data Analysis**, May 20-24, Wuhan, China.

Friess, P. (1988), *Empirical Accuracy of Positions Computed from Airborne GPS Data,* **Proceedings of the 16th International Congress of the International Society for Photogrammetry and Remote Sensing**, Commision III, Kyoto, July 1-10.

Gelb, A., ed. (1974). **Applied Optimal Estimation**, M.I.T. Press, Cambridge, Massachusetts.

Georgiadou, Y. and A. Kleusberg (1988), *On the Effect of Ionospheric Delay on Geodetic GPS Relative Positioning,* **Manuscripta Geodeatica**, Vol. 13, No.2, pp. 1-8.

Georgiadou, Y. and A. Kleusberg (1989), *Multipath Effects in Static and Kinematic GPS Positioning,* **IAG Symposium 102 on Global Positioning System: An Overview**, Springer Verlag, New York, pp. 82-89.

Goad, C.C. (1990), *Optimal Filtering of Pseudoranges and Phases from Single-frequency GPS Receivers,* **Navigation**, Vol. 37, No.3, pp. 249-262.

Goad, C.C. and L. Goodman (1974), *A Modified Hopfield Tropospheric Refraction Correction Model,* **Presented at the Fall Annual Meeting of the American Geophysical Union**, San Francisco, December 12-17.

Goldfarb, J.M. (1987), **Aerotriangulation Using An INS-Differential GPS**, Report Number 20022, Department of Surveying Engineering, The University of Calgary.

Gruen, A. and A. Runge (1988), *The Accuracy Potential of Self-Calibrating Aerial Triangulation without Ground Control*, **Proceedings of the 16th International Congress of the International Society for Photogrammetry and Remote Sensing**, Commision III, Kyoto, July 1-10.

Hatch, R. (1990), *Instantaneous Ambiguity Resolution*, **Proceedings of the International Sysposium on Kinematic Positioning for Geodesy, Surveying and Remote Sensing**, Springer Verlag, New York.

Hemesath, N.B. (1980), *Performance Enhancements of GPS User Equipment*, **Global Positioning System, Volume I**, Institute of Navigation, Washington, D.C.

Hemesath, N.B. and J.M. Bruckner (1988), *DARPA's Advanced Technology GPS Chipset*, **Proceedings of the First International Meeting of the Institute of Navigation**, GPS-88, The Institute of Navigation, Washington, D.C.

Hopfield, H.S. (1963), *The Effect of Tropospheric Refraction on the Doppler Shift of Satellite Data*, **Journal of Geophysical Research**, Vol. 68, No. 18, pp. 5157-5168.

Keel, G., H. Jones, G. Lachapelle, R. Moreau and M. Perron (1989), *A Test of Airborne Kinematic GPS Positioning for Aerial Photography*, **Photogrammetric Engineering**, Vol. 55, No. 12, pp. 1727-1730.

Klobuchar, J. (1983), **Ionospheric Effects on Earth-Space Propagation**, Report No. ERP-866, Air Force Geophysics Laboratory, Hanscom AFB, Mass.

Knickmeyer, E. T. (1990), **Vector Gravimetry by a Combination of Inertial and GPS Satellite Measurements**, Report No. 20035, Department of Surveying Engineering, The University of Calgary.

Krakiwsky, E.J., G. Lachapelle, and K.P. Schwarz (1990), **Assessment of Emerging Technologies for Future Navigation Systems in the Canadian Transportation Sector**, Publication 60007, Department of Surveying Engineering, The University of Calgary.

Kremer, G.T., R.M. Kalafus, P.V.W. Loomis and J.O. Reynolds (1989), *The Effect of Selective Availability on Differential Corrections,* **Proceedings of the Second International Technical Meeting of the Satellite Division of the ION, GPS-89**, Colorado Springs, September 27-29.

Lachapelle, G., and M.E. Cannon (1986), *Single and Dual Frequency GPS Results for Baselines of 10 to 500 Km,* **The Canadian Surveyor**, Vol. 40, No.2, pp. 173-183.

Lachapelle, G., P. Kielland and M. Casey (1991), *GPS for Marine Navigation and Hydrography,* **Presented at the Fourth Biennal Canadian Hydrographic Conference**, Rimouski, April 15-19.

Lachapelle, G., W. Falkenberg, D. Neufeldt and P. Kielland (1989), *Marine DGPS Using Code and Carrier in a Multipath Environment,* **Proceedings of the Second International Technical Meeting of the Satellite Division of the ION, GPS-89**, Colorado Springs, September 27-29.

Land Information Services Division (1989), **General Specifications for Large Scale Mapping**, Interdepartmental Committee on Surveying and Mapping, Alberta Forestry, Lands and Wildlife, Edmonton, Alberta.

Lapucha, D. (1990), **Precise GPS/INS Positioning for a Highway Inventory System**, Report No. 20038, Department of Surveying Engineering, The University of Calgary.

Lapucha, D., K.P. Schwarz, M.E. Cannon and H. Martell (1990), *The Use of INS/GPS in a Highway Survey System,* **Proceedings of the IEEE PLAN'S 90**, Las Vegas, March 20-23.

Lindenberger, J. (1989), *Quality Analysis of Platform Orientation Parameters for Airborne Laser Profiling Systems,* **High Precision Navigation,** Springer-Verlag, Berlin.

Lu, G. and G. Lachapelle (1990), *Reliability Analysis Applied to Kinematic GPS Position and Velocity Estimation,* **Proceedings of the International Sysposium on Kinematic Positioning for Geodesy, Surveying and Remote Sensing,** Springer Verlag, New York.

Lucas, J. and G. Mader (1989), *Recent Advances in Kinematic GPS Photogrammetry,* **Journal of Surveying Engineering,** Vol. 115, No. 1, pp. 78-92.

Mader, G. (1986), *Dynamic Positioning Using GPS Carrier Phase Measurements,* **Manuscripta Geodaetica,** Vol. 11, No. 4, pp. 272-277.

Martin, E.H. (1980), *GPS User Equipment Error Models,* **Global Positioning System, Volume I,** Institute of Navigation, Washington, D.C.

Matthews, A. and H. Welter (1989), *Cost-Effective, High-Accuracy Inertial Navigation,* **Navigation,** Vol. 36, No. 2, pp. 157-171.

McLellan, J.F., J.B. Schleppe and M.E. Cannon (1990), *Performance of a GPS-Based Automatic Vehicle Location System within Urban Canyons,* **Proceedings of the 2nd International Symposium on Precise Positioning with the Global Positioning System,** Ottawa, September 3-7.

Meehan, T.K., T.N. Munson, J.B. Thomas, J.M. Srinivasan, D.J. Spitzmesser, L.E. Young and R.E. Neilan (1987), *Rogue - A New High Accuracy Digital GPS Receiver,* **Presented at the XIX General Assembly of the IUGG,** Vancouver, August 9-22.

Merrell, R.L., H.S. Bains, M.P. Leach, D.J. Kurtin and J.R. Lucas (1990), *Refinements of the GPS/Photogrammetric Surveying Capability in the Texas State Department of Highways and Public Transportation,*

Proceedings of the Third International Technical Meeting of the Satellite Division of the ION, GPS-90, Colorado Springs, September 19-21.

Moffitt, F.H. and E.M. Mikhail (1980), **Photogrammetry**, Harper & Row, New York.

Remondi, B.W. (1984), **Using the Global Positioning System (GPS) Phase Observable for Relative Geodesy: Modeling, Processing, and Results**, CSR-84-2, Center for Space Research, The University of Texas at Austin, Austin.

Russell, S.S. and J.H. Schaibly (1980), *Control Segment and User Performance,* **Global Positioning System, Volume I**, Institute of Navigation, Washington, D.C.

Schwarz, K.P. (1980), *Inertial Surveying Systems - Experience and Prognosis,* **The Canadian Surveyor**, Vol. 34, No. 1, pp. 41-53.

Schwarz, K.P. and Z. Liu (1990), *An Evaluation of Alignment Procedures for Strapdown Inertial Systems,* **Proceedings of the International Sysposium on Kinematic Positioning for Geodesy, Surveying and Remote Sensing**, Springer Verlag, New York.

Schwarz, K.P., C.S. Fraser and P.C. Gustafson (1984). *Aerotriangulation without Ground Control,* **International Archives of Photogrammetry and Remote Sensing**, Vol. 25, Part A1, Rio de Janeiro, June 16-29.

Schwarz, K.P., M.E. Cannon and R.V.C. Wong (1989), *A Comparison of GPS Kinematic Models for the Determination of Position and Velocity Along a Trajectory,* **Manuscripta Geodaetica**, Vol. 14, pp. 345-353.

Seeber, G. and G. Wübbena (1989), *Kinematic Positioning with Carrier Phase and 'On the Way' Ambiguity Resolution,* **Proceedings of the 5th International Geodetic Symposium on Satellite Positioning**, Las Cruces, March 13-17.

Teunissen, P.J.G. and M.A. Salzmann (1989), *A Recursive Slippage Test for Use in State-Space Filtering,* **Manuscripta Geodeatica**, Vol. 14, pp.383-390.

Thyer, N. (1987), **Effectiveness of Auxiliary Positioning Systems in Aerial Photogrammetry**, Report Number 20023, Department of Surveying Engineering, The University of Calgary.

Thyer, N.H., J.A.R. Blais and M.A. Chapman (1989), *Integration of an Inertial System with High-Altitude Photogrammetry over Rugged Terrain,* **CISM Journal**, Vol. 43, No. 1, pp. 9-19.

Tolman, B.W., J.R. Clynch, D.S. Coco and M.P. Leach (1990), *The Effect of Selective Availability on Differential GPS Positioning,* **Proceedings of the Second International Symposium on Precise Positioning with the Global Positioning System, GPS-90**, Ottawa, September 3-7.

Tralli, D.M. and S.M. Lichten (1990), *Stochastic Estimation of Tropospheric Path Delays in Global Positioning System Geodetic Measurements,* **Bulletin Géodésique**, Vol. 64, No. 2, pp.127-159.

Van Dierendonck, A.J., S.S. Russell, E.R.Kopitzke and M. Birnbaum (1981), *The GPS Navigation Message,* **Global Positioning System, Volume I**, Institute of Navigation, Washington, D.C.

Vanîcek, P. and E. Krakiwsky (1986), **Geodesy: The Concepts**, Second Edition, Elsevier Science, Amsterdam.

Vegt, v.d., H.J.W. (1989), *GPS Test Flight Flevoland,* **Proceedings of the 42nd Photogrammetric Week, Stuttgart University, Schriftenreihe 13**, Stuttgart, September 11-16.

Vegt, v.d., H.J.W., D. Boswinkel and R. Witmer (1988), *Utilisation of GPS in Large Scale Photogrammetry,* **Proceedings of the 16th International Congress of the International Society for Photogrammetry and Remote Sensing**, Commision III, Kyoto, July 1-10.

Wei, M. and K.P. Schwarz (1990, *Testing a Decentralized Filter for GPS/INS Integration,* **Proceedings of the IEEE PLAN'S 90**, Las Vegas, March 20-23.

Wells, D.E., N. Beck, D. Delikaraoglou, A. Kleusberg, E.J. Krakiwsky, G. Lachapelle, R.B. Langley, M. Nakiboglou, K.P. Schwarz, J.M. Tranquilla and P. Vanícek (1987), **Guide to GPS Positioning**, University of New Brunswick Graphic Services, Fredericton.

Wong, R.V.C. (1985), **A Kalman Filter-Smoother for an Inertial Survey System of Local Level Type**, Report Number 20001, Department of Surveying Engineering, The University of Calgary.

Wong, R.V.C. (1988), **Development of a RLG Strapdown Inertial Survey System**, Report Number 20027, Department of Surveying Engineering, The University of Calgary.

Wong, R.V.C., K.P. Schwarz and M.E. Cannon (1988), *High Accuracy Kinematic Positioning by GPS-INS*, **Navigation**, Vol. 35, No. 2, pp. 275-287.

Wübbena, G. (1989), *The GPS Adjustment Software Package GEONAP: Concepts and Models*, **Proceedings of 5th International Geodetic Symposium on Satellite Positioning, Physical Science Laboratory**, New Mexico State University.

APPENDIX

GPS OBSERVATION PARTIAL DERIVATIVES

1) Paritial derivatives of double differenced carrier phase (for satellites i and j):

<u>With respect to latitude:</u>

$$\frac{\partial \Delta\nabla\Phi^{ij}}{\partial \phi_r} = \frac{\partial \Delta\nabla\Phi^{ij}}{\partial x_r} \frac{\partial x_r}{\partial \phi_r} + \frac{\partial \Delta\nabla\Phi^{ij}}{\partial y_r} \frac{\partial y_r}{\partial \phi_r} + \frac{\partial \Delta\nabla\Phi^{i}}{\partial z_r} \frac{\partial z_r}{\partial \phi_r}$$

<u>With respect to longitude:</u>

$$\frac{\partial \Delta\nabla\Phi^{ij}}{\partial \lambda_r} = \frac{\partial \Delta\nabla\Phi^{ij}}{\partial x_r} \frac{\partial x_r}{\partial \lambda_r} + \frac{\partial \Delta\nabla\Phi^{i}}{\partial y_r} - \frac{\partial y_r}{\partial \lambda_r} + \frac{\partial \Delta\nabla\Phi^{i}}{\partial z_r} \frac{\partial z_r}{\partial \lambda_r}$$

<u>With respect to height:</u>

$$\frac{\partial \Delta\nabla\Phi^{ij}}{\partial h_r} = \frac{\partial \Delta\nabla\Phi^{i}}{\partial x_r} \frac{\partial x_r}{\partial h_r} + \frac{\partial \Delta\nabla\Phi^{i}}{\partial y_r} \frac{\partial y_r}{\partial h_r} + \frac{\partial \Delta\nabla\Phi^{i}}{\partial z_r} \frac{\partial z_r}{\partial h_r}$$

where
$$\frac{\partial \Delta\nabla\Phi^{ij}}{\partial x_r} = \frac{\partial \Delta\Phi^{i}}{\partial x_r} - \frac{\partial \Delta\Phi^{j}}{\partial x_r} = \frac{-(x^i - x_r)}{\rho_i} + \frac{(x^j - x_r)}{\rho_j}$$

$$\frac{\partial \Delta\nabla\Phi^{ij}}{\partial y_r} = \frac{\partial \Delta\Phi^{i}}{\partial y_r} - \frac{\partial \Delta\Phi^{j}}{\partial y_r} = \frac{-(y^i - y_r)}{\rho_i} + \frac{(y^j - y_r)}{\rho_j}$$

$$\frac{\partial \Delta\nabla\Phi^{ij}}{\partial z_r} = \frac{\partial \Delta\Phi^{i}}{\partial z_r} - \frac{\partial \Delta\Phi^{j}}{\partial z_r} = \frac{-(z^i - z_r)}{\rho_i} + \frac{(z^j - z_r)}{\rho_j}$$

$$\frac{\partial x_r}{\partial \phi_r} \approx -(R_N + h)\sin\phi_r \cos\lambda_r$$

$$\frac{\partial x_r}{\partial \lambda_r} = -(R_N + h)\cos\phi_r \sin\lambda_r \quad ; \quad \frac{\partial x_r}{\partial h_r} = \cos\phi_r \cos\lambda_r$$

$$\frac{\partial y_r}{\partial \phi_r} \approx -(R_N + h)\sin\phi_r \sin\lambda_r$$

$$\frac{\partial y_r}{\partial \lambda_r} = (R_N + h)\cos\phi_r \cos\lambda_r \quad ; \quad \frac{\partial y_r}{\partial h_r} = \cos\phi_r \sin\lambda_r$$

$$\frac{\partial z_r}{\partial \phi_r} \approx (R_N (1-e^2) + h)\cos\phi_r$$

$$\frac{\partial z_r}{\partial \lambda_r} = 0 \quad ; \quad \frac{\partial z_r}{\partial h_r} = \sin\phi_r$$

and x_r, y_r, z_r ... are the cartesian coordinates of the remote receiver

ρ ... is the computed distance between the receiver and the satellite, e.g. $\mid r^i - r_r \mid$

R_N ... is the prime vertical radius of curvature.

2) Paritial derivatives of double differenced Doppler frequency (for satellites i and j):

<u>With respect to latitude:</u>

$$\frac{\partial \Delta\nabla\dot{\Phi}^{ij}}{\partial \phi_r} = \frac{\partial \Delta\nabla\dot{\Phi}^{ij}}{\partial x_r}\frac{\partial x_r}{\partial \phi_r} + \frac{\partial \Delta\nabla\dot{\Phi}^{ij}}{\partial y_r}\frac{\partial y_r}{\partial \phi_r} + \frac{\partial \Delta\nabla\dot{\Phi}^{ij}}{\partial z_r}\frac{\partial z_r}{\partial \phi_r}$$

With respect to longitude:

$$\frac{\partial \Delta\nabla\dot{\Phi}^{ij}}{\partial \lambda_r} = \frac{\partial \Delta\nabla\dot{\Phi}^{ij}}{\partial x_r}\frac{\partial x_r}{\partial \lambda_r} + \frac{\partial \Delta\nabla\dot{\Phi}^{ij}}{\partial y_r}\frac{\partial y_r}{\partial \lambda_r} + \frac{\partial \Delta\nabla\dot{\Phi}^{ij}}{\partial z_r}\frac{\partial z_r}{\partial \lambda_r}$$

With respect to height:

$$\frac{\partial \Delta\nabla\dot{\Phi}^{ij}}{\partial h_r} = \frac{\partial \Delta\nabla\dot{\Phi}^{ij}}{\partial x_r}\frac{\partial x_r}{\partial h_r} + \frac{\partial \Delta\nabla\dot{\Phi}^{ij}}{\partial y_r}\frac{\partial y_r}{\partial h_r} + \frac{\partial \Delta\nabla\dot{\Phi}^{ij}}{\partial z_r}\frac{\partial z_r}{\partial h_r}$$

With respect to north velocity:

$$\frac{\partial \Delta\nabla\dot{\Phi}^{ij}}{\partial v_n} = \frac{\partial \Delta\nabla\Phi^{ij}}{\partial \phi_r}$$

With respect to east velocity:

$$\frac{\partial \Delta\nabla\dot{\Phi}^{ij}}{\partial v_e} = \frac{\partial \Delta\nabla\Phi^{ij}}{\partial \lambda_r}$$

With respect to height velocity:

$$\frac{\partial \Delta\nabla\dot{\Phi}^{ij}}{\partial v_h} = \frac{\partial \Delta\nabla\Phi^{ij}}{\partial h_r}$$

where

$$\frac{\partial \Delta\nabla\dot{\Phi}^{ij}}{\partial x_r} = \left\{\frac{\partial^2 \Delta\Phi^i}{\partial x_r^2}(v_x^i - v_{x_r}) + \frac{\partial^2 \Delta\Phi^i}{\partial x_r \partial y_r}(v_y^i - v_{y_r}) + \frac{\partial^2 \Delta\Phi^i}{\partial x_r \partial z_r}(v_z^i - v_{z_r})\right\} - \left\{\frac{\partial^2 \Delta\Phi^j}{\partial x_r^2}(v_x^j - v_{x_r}) + \frac{\partial^2 \Delta\Phi^j}{\partial x_r \partial y_r}(v_y^j - v_{y_r}) + \frac{\partial^2 \Delta\Phi^j}{\partial x_r \partial z_r}(v_z^j - v_{z_r})\right\}$$

$$\frac{\partial \Delta\nabla\dot{\Phi}^{ij}}{\partial y_r} = \left\{\frac{\partial^2\Delta\Phi^i}{\partial x_r \partial y_r}\,(v_x^i - v_{x_r}) + \frac{\partial^2\Delta\Phi^i}{\partial y_r^2}\,(v_y^i - v_{y_r}) + \frac{\partial^2\Delta\Phi^i}{\partial y_r \partial z_r}\,(v_z^i - v_{z_r})\right\} - \left\{\frac{\partial^2\Delta\Phi^j}{\partial x_r \partial y_r}\,(v_x^j - v_{x_r}) + \frac{\partial^2\Delta\Phi^j}{\partial y_r^2}\,(v_y^j - v_{y_r}) + \frac{\partial^2\Delta\Phi^j}{\partial y_r \partial z_r}\,(v_z^j - v_{z_r})\right\}$$

$$\frac{\partial \Delta\nabla\dot{\Phi}^{ij}}{\partial z_r} = \left\{\frac{\partial^2\Delta\Phi^i}{\partial x_r \partial z_r}\,(v_x^i - v_{x_r}) + \frac{\partial^2\Delta\Phi^i}{\partial y_r \partial z_r}\,(v_y^i - v_{y_r}) + \frac{\partial^2\Delta\Phi^i}{\partial z_r^2}\,(v_z^i - v_{z_r})\right\} - \left\{\frac{\partial^2\Delta\Phi^j}{\partial x_r \partial z_r}\,(v_x^j - v_{x_r}) + \frac{\partial^2\Delta\Phi^j}{\partial y_r \partial z_r}\,(v_y^j - v_{y_r}) + \frac{\partial^2\Delta\Phi^j}{\partial z_r^2}\,(v_z^j - v_{z_r})\right\}$$

$$\frac{\partial^2\Delta\Phi^i}{\partial x_r^2} = \frac{1}{\rho^i}\left\{\left(\frac{\partial\Delta\Phi^i}{\partial x_r}\right)^2 - 1\right\}$$ (similarly for y, z and satellite j)

$$\frac{\partial^2\Delta\Phi^i}{\partial x \partial y} = \frac{1}{\rho^i}\left(\frac{\partial\Delta\Phi^i}{\partial x_r}\right)\left(\frac{\partial\Delta\Phi^i}{\partial y_r}\right)$$ (similarly for y, z and satellite j)

$$\frac{\partial^2\Delta\Phi^i}{\partial x \partial z} = \frac{1}{\rho^i}\left(\frac{\partial\Delta\Phi^i}{\partial x_r}\right)\left(\frac{\partial\Delta\Phi^i}{\partial z_r}\right)$$ (similarly for y, z and satellite j)

and v_x^i ... computed x-component velocity of satellite i

(similarly for y, z and satellite j)

v_{x_r} ... x-component velocity of remote receiver

(similarly for y and z).